DEVELOPMENT OF A VERSATILE MAGNETIC PERTURBATION SYSTEM ON THE STOR-M TOKAMAK

A Thesis Submitted to the

College of Graduate and Postdoctoral Studies

in Partial Fulfillment of the Requirements

for the degree of Master of Science

in the Department of Physics and Engineering Physics

University of Saskatchewan

Saskatoon

By

Michael Patterson

PERMISSION TO USE

In presenting this thesis in partial fulfilment of the requirements for a Postgraduate degree from the University of Saskatchewan, I agree that the Libraries of this University may make it freely available for inspection. I further agree that permission for copying of this thesis in any manner, in whole or in part, for scholarly purposes may be granted by the professor or professors who supervised my thesis work or, in their absence, by the Head of the Department or the Dean of the College in which my thesis work was done. It is understood that any copying or publication or use of this thesis or parts thereof for financial gain shall not be allowed without my written permission. It is also understood that due recognition shall be given to me and to the University of Saskatchewan in any scholarly use which may be made of any material in my thesis.

Requests for permission to copy or to make other use of material in this thesis in whole or part should be addressed to:

Head of the Department of Physics and Engineering Physics
University of Saskatchewan
Saskatoon, Saskatchewan S7N 5E2, Canada

or

Dean of the College of Graduate and Postdoctoral Studies
University of Saskatchewan
116 Thorvaldson Building, 110 Science Place
Saskatoon, Saskatchewan S7N 5C9, Canada

ABSTRACT

A system for creating various types of magnetic perturbations relevant to research on mitigation and control of magnetic islands has been developed for the STOR-M tokamak. It utilizes an H-bridge topology and digital controls to switch the discharge from a 51.8 mF capacitor bank and drive current in either a helical coil or a set of discrete coils. This system is capable of safely driving direct or slowly alternating coil currents (< 3 kHz) up to a maximum of 2200 A. At the maximum alternating current frequency of 25 kHz, the highest possible coil current is 1500 A. Preliminary tests have demonstrated modulation of magnetic island rotational frequency during direct current pulses.

ACKNOWLEDGEMENTS

I am deeply appreciative of Professor Akira Hirose, the recently passed director of the Plasma Physics Laboratory. This thesis would not have been possible without his foundational work at the University of Saskatchewan. Thank you also to Jiping Zhang and the crew of the Physics Machine Shop, all of whom provided vital technical assistance. And for all the informal lessons and the laughs, thanks are also due to our post-doctoral fellow, Dr. Sayf Elgriw, and my fellow graduate students, Akbar Rohollahi, Reza Behbahani, Masaru Nakajima, Joseph Adegun, and Seanne Chung.

Above all however, I am indebted to my supervisor, Professor Chijin Xiao, for the opportunity to work on such an interesting problem, and I am deeply grateful to him for his excellent guidance and patient support. I could not have succeeded without the aid of his wisdom and many insights, from which I have learned so much.

This research was supported by the grants from the Natural Sciences and Engineering Research Council of Canada (NSERC), and the Sylvia Fedoruk Canadian Centre for Nuclear Innovation and through financial aid from the University of Saskatchewan.

DEDICATION

To my mother

CONTENTS

LIST OF TABLES

LIST OF FIGURES

LIST OF ABBREVIATIONS

ELM	Edge Localized Mode
EMI	ElectroMagnetic Interference
FPGA	Field Programmable Gate Array
ICF	Inertial Confinement Fusion
IGBT	Insulated Gate Bipolar Transistor
ITER	International Thermonuclear Experimental Reactor
J-TEXT	Joint-TEXT
MCF	Magnetic Confinement Fusion
MHD	Magnetohydrodynamics
RMP	Resonant Magnetic Perturbation
STFT	Short Time Fourier Transform
STOR-M	Saskatchewan TORus-Modified
TEXTOR	Tokamak EXperiment for Technology Oriented Research

CHAPTER 1

INTRODUCTION

The fossil fuels that enabled the industrial revolution and the rapid growth that followed are in limited supply. As the world's energy demands continue to rise this only shortens the time left until their depletion and the collapse of the societal systems that depend on them. Moreover, it is now clear that the use of these fuels has come at a heavy cost, namely the addition of enormous quantities of greenhouse gases into the atmosphere, resulting in significant changes to the Earth's climate. For catastrophic damage to be avoided it will be necessary to avoid burning the majority of fossil fuel reserves [1, 2]. Clearly, new sources of energy need to be developed.

Solar, wind, and hydroelectric power are likely to play a key role in replacing fossil fuels but have fundamental drawbacks that prevent them from being a total solution. Solar and wind power production require high capital costs, are useful only where these resources are abundant, have a large geographic footprint, and are subject to climate and weather. Additionally, no effective method currently exists to store the energy generated via these methods, making it impossible to sufficiently smooth out the power supply to match the demand. Once the plant has been built, the cost of hydroelectric energy is quite low and the supply is steady. However, there are a limited number of locations suitable for such facilities and they are likewise subject to changes in climate, such as droughts.

Nuclear power presents an attractive alternative. Examining the energy densities of various fuels in Table 1.1, it can be seen that the mass of fuel needed to produce a given amount of energy is 6 to 7 orders of magnitude lower for nuclear reactions than chemical ones. All currently operating commercial nuclear reactors work by extracting energy from nuclear fission, where heavy nuclei decay naturally, or are stimulated to do so by absorption of a neutron. This process requires no external energy source. The required effort is in controlling the rate of fission, so as to avoid an explosive runaway or meltdown. This, and the potential for weapons proliferation have led to public

Table 1.1: Energy density of various fuels

Fuel	Reaction Type	Energy Density (MJ/kg)
Deuterium-Helium^3	Fusion	384,000,000
Deuterium-Tritium	Fusion	340,000,000
Deuterium	Fusion	87,900,000
Uranium	Fission	80,620,000
Thorium	Fission	79,420,000
Hydrogen at 10,000 psi	Chemical	142
Methane	Chemical	55.5
Gasoline	Chemical	46.4
Diesel	Chemical	48
Ethanol	Chemical	26.4
Coal	Chemical	24 - 35

concern regarding nuclear power. New developments could improve the safety and efficiency of fission reactors but they still face one of the primary problems of other fuels: a relatively limited supply.

The inverse process of nuclear fission is known as nuclear fusion, the combination of two or more nuclei into a single, heavier nucleus. While for heavy nuclei this process requires energy input, for light nuclei, energy is released by the reaction. As an energy source, fusion possesses significant advantages over fission. The most likely reaction candidate for a commercial reactor is deuterium-tritium fusion, with the tritium being bred from lithium.

$$ {}^{6}_{3}Li + n \rightarrow {}^{4}_{2}He + {}^{3}_{1}H + 4.8\ \text{MeV} \tag{1.1} $$

$$ {}^{2}_{1}H + {}^{3}_{1}H \rightarrow {}^{4}_{2}He + n + 17.6\ \text{MeV} \tag{1.2} $$

The primary fuels, deuterium and lithium, are incredibly abundant, and would last for millions

of years. Neither are radioactive, nor is the reaction product, helium. While tritium is radioactive, it has a half life of 12.3 years and only a few grams of fuel will be present in a reactor at a given time. The walls of the machine itself will become activated over time due to neutron bombardment, and this represents the main radiation concern. Careful choice of materials would limit this problem. Additionally, fusion reactors produce a minimal carbon footprint; the reaction itself produces no greenhouse gases. Any climate impact would be limited to construction and maintenance of a facility.

Fusion reactors are also inherently safe, and are immune to meltdowns. For fusion to occur, ideal conditions have to be maintained and deviation from those conditions results in the immediate termination of the reaction. This strength is also however, the main difficulty in developing a viable reactor. Over a half-century of effort has been put into developing a method to maintain the temperature and density of the fuel efficiently enough to extract more energy than is put in.

The two main approaches to achieving this goal are known as Inertial Confinement Fusion (ICF) and Magnetic Confinement Fusion (MCF). ICF works by superheating pellets of fuel with lasers resulting in the blowing off of material compressing the fuel core into fusion conditions. When heating fuel to fusion relevant conditions, where it is in the plasma state, it will rapidly lose energy to any chamber containing it, and there are no materials capable of withstanding these temperatures. In MCF hot, dense fuel is prevented from losing its energy by confining it with magnetic fields long enough for significant amounts of energy to be generated due to fusion.

Developed in the Soviet Union in the 1950s, the tokamak device is one of the primary candidates for a commercial MCF power plant, but has yet to achieve breakeven, where it produces more energy than is supplied.

To achieve a net energy gain, the triple product of density, n, temperature, T, and confinement time, τ - a measure of the rate at which energy is lost - needs to exceed a certain value. For the dueterium-tritium reaction that value is [3],

$$nT\tau > 3 \times 10^{21} \text{ keV s m}^{-3} \tag{1.3}$$

This is known as the Lawson criterion [4]. While enormous progress has been made, increasing the triple product by a factor of approximately 10^4 to the current record of $1.53x10^{21}$ keV s m^{-3} [5], another order of magnitude improvement needs to be realized.

The International Thermonuclear Experimental Reactor (ITER), currently under construction, promises to demonstrate energy breakeven and will be used to carry out research on the remaining issues in MCF. The world's current network of tokamaks is supporting this mission by investigating new methods to improve efficiency and deal with the problems of developing a commercial power plant, as well as contributing to our understanding of the basic physics of plasma behaviour in tokamak devices. Among the remaining challenges are the negative impacts of magnetohydrodynamic instabilities, the development of a system to mitigate these being the final goal of this thesis.

Following this introduction, Chapter 1 will illustrate the tokamak concept. Chapter 2 will introduce the basics of magnetohydrodynamic theory and magnetic instabilities. In Chapter 3, the method and history of manipulating magnetic instabilities by means of applied external magnetic perturbations will be detailed. Chapter 4 explains the design of the magnetic coils utilized by the new perturbation system. Chapter 5 explains the mathematical modelling and practical implementation of the power supply's circuit topology. An introduction to the tools and methods that were used to diagnose the perturbation system's effects on the plasma is given in Chapter 6. This is followed by the results of preliminary system tests in Chapter 7. And finally, Chapter 8 summarizes the work performed and provides suggestions for future efforts.

CHAPTER 2

THE TOKAMAK CONCEPT

During a collision between atomic nuclei the Coulomb force between them will increase until they are repulsed. However, if they are of sufficiently high energy they will approach within range of the strong nuclear force, resulting in their fusion. Figure 2.1 shows the potential energy of the simplest nuclear interaction: proton-proton. Even when relative particle energy is not higher than the potential barrier, quantum tunnelling can allow fusion to occur.

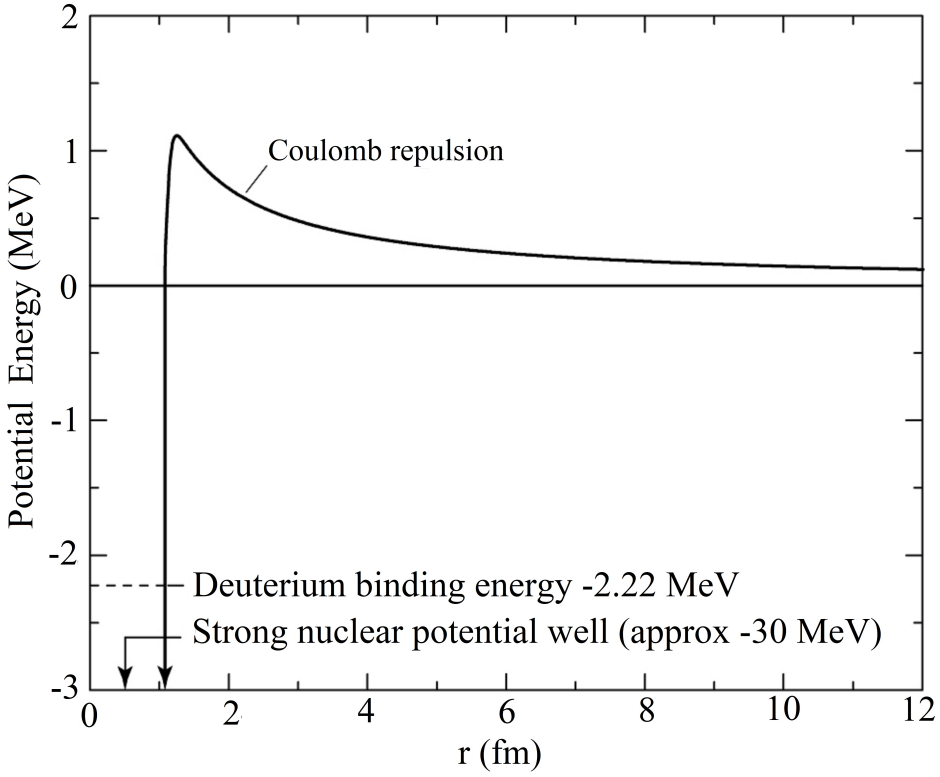

Figure 2.1: Coulomb barrier for the proton-proton interaction (from [6])

On the macroscopic scale, mean particle energy equates to temperature, and so all that is re-

quired to achieve fusion is to heat the fuel to adequate temperatures. However, to do this at an appreciable rate for a given quantity of fuel, a high density must be maintained by preventing its expansion and containing the fuel within a limited volume, as the collision frequency is proportional to the fuel's density. As mentioned previously, confining the hot fuel within a material vessel is not possible.

2.1 Method of Confinement

Ions that are energetic enough to overcome Coulomb repulsion and fuse together exist in the plasma state. While a bulk plasma is electrically neutral, the individual particles are charged and respond to electromagnetic fields. When collisions are ignored, a single particle of mass m, and charge q, travelling in electric and magnetic fields $\mathbf{E}$ and $\mathbf{B}$ has the equation of motion,

$$m\frac{d\mathbf{v}}{dt} = q(\mathbf{E} + \mathbf{v} \times \mathbf{B}) \tag{2.1}$$

where $\mathbf{v}$ represents the particle's velocity.

If these field lines point in the same direction, so that $\mathbf{E} = E\hat{\mathbf{z}}$ and $\mathbf{B} = B\hat{\mathbf{z}}$, and for simplicity are uniform,

$$\begin{aligned} m\frac{dv_x}{dt} &= qBv_y \quad : \quad \hat{\mathbf{x}}\text{-direction} \\ m\frac{dv_y}{dt} &= -qBv_x \quad : \quad \hat{\mathbf{y}}\text{-direction} \\ m\frac{dv_z}{dt} &= qE \quad : \quad \hat{\mathbf{z}}\text{-direction} \end{aligned} \tag{2.2}$$

Looking at the $\hat{\mathbf{z}}$-direction, the electric field, or indeed any force that acts parallel to the magnetic field, causes a constant acceleration in the magnetic field direction if unimpeded. The $\hat{\mathbf{x}}$ and $\hat{\mathbf{y}}$ components describe simple harmonic motion in their respective directions, or circular motion in the $x-y$ plane. Taking initial particle motion perpendicular to the magnetic field, $v_\perp$, to be in the $\hat{\mathbf{x}}$-direction,

$$\begin{aligned} v_x &= v_\perp \cos(\omega_c t) \\ v_y &= \mp v_\perp \sin(\omega_c t) \\ v_z &= \frac{q}{m}Et + v_{z_0} \end{aligned} \tag{2.3}$$

where $\omega_c = \frac{|q|B}{m}$, known as the cyclotron frequency, and the sign of v_y is determined by the particle's charge. Charged particles are constrained to rotate around magnetic field lines, but free

to travel indefinitely or be accelerated along the direction of the magnetic field. While various complications arise when attempting to take advantage of this behaviour in real-world applications, it is the basis for all magnetic confinement fusion devices.

The tokamak device to be discussed in this thesis is a donut-shaped apparatus. It is necessary to introduce the so-called toroidal coordinate system. In this system, shown in Figure 2.2, locations are defined by the coordinate values ϕ, θ, and r, and the typically constant major radius R. The toroidal coordinate ϕ defines the angular rotation in the plane of the major radius. The poloidal coordinate θ gives the angular position in the plane of the minor radius r. And, the minor radius describes the distance from the major radius. a is the maximum possible value of r, which in this thesis will be the radius of a plasma column .

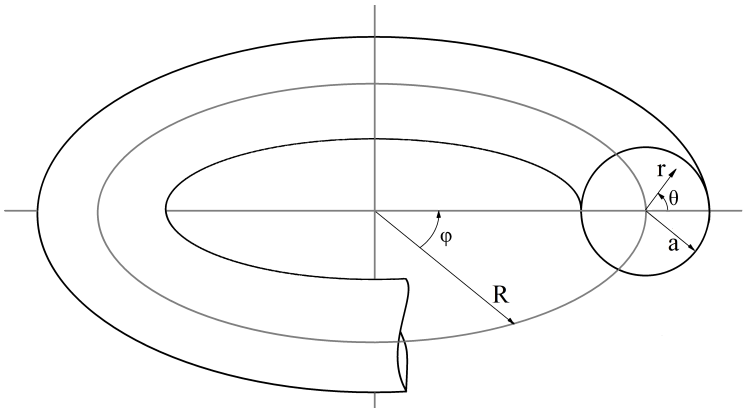

Figure 2.2: Toroidal coordinate system

If a solenoid and its uniform axial magnetic field were bent into a torus so that the ends connected, it may at first seem charged particles would continuously move in the toroidal ($\hat{\phi}$) direction without a net radial translation. In reality, the transition of the solenoid to a torus means the toroidal field windings will be farther apart on the outboard side than on the inboard side of the torus, resulting in a toroidal magnetic field inhomogeneity in the major radial direction. This means that as a particle gyrates, it travels through regions of varying field strength. The effect of this is a drift perpendicular to both the magnetic field direction and its gradient at a velocity $v_{\nabla B}$. Additionally, the centrifugal force felt by particles as they travel toroidally results in a second drift velocity v_R, known as curvature drift. The combined cross-field drift velocity can be expressed by the following equation, where $v_{\parallel}$ and $v_{\perp}$ represent particle velocities parallel and perpendicular to the magnetic

field respectively:

$$\mathbf{v}_R + \mathbf{v}_{\nabla B} = \frac{m(v_\parallel^2 + \frac{1}{2}v_\perp^2)}{q} \frac{\mathbf{R} \times \mathbf{B}}{R^2 B^2} \tag{2.4}$$

These two drifts sum, and have opposite directions for positive and negative particles, which causes a charge separation to develop. This establishes an electric field and leads to $E \times B$ drift, transporting particles radially outward.

$$\mathbf{v}_E = \frac{\mathbf{E} \times \mathbf{B}}{B^2} \tag{2.5}$$

In a tokamak, a toroidal electric field is created through transformer action and the driven current establishes a poloidal magnetic field. The total magnetic field lines then form a helical path as shown in Figure 2.3. When particles spiral along the helical magnetic field lines the radial displacement due to the gradient and curvature drifts is averaged out because of the poloidal rotation.

The plasma safety factor,

$$q(r) = \frac{rB_\phi(r)}{RB_\theta(r)} \tag{2.6}$$

describes the helicity of the magnetic field lines in a tokamak, which in equilibrium conditions lie on nested flux surfaces. B_ϕ refers to the toroidal magnetic field and B_θ the poloidal magnetic field. The name *safety factor* is used because it was found that maintaining $q(a) > 1$ was required to maintain a stable tokamak discharge.

In the minor radius direction, force balance of average thermal pressure and average magnetic pressure requires that

$$p = \frac{< B^2 >}{2\mu_0} \tag{2.7}$$

This balance is maintained through self-adjustment of the average toroidal magnetic field due to the plasma's diamagnetism from Larmor motion and paramagnetism of the plasma current. Changes in the toroidal magnetic field due to poloidal currents result in compressive force in the major radial direction.

Opposing this, like the repulsive force between two current-carrying wires with anti-parallel currents, there exists an expanding force as for any current loop. The current carriers in each segment of a loop are pushed outward due to the magnetic field generated by anti-parallel current components on the opposing side of the loop.

In addition to the toroidal field generated by external coils and the poloidal field from the plasma current, tokamaks require a vertical magnetic field:

$$B_{vertical} = \frac{\mu_0 I_p}{4\pi R}\left[\ln\left(\frac{8R}{a}\right) - \frac{3}{2} + \frac{2\mu_0 p}{B_\theta^2(a)} + \frac{2\pi}{\mu_0} l_i\right] \tag{2.8}$$

where a represents the tokamak's minor radius, I_p the plasma current, and l_i the internal inductance per unit length. The Lorentz force caused by the interaction of the vertical magnetic field and the plasma current balances the pressure in the major radial direction, as well as the forces in this direction due to the hoop current and changes in internal magnetic field.

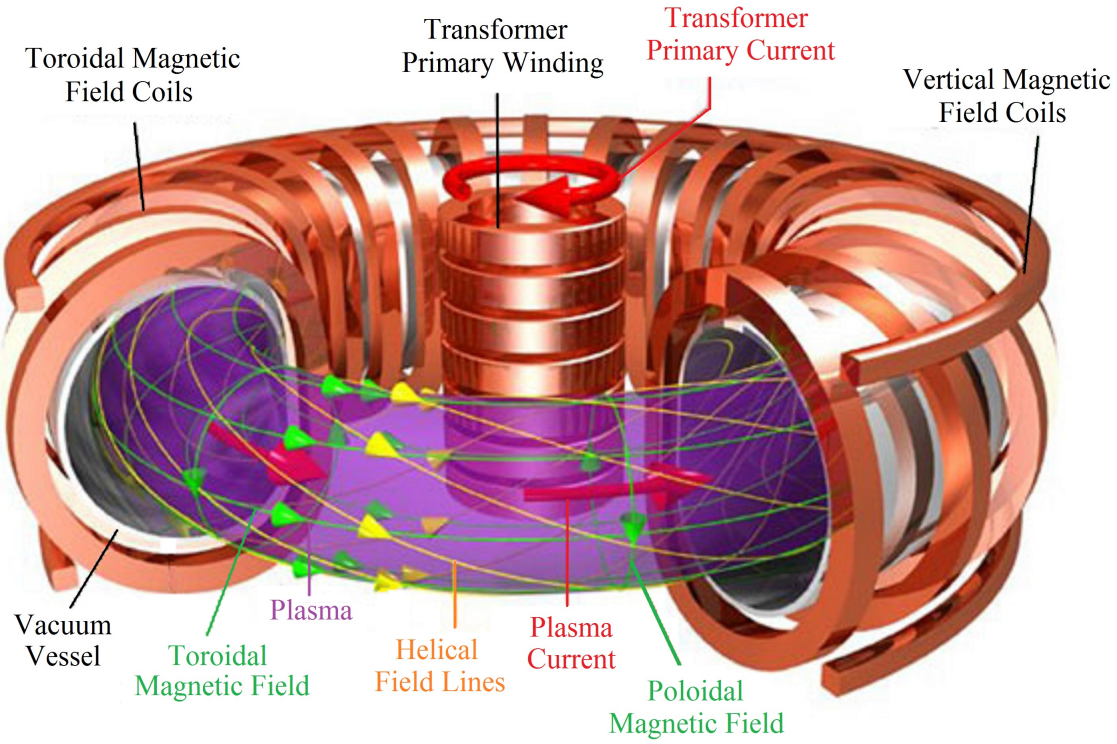

Figure 2.3: Tokamak coils and magnetic field lines (from [7])

2.2 STOR-M

The Saskatchewan Torus-Modified, or STOR-M, tokamak is a small tokamak, an upgrade from its predecessor, STOR-1M, built to investigate plasma heating and anomalous transport and explore potential new operating modes and advanced diagnostics. Completed at the University of Saskatchewan in 1987, it underwent a major upgrade to its toroidal magnetic field system in 1994.

Significant experiments performed on the device have included turbulent heating via current pulsing [8], plasma biasing [9], AC operation [10], compact torus injection [11, 12], examination of magnetohydrodynamic instabilities [13], plasma edge characterization [14, 15], and diamagnetic measurements [16]. Table 2.1 summarizes STOR-M's main parameters.

Table 2.1: STOR-M main parameters

Parameter	Value
Major Radius, R	46 cm
Minor Radius, a	12.5 cm
Toroidal Magnetic Field, B_ϕ	$0.5 \sim 1$ T
Plasma Current, I_p	$20 \sim 30$ kA
Electron Density, n_e	$1 \sim 3 \times 10^{13}$ cm^{-3}
Electron Temperature	$2 \sim 300$ eV
Confinement Time, τ_E	$2 \sim 5$ ms
Discharge Duration	$35 \sim 45$ ms

The vacuum chamber of STOR-M, made of 4 mm thick 304 alloy stainless steel, has a circular cross-section in both toroidal and poloidal cuts. A limiter of inner diameter 13 cm, with horizontal rails at 12 cm radial distance from the major axis confines the plasma within the center of the chamber, but allows 1 cm of horizontal plasma displacement without scrape-off. The rigid halves of the chamber are connected with a ceramic break and bellows at each joint. The bellows reduce mechanical stress and the ceramic breaks prevent the chamber from acting as another transformer winding.

Figures 2.4 and 2.5 are schematics of STOR-M's chamber, coils, and ports. There are 11 vertical, 10 horizontal, and 2 tangential ports that allow access to the inner chamber for diagnostics, pumps, the CT injector, and the gas feed system.

Rough pumping with a rotary pump evacuates the chamber to the working range of a turbomolecular pump, which brings the chamber to a base pressure of 8.0×10^{-8} torr. Ultra-pure

(99.999%) hydrogen is used as a filling gas and discharges are usually performed at 1.0×10^{-4} torr. Gas puffs can be set to be released at specific times in the discharge to adjust plasma density as needed.

There are three capacitor banks. The biasing bank (20 mF, 450 V) negatively biases STOR-M's iron core of 0.1 Wb flux capacity before the main discharge, which allows for a larger flux swing. A fast bank (200 mF, 450 V) drives ionization and the plasma current ramp-up. A current plateau is maintained by the slow bank (10 F, 100 V).

Pick-up coils detect the horizontal plasma position and their signals are sent to an automated control system which adjusts the current to the vertical field coils, keeping the plasma column centered in the vessel.

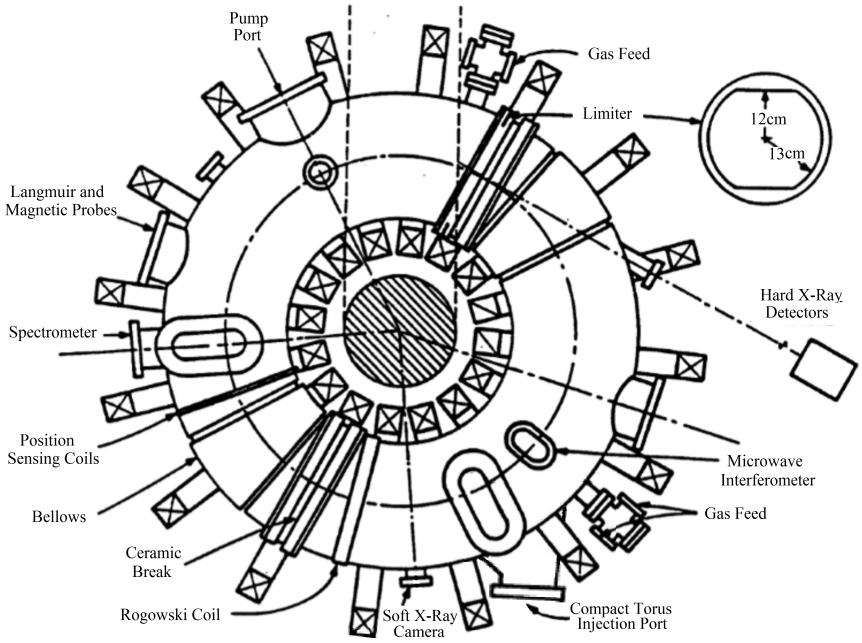

Figure 2.4: STOR-M schematic, overhead view (from [17]). Location of fittings and diagnostics noted

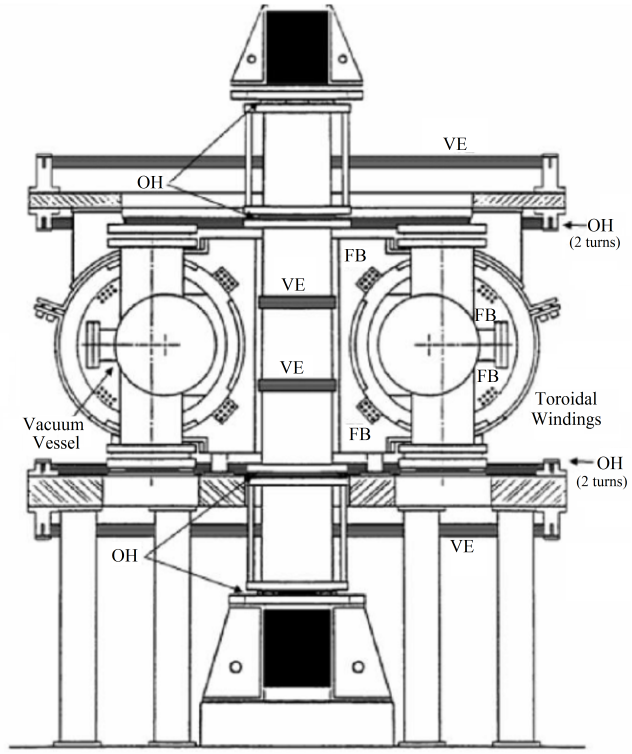

Figure 2.5: STOR-M schematic, vertical cross-section (from [18])
Marked coils are VE: vertical equilibrium, OH: ohmic heating, FB:feedback

Figure 2.6 displays the time-evolution of the main parameters recorded in order to characterize the plasma in a STOR-M discharge. The toroidal plasma current, I_p, is obtained via the integrated signal from a Rogowski coil which encircles the vacuum chamber in the poloidal direction and has a return line to avoid picking up poloidal current.

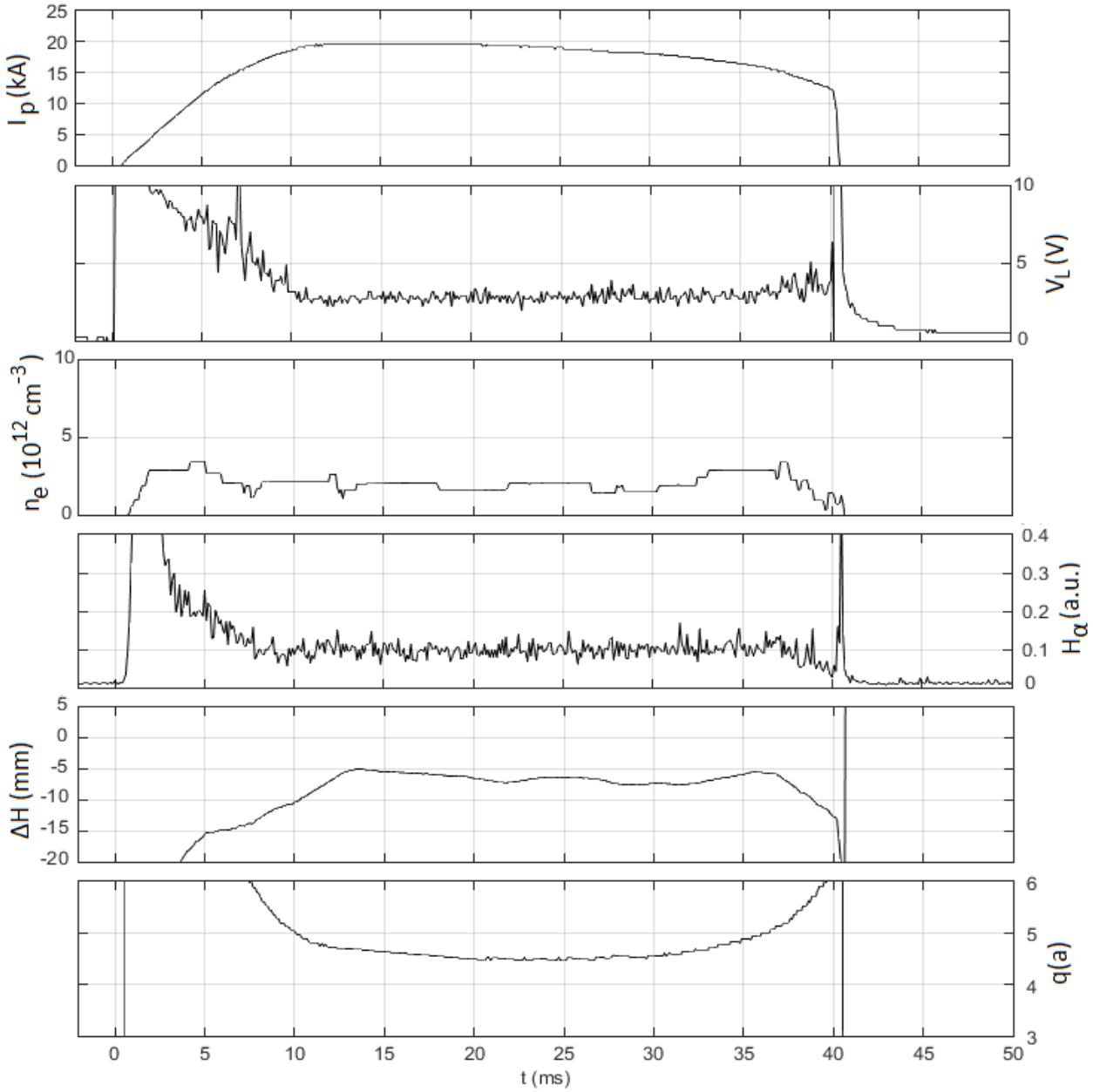

Figure 2.6: Typical STOR-M discharge waveforms (from shot 316301). From top to bottom: plasma current, loop voltage, electron density, H_α emission, horizontal offset, and safety factor at the plasma edge

A simple coil placed on top of the vacuum chamber acts as half of a 1:1 transformer and is used to measure the loop voltage, V_L, around the torus. Together with the plasma current this enables a straightforward estimation of the average plasma resistivity. As the plasma current is relatively constant during the "flat-top" region, and the plasma resistivity is largely impacted by the plasma's composition, loop voltage is used as an indicator of the plasma's cleanliness or purity. Impurities in the plasma increase radiation loss, reduce the electron temperature in the plasma and thus increase the plasma resistivity.

The line-averaged electron density, n_e, is measured using a 4-mm interferometer and H_α emission with a monochromator. H_α refers to hydrogen's Balmer transition, emitting photons of wavelength 656.28 nm. This radiation is due to energy-level drop-down of neutrals within the plasma.

The horizontal position is calculated using information from position sensing coils: simple magnetic pick-up loops connected to a comparator circuit. And, magnetic field line helicity (see Section 3.3) at the plasma edge, $q(a)$, is determined by means of the an assumed plasma current profile and toroidal magnet currents.

CHAPTER 3

MAGNETOHYDRODYNAMICS

3.1 MHD Equations

The simple, single-fluid model that describes the large-scale, slow interaction between a plasma and electromagnetic field is known as magnetohydrodynamics (MHD). The effects of viscosity, heating, ionisation, or radiation are not considered but MHD provides an overall picture of many plasma processes when the lengths and time periods of the events being examined are larger than certain characteristic scales. These are the ion mean-free-path time and length and the ion gyro-period and gyro-radius. Particle velocities are taken to be non-relativistic.

This conducting fluid model uses the equations of fluid dynamics, along with Maxwell's equations, to connect the macroscopic variables of plasma mass density ρ, current density $\mathbf{j}$, velocity $\mathbf{v}$, and kinetic pressure p to the electric and magnetic fields, $\mathbf{E}$ and $\mathbf{B}$.

For a plasma with singly charged ions,

$$\rho = n_i m_i + n_e m_e \approx n(m_i + m_e) \tag{3.1}$$

$$\mathbf{v} = \frac{n_i m_i \mathbf{v}_i + n_e m_e \mathbf{v}_e}{\rho} \approx \frac{m_i \mathbf{v}_i + m_e \mathbf{v}_e}{m_i + m_e} \tag{3.2}$$

$$\mathbf{j} = e(n_i \mathbf{v}_i - n_e \mathbf{v}_e) \approx ne(\mathbf{v}_i - \mathbf{v}_e) \tag{3.3}$$

$$p = p_i + p_e \tag{3.4}$$

where the simplified approximations on the right have taken advantage of the plasma's quasineutrality: $n_i \approx n_e$.

The Continuity Equation takes the same form as in standard fluid dynamics, and is a statement of mass conservation. The change of mass entering and leaving a volume is entirely due to the

difference between the rates of mass entering and exiting the volume.

$$\frac{\partial \rho}{\partial t} + \nabla \cdot (\rho \mathbf{v}) = 0 \quad : \quad \text{Continuity Equation} \tag{3.5}$$

In the MHD model processes within the plasma are generally assumed to be adiabatic:

$$pV^{\gamma} = constant \tag{3.6}$$

V being the plasma volume, and γ the ratio of specific heats. Mass is conserved within a moving fluid cell, so that $V \sim \rho^{-1}$. Then,

$$\frac{d}{dt}\Big(\frac{p}{\rho^{\gamma}}\Big) = \Big(\frac{\partial}{\partial t} + \mathbf{v} \cdot \nabla\Big)\frac{p}{\rho^{\gamma}} = 0 \quad : \quad \text{Equation of State} \tag{3.7}$$

the derivative moving with the fluid $\big(\frac{d}{dt}\big)$ being separated into the local derivative, the rate of change of a quantity at a specific point $\big(\frac{\partial}{\partial t}\big)$, and the convective term $\big(\mathbf{v} \cdot \nabla\big)$.

Viscosity will be ignored, which is reasonable if the characteristic frequency is larger than the ion collision frequency. It is also quickly seen that collisional momentum transfer from one species to another, $\boldsymbol{\mathcal{P}}_{12} = \eta e^2 n^2 (\mathbf{v}_2 - \mathbf{v}_1)$, can be ignored as $\boldsymbol{\mathcal{P}}_{ie} = -\boldsymbol{\mathcal{P}}_{ei}$. Here, η represents the plasma resistivity. The dominant terms in the ion and electron equations of motion are

$$m_i n \frac{\partial \mathbf{v}_i}{\partial t} = en\big(\mathbf{E} + \mathbf{v}_i \times \mathbf{B}\big) - \nabla p_i + \boldsymbol{\mathcal{P}}_{ie} \tag{3.8}$$

$$m_e n \frac{\partial \mathbf{v}_e}{\partial t} = en\big(\mathbf{E} + \mathbf{v}_e \times \mathbf{B}\big) - \nabla p_e + \boldsymbol{\mathcal{P}}_{ei} \tag{3.9}$$

which can be summed to obtain the single fluid equation,

$$n\frac{\partial}{\partial t}(m_i \mathbf{v}_i + m_e \mathbf{v}_e) = en(\mathbf{v}_i - \mathbf{v}_e) \times \mathbf{B} - \nabla p \tag{3.10}$$

$$\rho\Big(\frac{\partial}{\partial t} + \mathbf{v} \cdot \nabla\Big)\mathbf{v} = -\nabla p + \mathbf{j} \times \mathbf{B} \quad : \quad \text{Equation of Motion} \tag{3.11}$$

the last equation having utilized the earlier definitions for ρ, $\mathbf{j}$, and p.

The linear combination of [m_e(Eq.3.8) + m_i(Eq.3.9)]/ρe can be written as

$$\mathbf{E}+\mathbf{v}\times\mathbf{B}=\eta\mathbf{j}+\frac{1}{\rho e}\left[\frac{m_i m_e n}{e}\frac{\partial}{\partial t}\left(\frac{\mathbf{j}}{n}\right)+(m_i+m_e)\mathbf{j}\times\mathbf{B}+m_e\nabla p_i+m_i\nabla p_e\right] \tag{3.12}$$

For times longer than gyro-period the time derivative is neglected. The ratio of species' masses, $\frac{m_e}{m_i}\approx 0$ allows further simplification.

$$\mathbf{E}+\mathbf{v}\times\mathbf{B}=\eta\mathbf{j}+\frac{1}{ne}\left(\mathbf{j}\times\mathbf{B}-\nabla p_e\right) \quad : \quad \text{Ohm's Law} \tag{3.13}$$

The Hall current ($\mathbf{j}\times\mathbf{B}$) term and electron pressure gradient are quite small and can be disregarded as well [19].

MHD theory is described by the set of Equations 3.5, 3.7. 3.11, 3.13 together with Maxwell's Equations. The quasineutrality gives zero electric field divergence.

$$\nabla\cdot\mathbf{E}\approx 0 \quad : \quad \text{Gauss's Law for Electricity} \tag{3.14}$$

$$\nabla\cdot\mathbf{B}=0 \quad : \quad \text{Gauss's Law for Magnetism} \tag{3.15}$$

$$\nabla\times\mathbf{E}=-\frac{\partial\mathbf{B}}{\partial t} \quad : \quad \text{Faraday's Law} \tag{3.16}$$

$$\nabla\times\mathbf{B}\approx\mu_0\mathbf{j} \quad : \quad \text{Ampere's Law} \tag{3.17}$$

where once again the displacement current in Ampere's Law has been ignored for the low velocities/frequencies for which MHD theory is applicable, and since the current density is large and the electric field weak in a tokamak. For situations in which the plasma resistivity, η, can be considered to be zero, these set of equations are referred to as ideal MHD.

3.2 MHD Equilibrium

At equilibrium, Equation 3.11 describes the force balance between the kinetic and magnetic pressures:

$$\nabla p = \mathbf{j} \times \mathbf{B} \tag{3.18}$$

which says that plasma currents and magnetic fields are both perpendicular to the pressure gradient. That is, current sheets and magnetic flux surfaces lie on isobaric surfaces. By use of the vector identity,

$$\nabla(\mathbf{A} \cdot \mathbf{B}) = \mathbf{A} \times (\nabla \times \mathbf{B}) + \mathbf{B} \times (\nabla \times \mathbf{A}) + (\mathbf{B} \cdot \nabla)\mathbf{A} + (\mathbf{A} \cdot \nabla)\mathbf{B} \tag{3.19}$$

and elimination of the current density by means of Ampere's Law, Equation 3.18 can be rewritten as,

$$\nabla\left(p + \frac{B^2}{2\mu_0}\right) = \frac{1}{\mu_0}(\mathbf{B} \cdot \nabla)\mathbf{B} \tag{3.20}$$

The term on the right represents the magnetic tension which balances the total pressure gradient (left half of Eq. 3.20). For straight magnetic field lines, $(\mathbf{B} \cdot \nabla)\mathbf{B} = 0$. In, for example, a cylindrical plasma column with an axial magnetic field, the sum of plasma kinetic pressure and and magnetic pressure remains constant. The kinetic pressure decreases with radial distance from the cylinder's axis, and so the magnetic pressure (and field) increases accordingly. The change in magnetic field strength is due to diamagnetic current. The ratio of thermal and magnetic pressure is known as the plasma beta:

$$\beta = \frac{p}{B^2/2\mu_0} \tag{3.21}$$

which characterizes the efficiency with which the magnetic field confines the plasma. Despite the curvature ignored in Equation 3.20, conventional tokamaks with a large aspect ratio (R/a) generally do not strongly diverge from the cylindrical approximation assumed in the derivation of the plasma beta. For simplicity, β is often given in terms of the mean pressure and the averaged magnetic field along a specific line. For tokamaks, with B_{ϕ_0} being the magnetic field on the toroidal axis, and

B_{θ_a} the averaged poloidal magnetic field on the plasma surface, we define the toroidal and poloidal betas,

$$\beta_\phi = \frac{< p >}{B_{\phi_0}^2/2\mu_0} \tag{3.22}$$

$$\beta_\theta = \frac{< p >}{B_{\theta_a}^2/2\mu_0} \tag{3.23}$$

The toroidal field of a tokamak is far stronger than its poloidal field and β_ϕ is dominant when considering plasma confinement. The higher the magnetic field required, the more expensive the magnets, so it is preferred to operate at as high a beta as possible. $\beta < 1$, (kinetic pressure lower than magnetic pressure) is of course necessary for confinement but there is in practice a far lower limit on the plasma beta.

3.3 MHD Instabilities

3.3.1 Ideal MHD Instabilities

There are two classes of large-scale instabilities that can develop in a tokamak plasma. "Ideal" instabilities refer to those that arise in the non-resistive MHD model and can cause bending and bulging of the field lines. They develop on the microsecond scale and rapidly disrupt the plasma. It was found experimentally that ideal instabilities can be avoided by limitation of the plasma beta [20]. Numerical calculations give this limit in terms of the Troyon factor, β_N, as well as the plasma current, I_ϕ, tokamak minor radius, a, and toroidal magnetic field B_ϕ.

$$\beta < 10^{-8}\frac{\beta_N I_\phi}{aB_\phi} \tag{3.24}$$

The Troyon factor, or normalized beta, was calculated to be $2.5 \sim 3.5$ leading to a plasma β limit on the order of 0.01 [21]. It was later found that plasma shaping could drastically improve this factor. The spherical tokamak NSTX achieved $\beta_N = 7.2$ and $\beta = 0.39$ [22] while still avoiding disruptions due to ideal MHD instabilities.

3.3.2 Resistive MHD Instabilities

When including finite plasma resistivity in the MHD equations a different set of "resistive" instabilities is found. These lead to the so-called tearing modes, magnetic reconnection, and the formation of magnetic islands, and have proven much harder to control.

The magnetic field lines in a tokamak can spiral endlessly, filling the entire surface they lie on. Or, they can travel a finite number of times poloidally (rotating around the minor axis) and toroidally (rotating around the major axis) before reconnecting to themselves. Such lines occur at rational surfaces, described by the poloidal and toroidal integer mode numbers, m and n respectively. m represents the number of nodes in the poloidal direction, or number of times a closed field line travels around the tokamak in the toroidal direction before closing on itself. And n represents the number of nodes in the toroidal direction, or number of times a closed field line travels around the tokamak in the poloidal direction before closing on itself. For rational surfaces then, the safety factor can be written as

$$q(r) = \frac{m}{n} \tag{3.25}$$

The helicity of the total (toroidal and poloidal) equilibrium field increases with the minor radius, so that there is a shear, s, between different flux surfaces.

$$s(r) = \frac{r}{q}\frac{dq}{dr} \tag{3.26}$$

Small deviations from this idealized situation (typically from the deviation of the current profile in the plasma from the equilibrium profile and also from minute imperfections in the engineering or construction of the device) introduce a radial field component, known as the error field, that combines with the field's shear to break apart the nested flux surfaces into magnetic islands. This occurs at rational surfaces along the magnetic field lines and the islands can therefore also be characterized by m and n. Figure 3.1 illustrates the difference between the nested flux surfaces of equilibrium and a single m/n = 2/1 magnetic island resulting from a tearing mode, viewed on a vertical cress-section at a fixed toroidal angle. It is possible for many islands to be present on different rational surfaces at different radial locations simultaneously, which can be locked together or rotate independently.

If B_{r_0mn} represents the amplitude of a specific m/n island at a radial location r_0, then for a rotational frequency ω, the radial magnetic field of the plasma is given by:

$$B_r(\theta,\phi,t) = \sum_{m,n} B_{r_0mn}\cos(m\theta - n\phi + \omega_{mn}t) \tag{3.27}$$

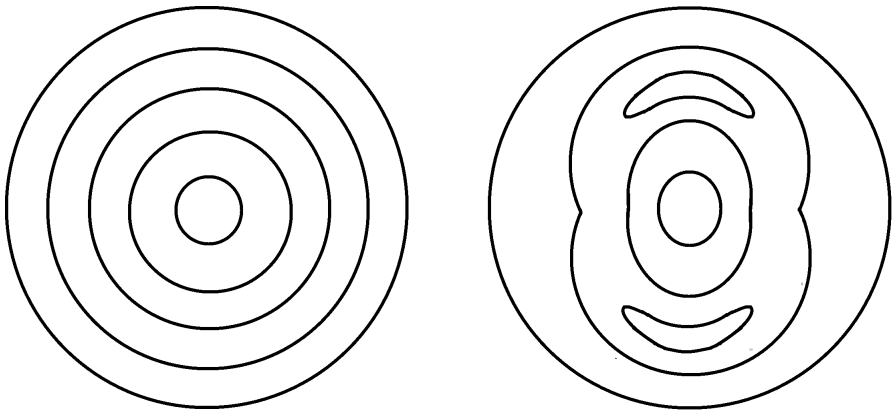

(a) **(b)**

Figure 3.1: Flux surfaces of a poloidal cross-section. (a) Nested Surfaces. (b) Magnetic Island, m/n = 2/1

The coefficient for diffusion across magnetic field lines is proportional to the square of the characteristic transport length which is usually determined by the Larmor radius. When a magnetic island develops however, particles can rapidly be transported radially outward by moving along a magnetic island's field lines and therefore magnetic islands are a serious detriment to the confinement of these particles and the energy they carry.

In general, magnetic islands rotate in the plasma. However, if an island becomes too large it can slow down, and even become stationary, locked to the resonant error field which helped create it [23, 24]. The plasma rotation imparts toroidal momentum to the islands but for large islands/external fields, this may not be strong enough to prevent locking. Then, eddy currents in the chamber wall which previously acted to stabilize the island are no longer present and island width can grow quickly.

Islands that grow large enough can cause disruptions, potentially dangerous events analogous to a lightning strike on the chamber walls, in which a large current quench can cause severe heating to the affected plasma-facing components. In the most extreme case islands can grow to such a

large size that they result in termination of the plasma, potentially catastrophic heating in a limited area and extreme mechanical stress on the whole device due to the inductive forces resulting from the rapid current decay [25].

Commercial reactors may purposely create and manipulate islands in order to exploit this transport to limit the quantity of helium ash in the plasma. In general, however, when the creation of magnetic islands cannot be prevented, it is desirable to suppress growth of their width and limit the radial transport they allow.

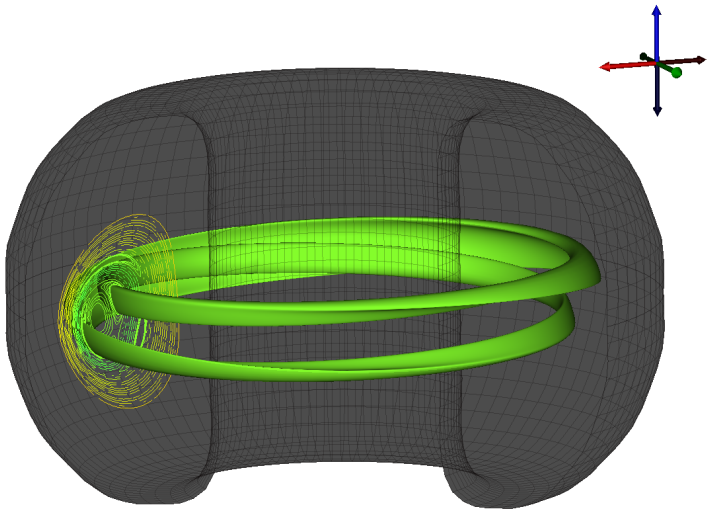

Figure 3.2: 3-Dimensional illustration of m/n = 2/1 magnetic island (from [26], generated using the techniques described in [27])

3.3.3 Edge-Localized Modes

A high-confinement (H-mode) regime can be induced in strongly heated tokamak plasmas after crossing a critical power threshold [28]. ITER, and likely all future reactors will operate in this mode, which is characterized by an improved energy confinement time, typically double or more that during normal operation, or low-confinement mode (L-mode). During H-mode, there are immense temperature and pressure gradients in the edge plasma region, known as the pedestal. The pedestal provides a free energy source for large-scale, explosive instabilities known as edge localized modes (ELMs), which eject energetic particles [29]. The projected heat loads from these events will be sufficient to melt plasma-facing components in fusion-relevant conditions [30]. The physical mechanism behind ELMs has not yet been determined.

CHAPTER 4

RESONANT MAGNETIC PERTURBATIONS

Application of small (on the order of 0.01% of the toroidal field strength) radial magnetic fields which have the same helicity as a specific flux surface can have strong effects on the stability and transport properties of a tokamak plasma. These resonant magnetic perturbations (RMPs) have been studied on numerous devices, including STOR-M, where Mirnov oscillations (a signal of magnetic islands) were strongly damped and plasma confinement improved by their use [13].

The effects RMPs could have on the surfaces with which they are resonant, and consequently the whole plasma, were first seen on the PULSATOR tokamak [31]. It possessed a set of m/n = 2/1 windings that were intended to improve the start-up condition of the device. It did not work as intended, but rather stimulated disruptions at high currents. At lower currents these disruptions did not appear but instead there was a strong reduction in the m/n = 2/1 mode amplitude (a decrease in island width). This reduction allowed for long, high-density plasma pulses [31, 32]. Many experiments followed on other devices, with similar results for different tearing modes (m/n = 1/1, 3/1, 3/2, 4/2) [33, 34, 35, 36, 37, 38, 39, 40, 41, 42, 43].

4.1 Static RMP

This partial or complete mode suppression has continued with recent experiments, showing strong dependence on magnetic island rotational frequency [44] and phase [45] with respect to applied perturbations. Different density regimes were found where the RMP effect bifurcated. At low densities, RMPs were seen to suppress both mode amplitude/island width and rotational frequency. At higher densities, stabilization still occurred but mode frequency remained constant [23]

The effect RMPs have is also largely determined by their amplitude. In addition to the error field of a tokamak, it is possible for large magnetic islands to become locked to RMPs [23, 46]. If

the applied RMP is stationary this will lead to a severe loss in confinement and likely a disruption, as discussed in Section 3.3. Smaller amplitudes result in partial mode suppression and moderate strength RMPs have demonstrated complete tearing mode suppression [47]. After a certain density dependent threshold large amplitude RMPs will mode-lock existing islands, causing them to grow, or induce magnetic tearing and the formation of magnetic islands where none previously existed [23]. This is known as mode penetration, and is resisted by plasma flow and counter-currents [48]. The transition point between suppression and mode-locking regimes has also been found in theoretical treatments and numerical modelling [49] which also predicated the experimentally observed requirement of perturbations to be resonant for mode penetration to occur. While island suppression has clearly been demonstrated on multiple devices, further study is needed to better understand and be able to predict the situations leading to suppression or mode-locking.

An island rotating at low frequency is more likely to experience error field mode-locking, with a subsequent plasma disruption. It is expected that this will occur more easily in a large fusion reactor like ITER (due to the slower flows and island frequencies) than in current experimental devices, as will mode penetration [50]. RMPs can be used to intentionally induce magnetic reconnection and generate magnetic islands in order to study error-field and frequency limits for future devices.

As magnetic islands rotate, a static RMP will alternate between being in-phase and out-of-phase with an island's radial field. For small amplitude RMPs, the EXTRAP group demonstrated both tearing mode amplification and suppression, as well as acceleration and deceleration, depending on this phase difference [45]. Larger amplitudes produced the expected mode-locking, and revealed more about the nature of this process. As the mode frequency decreased, it did so in steps corresponding to the mode passing through the amplification and slowing-down region (RMP and mode in-phase). Despite complete suppression when out-of phase, the average mode amplitude was increased.

4.2 Rotating RMP

Experiments on J-TEXT utilized RMP fields that rotated with respect to the vacuum vessel and saw improved confinement when the rotation frequency of the RMP was larger than the natural frequency of the island they targeted [51]. The reverse was true when applying RMP of a lower

relative frequency.

Rotating RMPs on TEXTOR were seen to have a stabilizing effect if the direction of their rotation was opposite to the plasma current direction, and a destabilizing one if the rotations were in the same direction [52]. In the same experiments, the threshold field for mode penetration was minimum when the RMP's rotational frequency matched the natural mode frequency.

When an RMP rotates at a similar frequency as a tearing mode, the mode can easily lock to the RMP and be forced to rotate together with it [53]. A theoretical examination of magnetic islands in geometry similar to STOR-M 's has shown that for moderate amplitudes, islands resist locking to rotating RMPs when the rotational frequency mismatch is significant [54]. Ramping up RMP rotation velocity, these simulations showed that islands lock at about half the natural mode frequency, and are able to be spun up to around three times their natural frequency before unlocking. The spin-up of mode frequencies may prove to be an effective method of controlling island growth via induced eddy currents in the vacuum vessel.

4.3 RMP Effect on ELMs

In order to achieve the relevant performance levels, fusion reactors will be required to operate in the H-mode regime. However, development of a commercial rector will depend upon solving the problem that accompanies H-mode, the enormous heat loads released from ELMs.

RMPs represent the most likely solution. Perturbations that are resonant with the edge region can enlarge islands there and cause pedestal magnetic field stochasticization, where magnetic islands overlap and field lines wander randomly [55, 56]. This degrades local confinement and decreases the pressure gradient typical in H-mode pedestals. The pedestal itself is maintained and confinement in the core plasma is not significantly affected.

For high collisionality, RMPs lower the threshold energy at which ELMs occur, and as a result they become more frequent but contain less energy, meaning that the heat load is spread out in time. This mitigation has been reproduced on multiple devices [57, 58, 59, 60, 61, 62]. Strong amplitude RMPs can result in lower collisionality in the pedestal due to the induced density pump-out [30]. This can completely suppress ELMs [56, 63, 64, 65, 66].

STOR-M possesses a limiter which projects into the outer plasma confinement region and

collects escaped particles, limiting plasma-chamber contact and sputtering. Fusion reactors will use a divertor instead, where heavier particles (the reaction products) and any others that escape confinement will be collected. ELMs can cause extreme heating in a small localized area on these divertors. In addition to the time spread of the heat load from ELMs, RMPs can induce strike point splitting, spreading the heat load over a larger area [67, 24, 68, 69],

These results have led to the inclusion of a set of RMP coils for the purposes of ELM control in the ITER baseline design [70, 71].

CHAPTER 5

SADDLE COIL DESIGN

A helical RMP coil (0.1 Ω, 14.4 μH) was previously installed on STOR-M and is used to produce stationary perturbations. Its layout and poloidal mode spectrum can be seen in Figure 5.1.

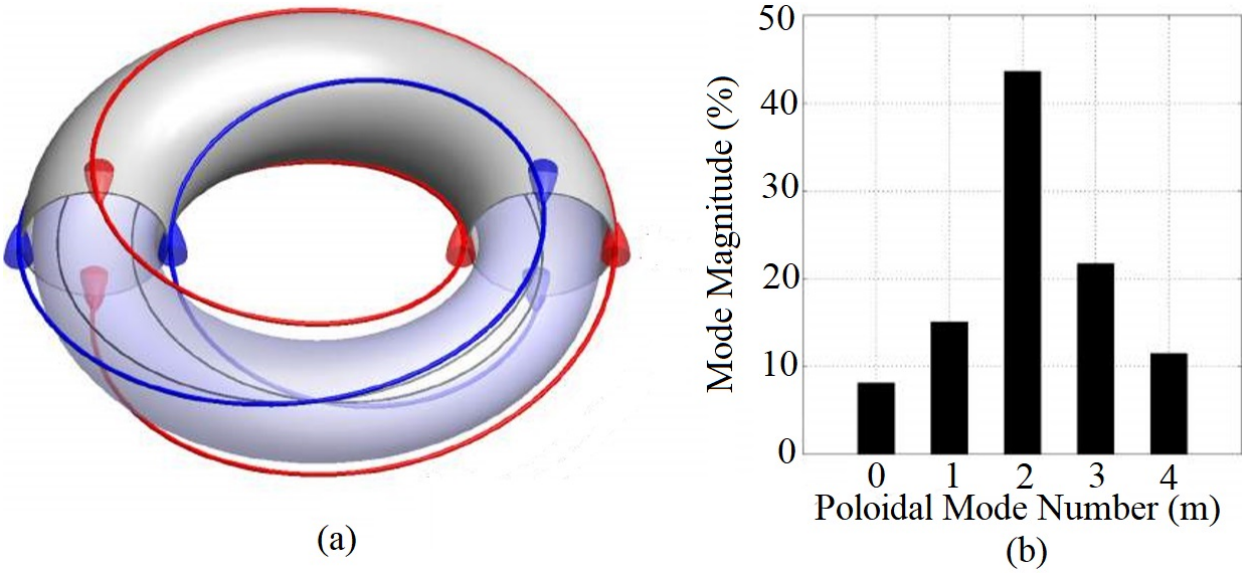

Figure 5.1: Helical RMP Coil (a) Double-winding layout and (b) the poloidal mode spectrum generated at the plasma edge (from [72])

To force an RMP pulse to rotate around the vessel a series of discrete coils need to be used instead. The magnetic field produced by a coil set can be written in the same form as that of magnetic islands (Equation 3.27), and similarly, its helicity can be represented by m and n toroidal and poloidal mode numbers. The helical coil was constructed to create a mainly m/n = 2/1 magnetic field. This is because the dominant natural MHD mode present in STOR-M corresponds to spatial mode numbers m/n = 2/1, and so it is this helicity the discrete coils must also match in order to be resonant. Using a larger number of coils purer modes can be obtained, however the many ports and diagnostics already present on STOR-M limit the potential positions and number of coil arrays.

5.1 Principles of Mode Calculation

Magnetic field and mode calculations were performed to test various coil layouts. A suite of scripts to do this had previously been developed by undergraduate students for their research project [73]. These were modified to allow for various numbers of coils in the poloidal direction and an additional script was implemented in order to easily display the results of the calculations. Due to spatial constraints on the inboard, or high-field side of most tokamaks, saddle coils have usually been limited to the top, bottom, and outboard, or low-field sides of the chamber. Given the number of coils and their geometries as inputs, one of the scripts generates a layout of evenly distributed (in the toroidal direction) coils at the poloidal locations specified. The magnetic field due to the coils is calculated by another script using the Biot-Savart Law,

$$\mathbf{B}(\mathbf{r}) = \frac{\mu_o}{4\pi}\int_C \frac{Id\mathbf{l}(\mathbf{r'})\times(\mathbf{r}-\mathbf{r'})}{|\mathbf{r}-\mathbf{r'}|^3} \tag{5.1}$$

where here $\mathbf{r}$ represents the general position vector in Cartesian coordinates, and the path, C, is described by the coil geometry (the thin wire approximation is used, and is valid at the relevant distance far from coils). $d\mathbf{l}(\mathbf{r'})$ is the tangent vector to C at $\mathbf{r}-\mathbf{r'}$.

The radial magnetic field created by the RMP coils at a certain distance from the major axis can be written in the same form as the magnetic islands' fields (Eq. 3.27). For a set radial distance, the magnetic field generated by the coils at a specific toroidal or poloidal location, ϕ_0 or θ_0 respectively, and at a specific time t_0, can be written as,

$$B_r(\theta,\phi_0,t_0) = \Sigma\left[B_{r_0mc}\cos(m\theta) + B_{r_0ms}\sin(m\theta)\right] \tag{5.2}$$

$$B_r(\theta_0,\phi,t_0) = \Sigma\left[B_{r_0nc}\cos(n\phi) + B_{r_0ns}\sin(n\phi)\right] \tag{5.3}$$

The non-normalized mode amplitudes at those specific radial and toroidal/poloidal positions are:

$$B_{r_0m} = \sqrt{B_{r_0mc}^2 + B_{r_0ms}^2} \tag{5.4}$$

$$B_{r_0n} = \sqrt{B_{r_0nc}^2 + B_{r_0ns}^2} \tag{5.5}$$

which are computed using the Fourier series coefficients:

$$B_{r_0mc} = \frac{1}{\pi}\int_0^{2\pi} \cos(m\theta) B_r(\theta, \phi_0, t_0) d\phi \qquad B_{r_0ms} = \frac{1}{\pi}\int_0^{2\pi} \sin(m\theta) B_r(\theta, \phi_0, t_0) d\phi \tag{5.6}$$

$$B_{r_0nc} = \frac{1}{\pi}\int_0^{2\pi} \cos(n\phi) B_r(\theta_0, \phi, t_0) d\phi \qquad B_{r_0ns} = \frac{1}{\pi}\int_0^{2\pi} \sin(n\phi) B_r(\theta_0, \phi, t_0) d\phi \tag{5.7}$$

These integrations were performed numerically in Matlab, as were the magnetic field calculations. All of the figures in this section were generated with calculations using STOR-M's geometry. As shown earlier, its major radius is 46 cm. The listed value of minor radius, 12.5 cm, is that of the plasma column, as set by the limiter. RMP coils will be placed on the exterior of the vacuum chamber, at approximately r = 17 cm. The magnetic field and mode calculations shown here were performed at the r = 7 cm surface. This is the location of the q = 2/1 magnetic surface in a standard STOR-M discharge.

To produce the desired mode it was seen that it is ideal for an array of coils to cover as much of the chamber in the poloidal direction as possible. The presence of the vacuum chamber's ports prevents this at many toroidal locations and practically each coil can be about 20 cm long in the poloidal direction. Accordingly, the examples in this section are based on coils with that dimension. The variables that strongly affect the modes generated and over which the greatest control can be exercised are the number of coils in the toroidal direction and their individual spans in that direction.

Coils span certain toroidal and poloidal angles, so neglecting curvature, they are roughly trapezoidal or square (if centered on $\theta = 0, \pi$). Coil sizes are indicated in terms of the outboard coil width, at $\theta = 0$. So for example, a 20 cm outboard coil width indicates that all the coils at that toroidal location span 18.2 degrees in the toroidal direction. Again, each of the coils are 20 cm long in the poloidal direction, or span 67.4 poloidal degrees.

To create a rotating perturbation alternating currents with different relative phases can be passed through the discrete coils. Figure 5.2 depicts the counter-clockwise rotation of a magnetic field generated by such a system over four snapshots in time.

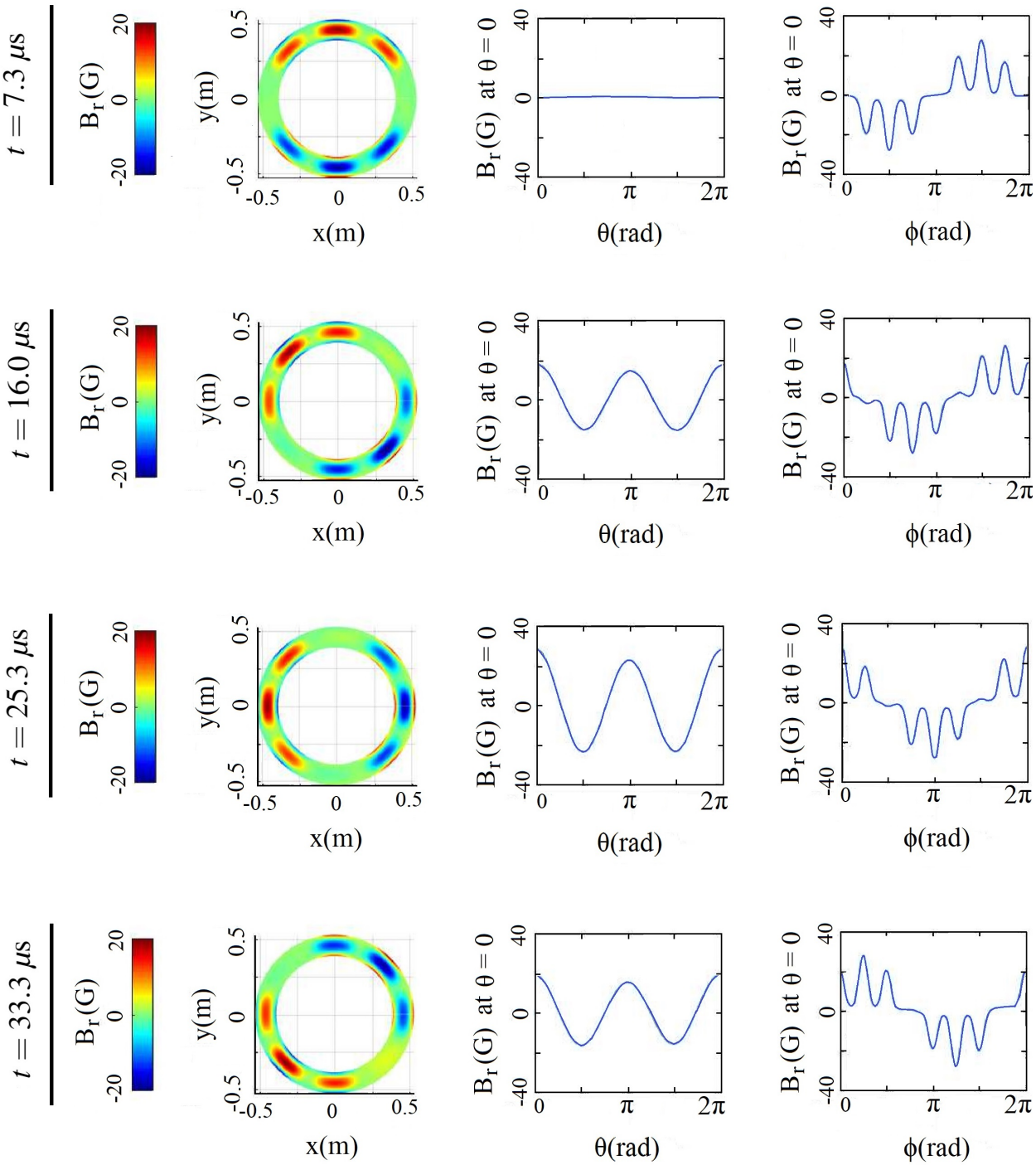

Figure 5.2: Snapshots of simulated radial magnetic field produced at $r = 7$ cm with eight, 20 cm wide (at the outboard side) 4-coil arrays by 1000 A current driven at 15 kHz. Left to right: top-view, poloidal distribution, toroidal distribution.

5.2 Mode Calculations

Research groups that have investigated rotating RMPs have in the past been limited to installing coils on the top, bottom, and outboard sides of the vacuum vessel due to the inaccessibility of the inboard region. Initially it was thought it would be necessary to do the same on STOR-M, for the same reason. Figure 5.3 shows example magnetic field and mode calculations performed using 4 evenly spaced arrays of 3 coils at these poloidal positions, where curent directions have been chosen to create a mainly m/n = 2/1 mode. Comparing **(a)** and **(b)**, or **(c)** and **(d)**, it is seen that doubling the toroidal span of the coils has minimal impact on the modes. The wider coils do result in a small improvement, but it is not clear at the scale shown. However, doubling the number of arrays reduces the amplitude of most of the $n \neq 1$ components. The contributions to the magnetic field of modes with $n \geq 7$ are lower in amplitude than the desired m/n = 2/1 mode. And, the surfaces with which they are resonant are deeper in the plasma core and will experience greater attenuation due to plasma flows. They are unlikely therefore to induce unwanted, high-n magnetic island formation. For all the simulations using top, bottom, and outboard coils, n = 1 modes are significant.

Since one plasma discharge in STOR-M is short (about 30ms) resistive heating of the RMP coils due to one shot is not particularly high. The charging time required by the tokamak's main capacitor banks is several minutes, which is sufficiently long to allow the use of a relatively small gauge wire for the RMP coils and still avoid them heating up significantly over the course of many shots. Using a thin wire, it is possible to place an RMP coil on the inboard side of the tokamak, between the vacuum vessel and toroidal magnetic field magnets. As shown in Figure 5.4, the addition of an inboard coil all but eliminates the m = 1 modes in the RMP field. Then nearly all the power used to drive the coil currents can be utilized to target the m/n = 2/1 mode and there is less risk of sidebands creating undesirable effects. Again, modal analysis shows that when spanning the same surface area, using more arrays rather than wider ones produces a purer targeted mode.

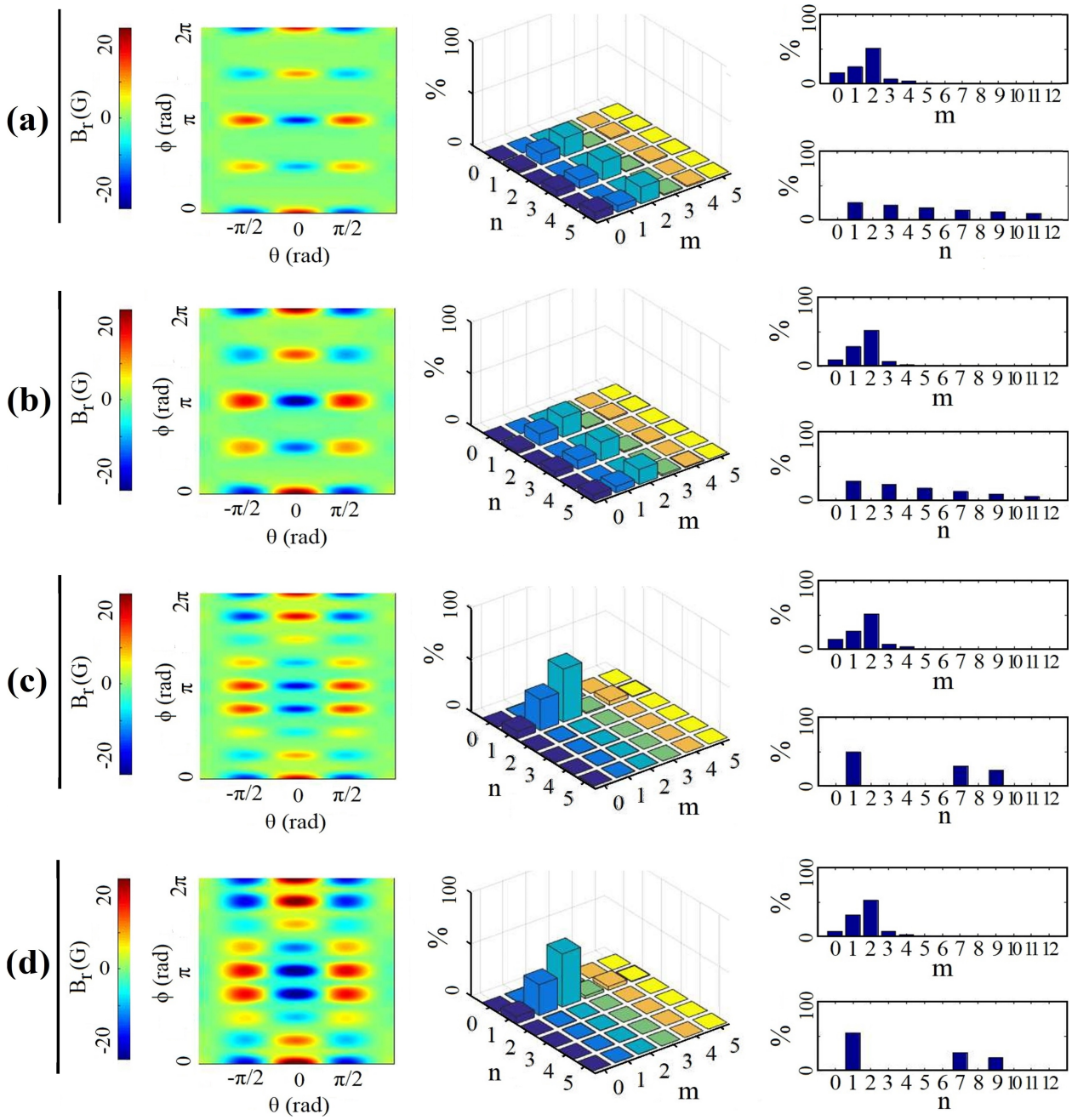

Figure 5.3: Left: Snapshot of radial magnetic field produced at $r = 7$ cm by 3-coil arrays with a coil current of 1000 A. Middle: Dominant m/n mode amplitudes. Right: Total contributions from individual m and n components.

(a) Arrays at 4 toroidal locations. Outboard coil width: 10 cm

(b) Arrays at 4 toroidal locations. Outboard coil width: 20 cm

(c) Arrays at 8 toroidal locations. Outboard coil width: 10 cm

(d) Arrays at 8 toroidal locations. Outboard coil width: 20 cm

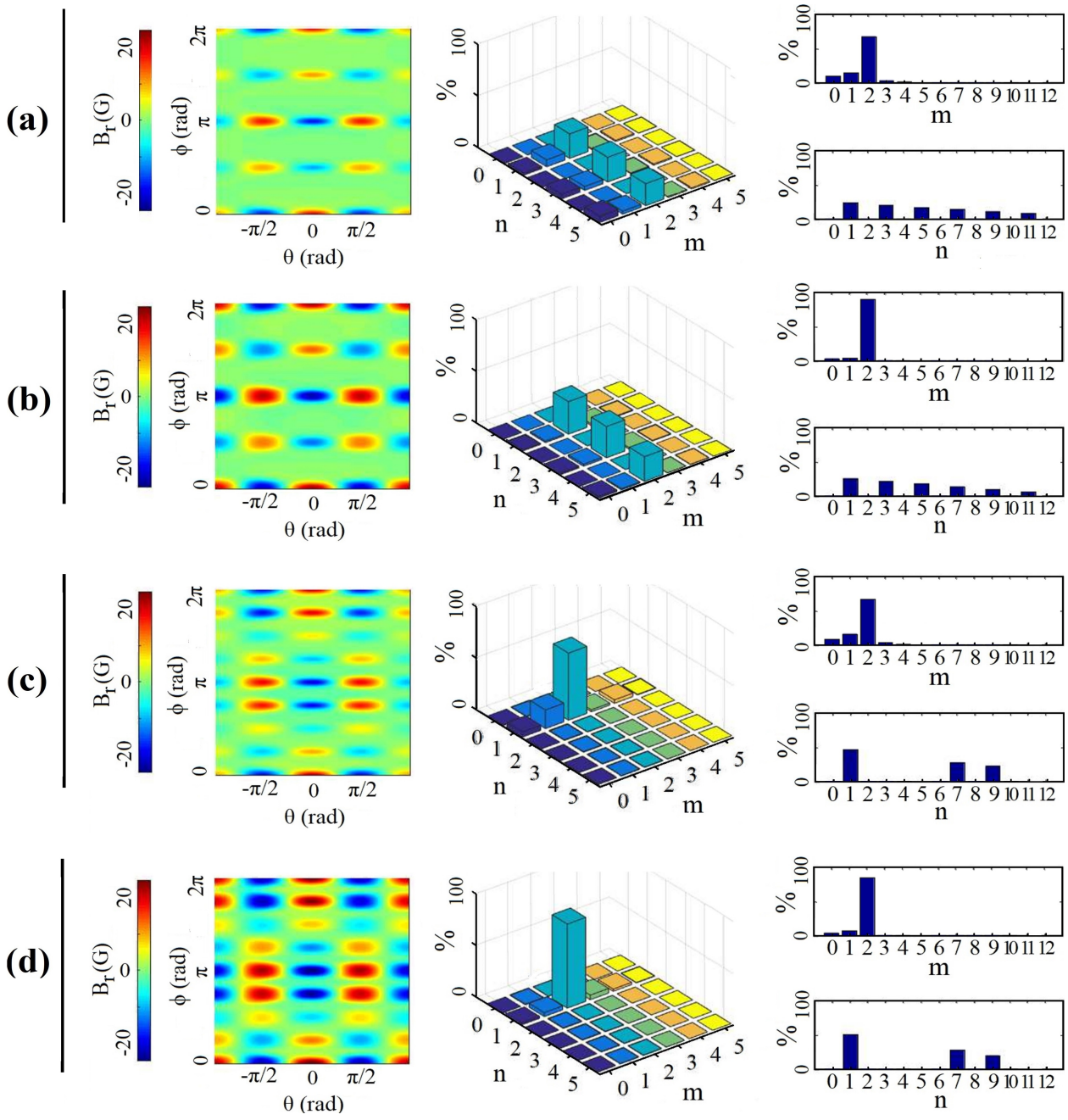

Figure 5.4: Left: Snapshot of radial magnetic field produced at $r = 7$ cm by 4-coil arrays with a coil current of 1000 A. Middle: Dominant m/n mode amplitudes. Right: Total contributions from individual m and n components.

(a) Arrays at 4 toroidal locations. Outboard coil width: 10 cm

(b) Arrays at 4 toroidal locations. Outboard coil width: 20 cm

(c) Arrays at 8 toroidal locations. Outboard coil width: 10 cm

(d) Arrays at 8 toroidal locations. Outboard coil width: 20 cm

5.3 Physical Design of Coils

To reduce the effect of the m/n = 1/1 mode and ensure that observed effects on the plasma were due to the m/n = 2/1 mode, all arrays were constructed with four coils in the poloidal direction (top,bottom, outboard, inboard). Using a larger number of arrays distributed on at evenly spaced toroidal locations decreases the strength of the n < 1 modes, however it is very challenging to fit the arrays to the vacuum vessel in the limited space available. Additionally, these modes are not resonant with any significant rational surface so their effects should be unnoticeable. Many more configurations than shown were explored, including the use of many coils in the poloidal direction to enable higher m modes, but it was decided to use sixteen coils in total, at four toroidal and four poloidal positions. This design can create relatively pure m/n = 2/1 modes and there were four (evenly spaced) comparably accessible spaces on the vessel surface to fit the coils to. The positioning of the coils can be seen in Figure 5.5.

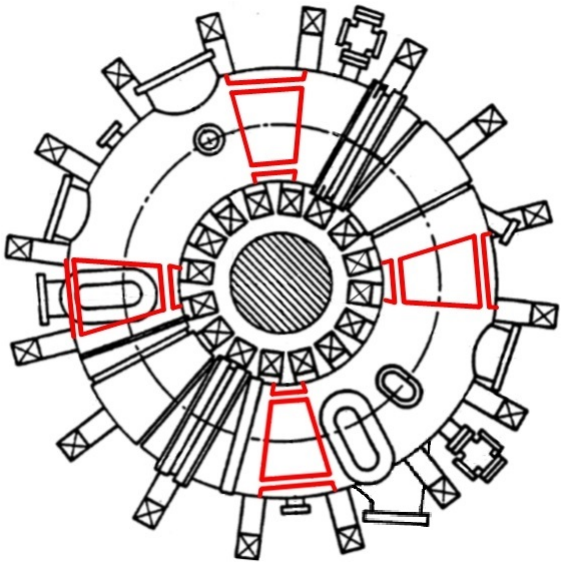

Figure 5.5: Discrete coil layout

Insulating, non-magnetic coil frames, made of low-density polyethylene, were constructed and are used to shape the coils and secure the coil arrays to the vacuum vessel exterior wall. The coils are made of single loops of 14 gauge insulated, stranded wire. The coil terminals can be accessed from underneath the tokamak, and it is possible to easily reconfigure their connections. This can be done to achieve different total inductances or to alter individual coil current directions

for the creation of different modes, such as m/n = 1/1 or mixed modes. In the standard set-up, the four coils of one array are wired in parallel to limit inductance, and the top and bottom coils have reverse current directions with respect to the inboard and outboard coils.

The actual coils span 16.4 degrees toroidally (the outboard coil being 18 cm wide) and 67.4 degrees poloidally (each coil being 20 cm long). The exception to this is the array at the same toroidal location as an optical chamber port. This array's top and bottom coils are approximately 4 cm longer in the poloidal direction. Its inboard and outboard coils are shorter by a similar amount. These adjustments were necessary due to the presence of the port. The magnetic field and mode simulations of the real coils are shown in Figure 5.6.

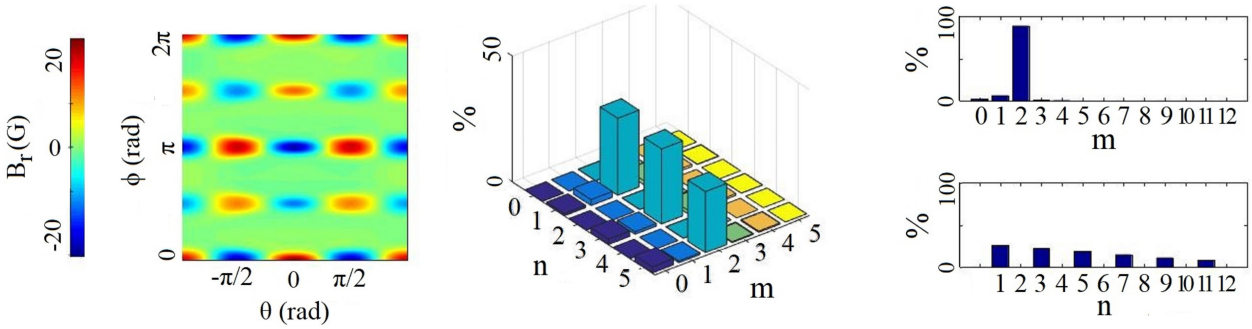

Figure 5.6: Left: Snapshot of simulated radial magnetic field produced at $r = 7$ cm by the installed 4-coil arrays with a coil current of 1000 A. Middle: Dominant m/n mode amplitudes. Right: Total contributions from individual m and n components.

CHAPTER 6

POWER SUPPLY

6.1 Design Requirements

The circuit topology chosen for the rotating RMP power supply is the H-bridge, which can create sinusoidal waveforms. It consists of four semiconductor switches and the load (coils and a resonant capacitor). The polarity of a capacitor bank discharge is switched at the same frequency as the load's natural frequency by alternately turning on/off the top-left (S1) and bottom-right (S4), then top-right (S2) and bottom-left IGBTs (S3) switches in Figure 6.1. The load is then driven at its resonant frequency, giving the desired alternating current. Different frequencies are achieved by adjusting the capacitance in series with the coils. The switches are controlled by frequency-matched gated square waves, created by an FPGA (Field Programmable Gate Array). A trigger signal to the FPGA controls when the system fires.

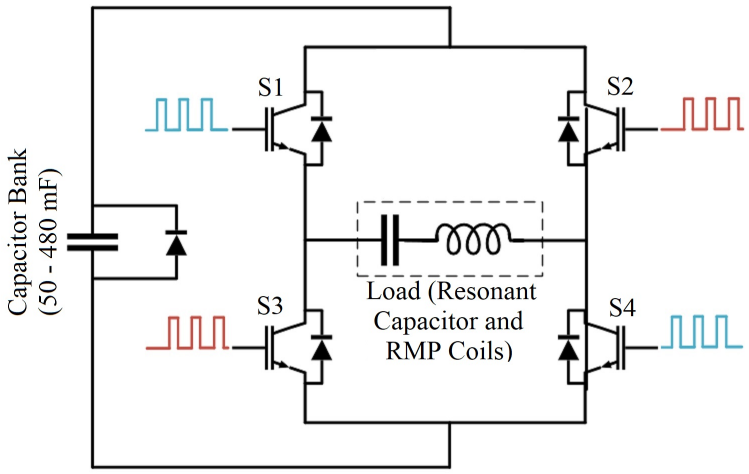

Figure 6.1: Basic circuit topology and out-of-phase gate signals

It was previously seen on STOR-M that static RMP experiments with a helical coil required

currents from 600 to 1000 A to achieve mode penetration, depending on the q profile [72]. Considering this, and since for dynamic RMP there will be attenuation through the chamber wall due to shielding from eddy currents, 1000 A was taken as the minimum current requirement for the new system. Due to STOR-M's geometry and operating parameters, the magnetic islands in the tokamak rotate in the 25 to 45 kHz range. While it would be ideal to be able to create rotating perturbations to match, and even surpass these frequencies, current power-semiconductor switch technology limits the potential operating frequency to about 25 kHz for the required current.

Coils that are driven in phase or 180 degrees out-of-phase can be connected to the same bridge meaning that only two will be required to drive a rotating m/n = 2/1 perturbation (or one bridge for a non-rotating 2/1 perturbation).

6.2 Mathematical Modeling of H-Bridge

In order to predict the peak currents and voltages reached and importantly, the effect of different component values on those parameters, the H-bridge circuit was modeled mathematically.

After the capacitor bank has been charged, when two of the IGBT switches of the rotating RMP power supply are first turned on it can be modeled by an equivalent RLC circuit:

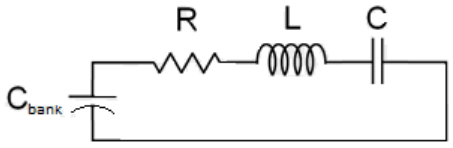

Figure 6.2: Equivalent circuit during first half-wave

Travelling around the loop, Kirchhhoff's voltage law gives the following equation:

$$V_{Bank} - V_R - V_L - V_C = 0 \tag{6.1}$$

or

$$V_{Supply} - \frac{1}{C_{Bank}} \int i \cdot dt - iR - L\frac{di}{dt} - \frac{1}{C} \int i \cdot dt = 0 \tag{6.2}$$

and differentiating with respect to time and reorganizing,

$$\frac{d^2i}{dt^2}+\frac{R}{L}\frac{di}{dt}+\frac{i}{L}\Big(\frac{1}{C_{Bank}}+\frac{1}{C}\Big)=0 \tag{6.3}$$

Defining $\alpha=\frac{R}{2L}$ and $\omega_0=\sqrt{\frac{1}{L}\Big(\frac{1}{C_{Bank}}+\frac{1}{C}\Big)}$,

$$\frac{d^2i}{dt^2}+2\alpha\frac{di}{dt}+\omega_0^2 i=0 \tag{6.4}$$

For $\frac{\alpha}{\omega_0}<1$, or underdamping, this has the general solution:

$$i(t)=Ae^{-\alpha t}\sin(\omega_d t)+Be^{-\alpha t}\cos(\omega_d t) \tag{6.5}$$

where $\omega_d=\sqrt{\omega_0^2-\alpha^2}$ is the damped frequency. Current will be zero at turn on and practically zero when switching so $B=0$ and all that remains is to determine the value of A, which can be found by examining V_L,

$$V_L(t)=L\frac{di}{dt}=LA_1[-\alpha e^{-\alpha t}\sin(\omega_d t)+\omega_d e^{-\alpha t}\cos(\omega_d t)] \tag{6.6}$$

$$V_L(0)=LA_1\omega_d \tag{6.7}$$

$$=V_{Bank}(0)-V_C(0)-V_R(0) \tag{6.8}$$

$$=V_{Supply} \tag{6.9}$$

$$A_1=\frac{V_{Supply}}{\omega_d L}=\frac{V_{Supply}}{\sqrt{L\big(\frac{1}{C_{Bank}}+\frac{1}{C}\big)-\frac{R^2}{4}}}\approx\frac{V_{Supply}}{\sqrt{\frac{L}{C}-\frac{R^2}{4}}} \tag{6.10}$$

So,

$$i(t)=\frac{V_{Supply}}{\sqrt{L(\frac{1}{C_{Bank}}+\frac{1}{C})-\frac{R^2}{4}}}e^{-\alpha t}\sin(\omega_d t) \tag{6.11}$$

is the completely determined current flowing in the circuit , but only before switching occurs, at which point the equivalent circuit shown above changes and needs to be re-evaluated based on the new "initial" conditions.

The following plots show the maximum currents reached during the first half-wave of the current waveform for realistic potential RLC values and $C_{Bank}=480$ mF, $V_{Supply}=400$ V.

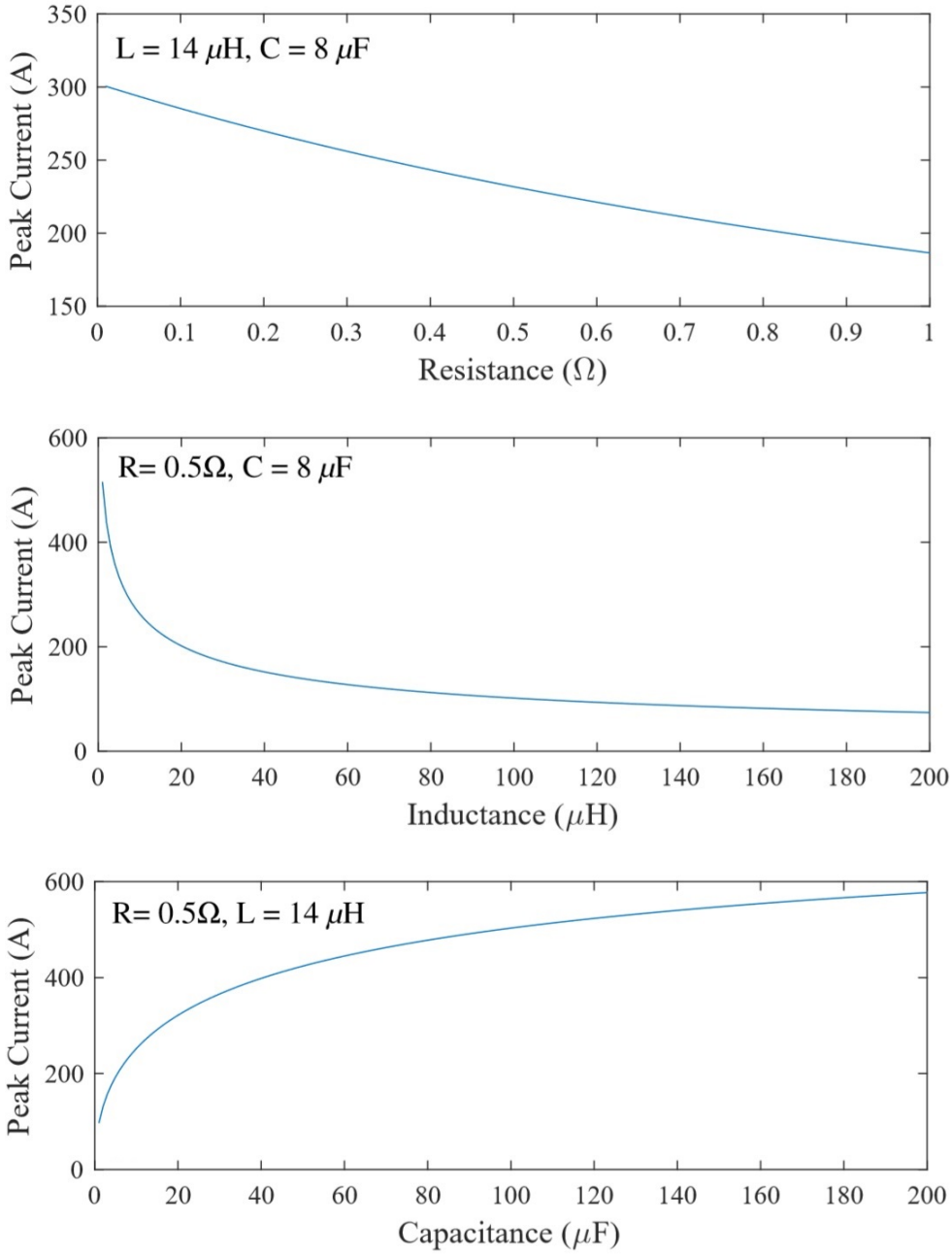

Figure 6.3: Dependencies of peak current reached during the first half-wave

Clearly, in the range of the realistic load resistance, inductance, and capacitance values, for a given charging voltage the inductance and capacitance ratio, $\frac{L}{C}$, dominates in terms of peak current.

At the end of the first half-wave the resonant capacitor will have charged to:

$$V_C\left(\frac{\pi}{\omega_d}\right) = \frac{1}{C}\int_0^{\frac{\pi}{\omega_d}} i \cdot dt \tag{6.12}$$

$$= \frac{1}{C}\int_0^{\frac{\pi}{\omega_d}} \frac{V_{Supply}}{\omega_d L} e^{-\alpha t} sin(\omega_d t) dt \tag{6.13}$$

$$= \frac{V_{Supply}}{\omega_d LC}\left[\frac{1}{1+\frac{\omega_d^2}{\alpha^2}}\left(\frac{-1}{\alpha}e^{-\alpha t}\sin(\omega_d t) - \frac{\omega_d}{\alpha^2}e^{-\alpha t}\cos(\omega_d t)\right)\right]\Bigg|_0^{\frac{\pi}{\omega_d}} \tag{6.14}$$

$$= \frac{V_{Supply}}{(\alpha^2+\omega_d^2)LC}\left(1+e^{-\frac{\alpha}{\omega_d}\pi}\right) \tag{6.15}$$

and the capacitor bank voltage will have decreased:

$$V_{Bank}\left(\frac{\pi}{\omega_d}\right) = V_{Bank}(0) - \frac{1}{C_{Bank}}\int_0^{\frac{\pi}{\omega_d}} i \cdot dt \tag{6.16}$$

$$= V_{Supply} - \frac{V_{Supply}}{(\alpha^2+\omega_d^2)LC_{Bank}}\left(1+e^{-\frac{\alpha}{\omega_d}\pi}\right) \tag{6.17}$$

The H-bridge switching equates to swapping the polarity in the equivalent circuit ($V_{Bank} \rightarrow -V_{bank}$). This occurs every time the current reaches a zero-crossing.

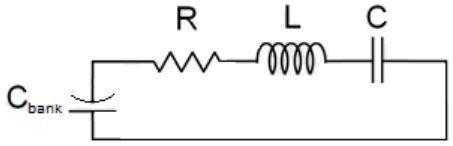

Figure 6.4: Equivalent circuit during 2nd half-wave and subsequent even half-waves

At the start time of the second half-wave, now called t = 0,

$$i(0) = 0 \tag{6.18}$$

$$V_C(0) = \frac{V_{Supply}}{(\alpha^2+\omega_d^2)LC}\left(1+e^{-\frac{\alpha}{\omega_d}\pi}\right) \tag{6.19}$$

$$V_{Bank}(0) = -V_{Supply} + \frac{V_{Supply}}{(\alpha^2+\omega_d^2)LC_{Bank}}\left(1+e^{-\frac{\alpha}{\omega_d}\pi}\right) \tag{6.20}$$

Once again,

$$V_{Bank} - V_R - V_L - V_C = 0 \tag{6.21}$$

$$V_{Bank}(0) - \frac{1}{C_{Bank}} \int i \cdot dt - iR - L\frac{di}{dt} - \frac{1}{C} \int i \cdot dt = 0 \tag{6.22}$$

which has the same form as Eq. 6.2 and the same solution: Eq. 6.6.

$$V_L(0) = LA_2\omega_d \tag{6.23}$$

$$= V_{Bank}(0) - V_C(0) - V_R(0) \tag{6.24}$$

$$= -V_{Supply} + \frac{V_{Supply}}{(\alpha^2+\omega_d^2)LC_{Bank}}\left(1 + e^{-\frac{\alpha}{\omega_d}\pi}\right) - \frac{V_{Supply}}{(\alpha^2+\omega_d^2)LC}\left(1 + e^{-\frac{\alpha}{\omega_d}\pi}\right) \tag{6.25}$$

The solution for the second half-wave (and all subsequent waves) has the same form as the first half-wave, however the constant, A, has changed (contrast with Eq. 6.10). Every time the circuit switches it must be re-evaluated based on the new initial conditions.

$$i(t) = A_2 e^{-\alpha t}\sin(\omega_d t) \tag{6.26}$$

$$A_2 = \frac{-V_{Supply}}{\omega_d L}\left[1 - \frac{1}{(\alpha^2+\omega_d^2)L}\left(1 + e^{\frac{-\alpha}{\omega_d}\pi}\right)\left(\frac{1}{C_{Bank}} - \frac{1}{C}\right)\right] \tag{6.27}$$

In general, during the n^{th} half-wave, or switch-state,

$$i(t) = A_2 e^{-\alpha t}\sin(\omega_d t) \tag{6.28}$$

$$V_C = \frac{B}{C}\sum_{i=1}^{n-1} A_i + \frac{A_n}{C}\left(\frac{e^{-\alpha t}}{1+\frac{\omega_d^2}{\alpha^2}}\right)\left[\frac{-\sin(\omega_d t)}{\alpha} - \frac{\omega_d\cos(\omega_d t)}{\alpha^2} + \frac{\omega_d}{\alpha^2}\right] \tag{6.29}$$

$$V_{Bank} = (-1)^{n+1}V_{Supply} + \frac{B}{C_{Bank}}\sum_{i=1}^{n-1}(-1)^{i+n-1}A_i \tag{6.30}$$

$$+ \frac{A_n}{C_{Bank}}\left(\frac{e^{-\alpha t}}{1+\frac{\omega_d^2}{\alpha^2}}\right)\left[\frac{-\sin(\omega_d t)}{\alpha} - \frac{\omega_d\cos(\omega_d t)}{\alpha^2} + \frac{\omega_d}{\alpha^2}\right] \tag{6.31}$$

$$\text{where, } A_n = \frac{1}{w_d L}\left[(-1)^{n+1}V_{Supply} + \frac{B}{C_{Bank}}\sum_{i=1}^{n-1}(-1)^{i+n-1}A_i - \frac{B}{C}\sum_{i=1}^{n-1}A_i\right] \tag{6.32}$$

$$B = \frac{\omega_d}{\alpha^2+\omega_d^2}\left(1 + e^{\frac{-\alpha}{\omega_d}\pi}\right) \tag{6.33}$$

Figure 6.5 shows some examples of simulated waveforms of the current driven through the coils and the voltage present across the resonant capacitor, and illustrates important considerations when selecting components for the power supply. In this figure, **(a)** is intended as a reference, while **(b)** demonstrates the impact of a doubling of load resistance, and **(c)** and **(d)** a doubling of load capacitance and inductance respectively. As previously shown, the circuit's resistance should be minimized or high charging voltages will be required, which introduces other practical implementation challenges. Additionally, the $\frac{L}{R}$ ratio needs to be such that for a given charging voltage the resonant capacitor will not be destroyed due to overvoltage.

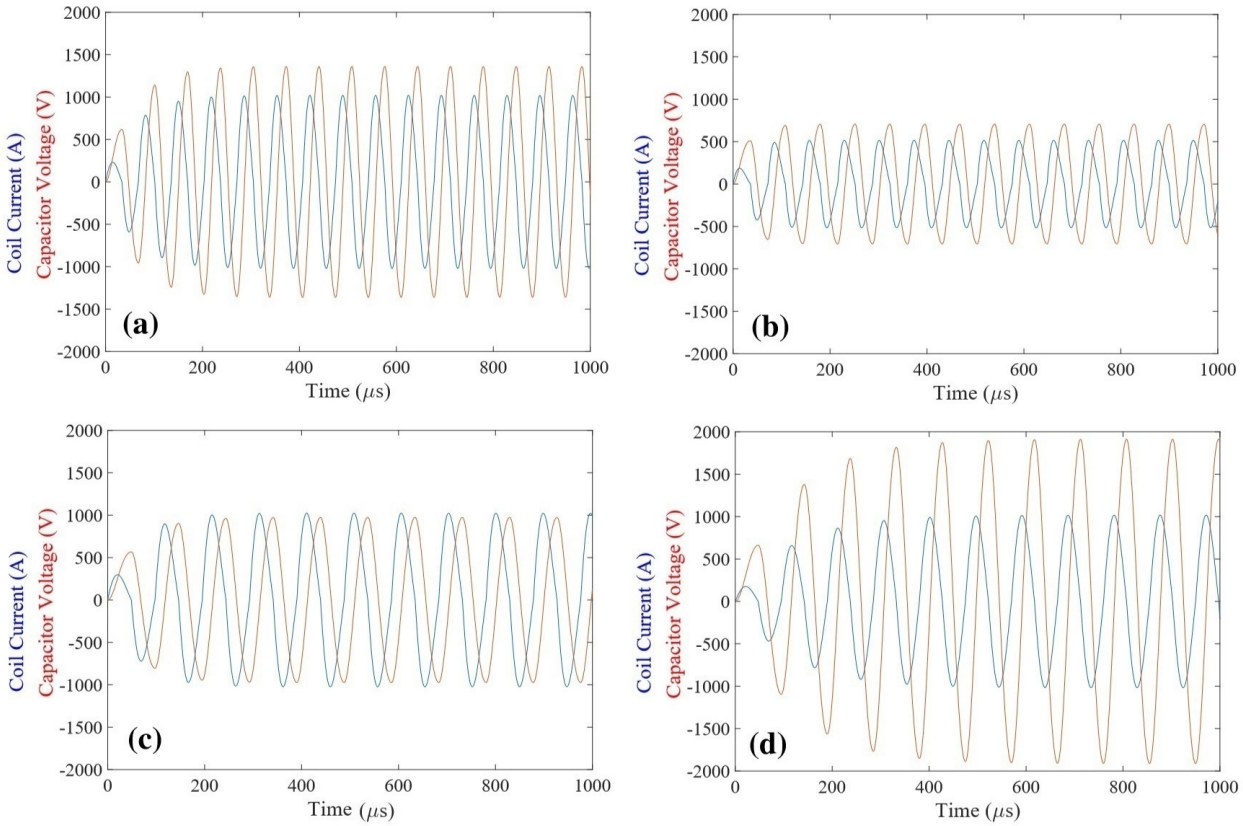

Figure 6.5: Simulated coil currents and resonant capacitor voltages for different values of load resistance, inductance, and capactiance (see Table 6.1)

Table 6.1: Input parameters and results of simulations shown in Figure 8.1

	R (Ω)	L (μH)	C (μF)	f (kHz)	Peak I (A)	Peak V_C (V)
(a)	0.5	14	8	14.8	1018	1358
(b)	1	14	8	13.9	515	705
(c)	0.5	14	16	10.5	1023	973
(d)	0.5	28	8	10.5	1017	1910

The following three plots demonstrate how the RLC values affect the maximum current reached after many cycles.There is a large difference between how the RLC values affect the first cycle's peak current, shown earlier, and the maximum current. As long as the circuit remains underdamped the main contribution to the natural frequency of the system is always due to $\frac{L}{C}$. Differently however, the maximum current reached over many cycles is almost entirely determined by the circuit's resistance. The value of $\frac{L}{C}$ determines how quickly a pulse of the system will reach that peak current.

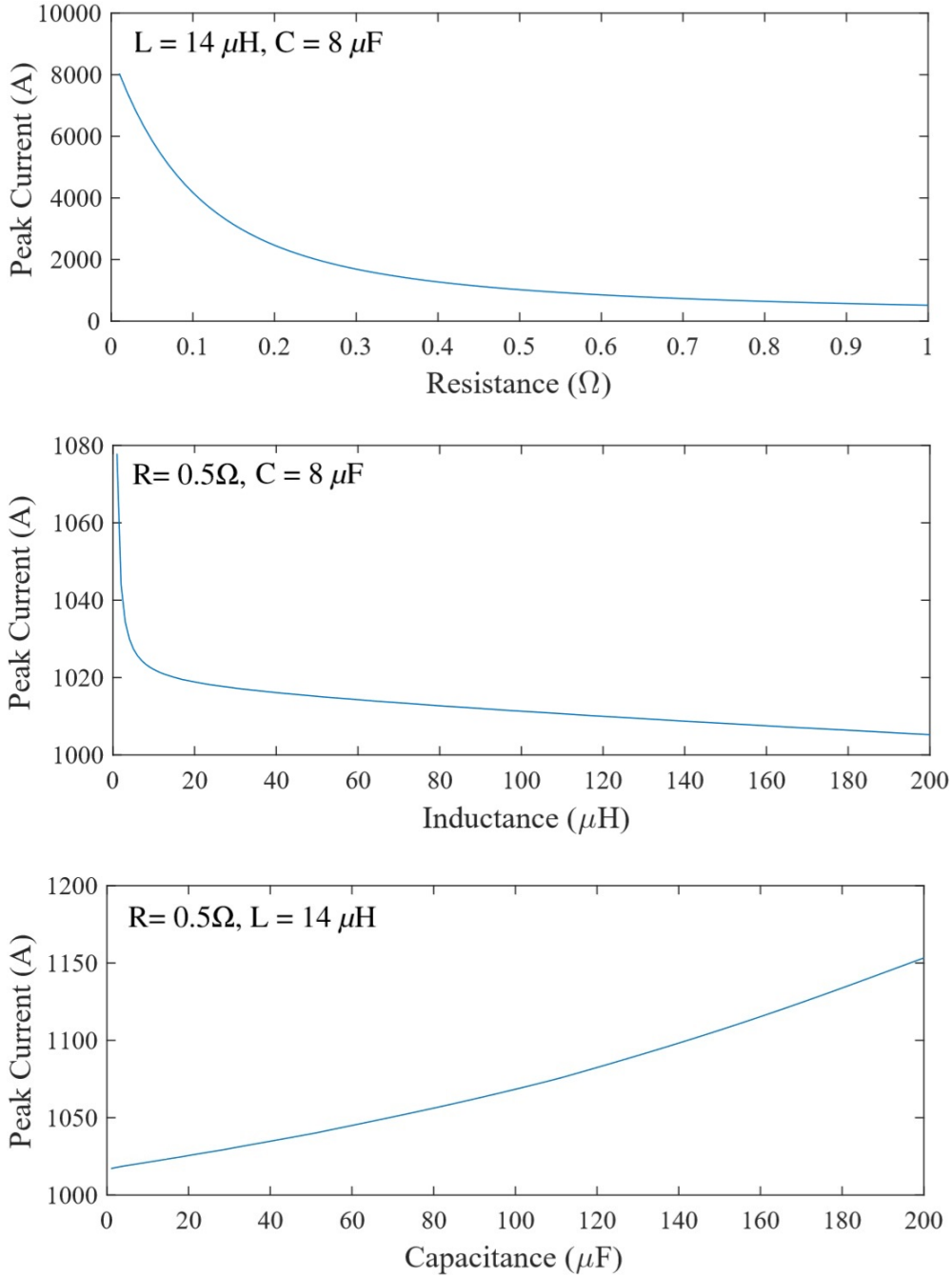

Figure 6.7: Dependencies of maximum current

6.3 Design

6.3.1 Rapid High Current IGBT Switching Considerations

Insulated-gate bipolar transistors (IGBTs) were chosen as the switches for the H-bridge. They straddle the position between high power and high frequency semiconductor switches, and their voltage-regulated gates make them relatively simple to control. The main disadvantage faced when using IGBTs is the long time their minority carriers take to enter and exit the drift region, resulting in a limited switching frequency.

Turn-on, by means of an applied gate-emitter voltage, equates to the creation of a conductive channel from the collector to the emitter. In an **N**-channel IGBT, illustrated in Figure 6.8, the gate-emitter voltage draws electrons toward the gate. This establishes a depletion region in the **P**-body and allows conduction.

In addition to the majority carriers, the electrons, part of the current flow in the drift region is due to positive ions/holes, the minority carriers, from the $\mathbf{P}^+$ injection layer. This means the device operates with a lower on-state voltage and allows for more current to be passed.

While removing the gate-emitter voltage quickly stops electrons from flowing, the holes in the drift region must recombine or are more slowly swept out due to the voltage gradient. As a result, IGBTs have a tail current which must be accounted for when switching. Though a class of IGBTs exists that has a buffer capable of modifying the recombination rate, the majority of these devices do not possess the high voltage rating needed for the RMP power supply [74].

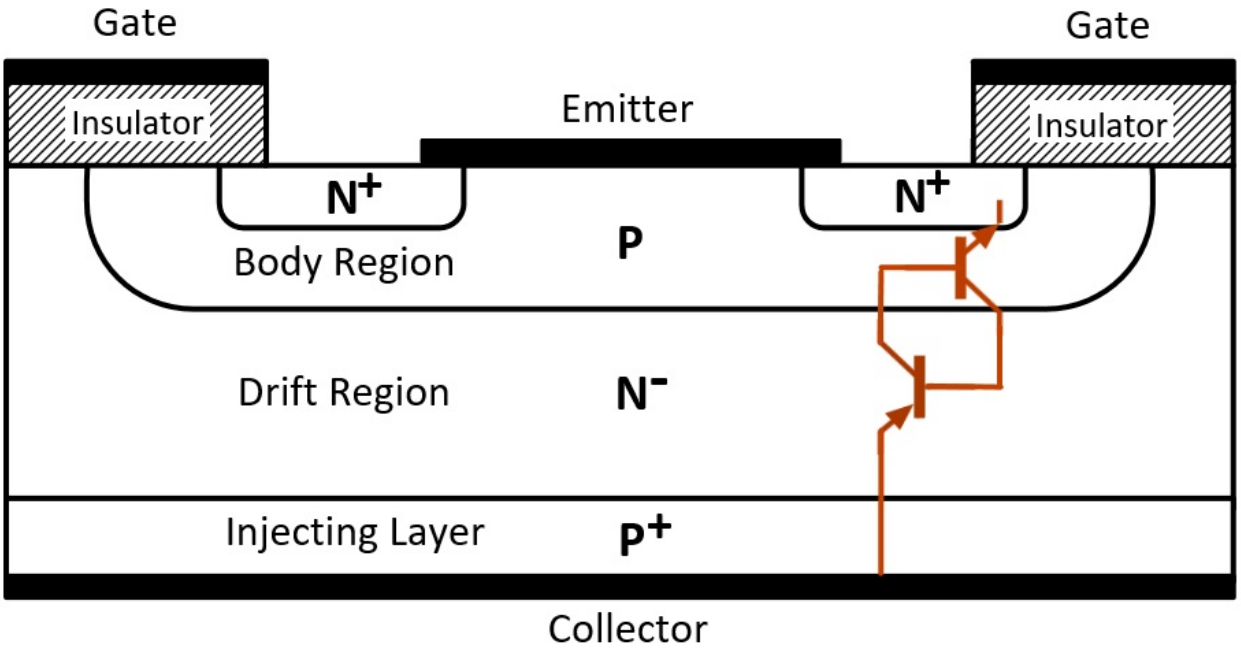

Figure 6.8: IGBT structure and internal parasitic thyristor

The other concern when developing/operating the power supply is the prevention of latch-up, the turn-on of the parasitic **PNPN** thyristor inherent to the IGBT design. Should this occur, current flow will no longer be controlled by the gate and the switch will be destroyed due to the huge power dissipation.

During normal operation, a fraction of the holes travel across the **P**-body layer, creating a lateral voltage drop due to the non-zero resistance of the body. This can forward bias the $\mathbf{N}^{+}$P junction, turning on the **NPN** transistor, and causing the latchup of the **PNPN** thyristor. See Figure 6.9. Rapid turn off causes the depletion region of the$\mathbf{N}^{-}$P junction to expand, causing more ions/holes to be collected at that junction. The escalating **PNP** collector current increases the cross-body voltage drop, affecting the **P** base of the **NPN** transistor, resulting in latchup at lower currents when fast switching than would normally be expected. This situation is avoided by operating at lower currents, where the $\mathbf{N}^{+}$P bias will be farther from the latchup threshold before turn-off.

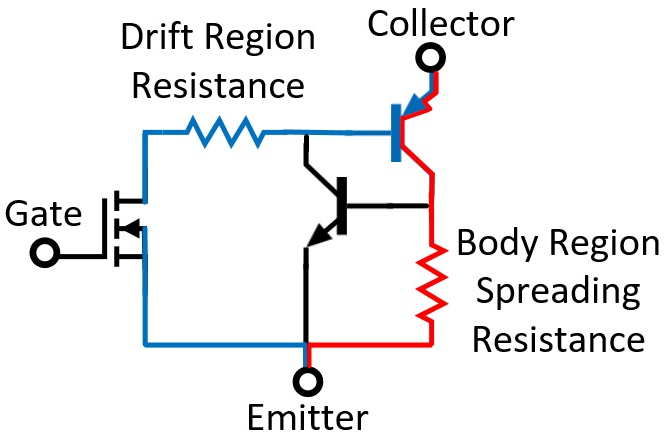

Figure 6.9: Approximate IGBT equivalent circuit. Blue: Dominant current path during normal operation. Red: Latch-up current path

In addition to the voltage breakdown threshold of the specific switches used, the switching speed and current limits imposed by the IGBT tail current and the risk of latchup are then the main determinants of the RMP system's maximum parameters. With these considerations in mind, gate drivers and a timing system were developed that allow a switching speed of 25 kHz at 1200 A. Snubbers prevent potentially destructive inductive voltage spikes at high currents and frequencies.

6.3.2 RMP Coil Induction

The orientation of the RMP coils is such that the tokamak's toroidal field lines should ideally not pass through the area bounded by the coils. However, any misalignment could potentially result in magnetic flux through the coil areas and large inductive voltages may be induced in them as a result of the enormous toroidal magnetic field. The RMP power supply would need to absorb or overcome these voltages, and prevent a reduction in driven current or even damage to the power supply.

To investigate whether this would be an issue, a mock-up expected to be reasonably similar to the final array design was installed to measure this induction. When adjusting the alignment, the maximum voltage across the ends of the coil was never more than a fraction of a volt during a standard discharge and was therefore disregarded when developing the power supply. Figure 6.10 shows waveforms of the toroidal magnetic field, plasma discharge current, and the voltage induced between the terminals of the mock-up coil.

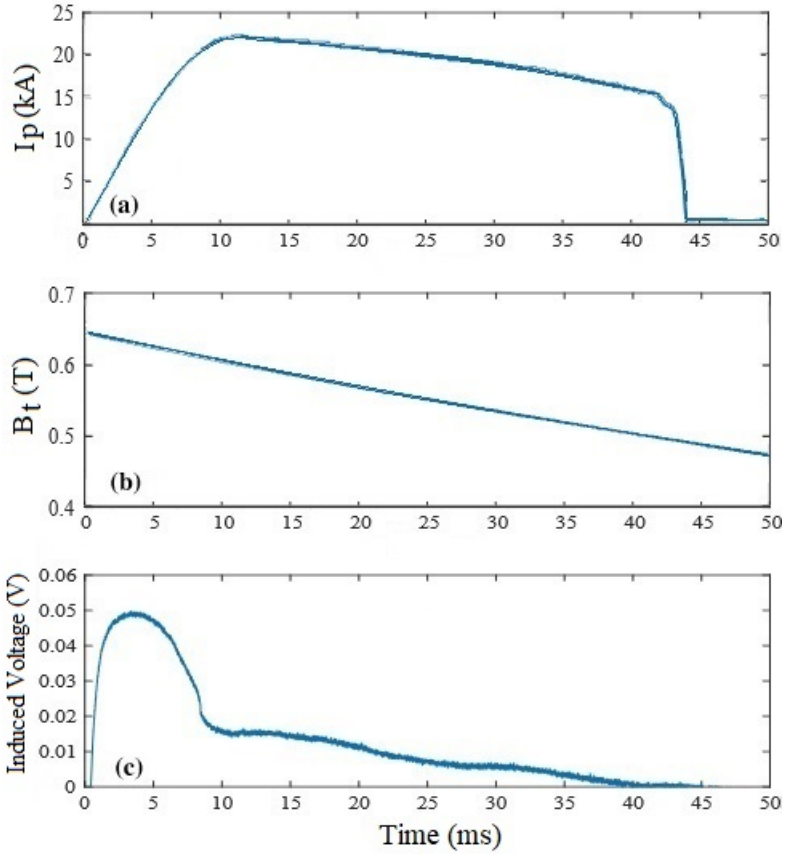

Figure 6.10: (a) Plasma current, (b) Toroidal magnetic field, (c) Voltage induced in mock-up coil due to toroidal field magnets and plasma discharge. The source inducing the voltage is mainly due to toroidal field BT

6.3.3 Gate Drivers

Commercial gate driver chips (Infineon 1EDI60I12AF) were used due to their reliability and the speed advantage of an integrated circuit. These are powered with batteries and floated at the IGBT gates, and are therefore optically isolated from the FPGA timing circuit. The gate resistors of 3.3 Ω were chosen to balance the minimization of switching time required for operation at higher frequencies and avoiding damaging voltage transients at turn-off. Four gate driver circuits were made, one for each IGBT in the H-bridge.

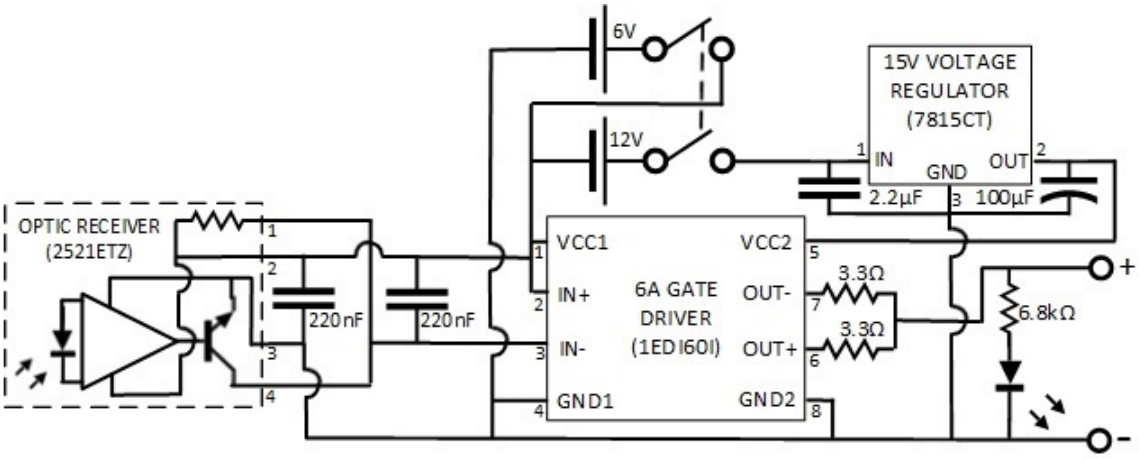

Figure 6.11: Circuit diagram of the IGBT gate drivers

6.3.4 Timing Control

The timing signals that control the gate drivers come from a Mercury Development Board (Model ME1B-200M) utilizing a Xilinx Spartan-3A FPGA connected to optical outputs. The scripting that describes the timing was performed in VHDL (Very-high-speed-integrated-circuit Hardware Description Language). The digital control system allows for rapid and accurate tuning of the gate signals to adjust for the resonant frequencies of different loads, and easy modification of RMP pulse length.

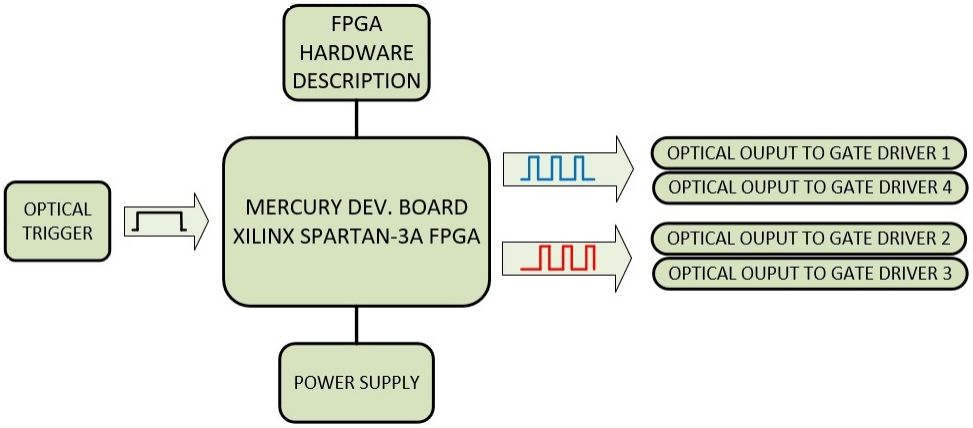

Figure 6.12: FPGA timing control

If the switches on one side of the H-bridge turn on simultaneously tens of thousands of amps can flow through the resulting short circuit. This would destroy the switches at a minimum, and

also represents a substantial safety risk. To avoid this, the out-of-phase square waves from the timing system have a dead time between their on times when all four IGBTs will be switched off. This time should be long enough to ensure full shut off, which due to the IGBT tail current can be substantial. However, a long dead time significantly distorts the desired sinusoidal waveform of the coil current. For the IGBT modules used in the system, the worst fall time observed was 2.5 μs. A minimum dead time of 5 μs is maintained for safety. This time is one of the contribution to the maximum switching frequency of the rotating RMP system.

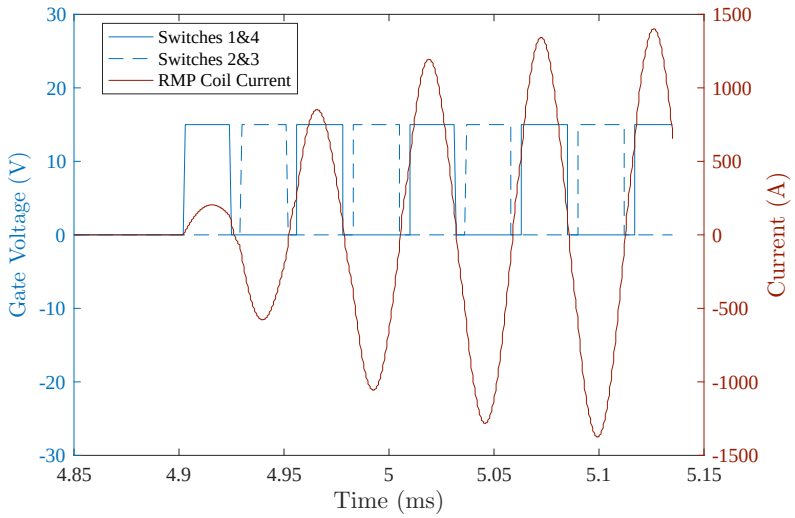

Figure 6.13: Gate timing with respect to coil current

6.3.5 Snubbing Circuit

When an IGBT is switched off large inductive spikes can appear across its collector and emitter. The voltages reached will depend on the inductance of the coils and the rate at which the device turns off. The inductance of the coils is set by their geometry and the turn-off times are required to achieve frequencies comparable to those of STOR-M's magnetic islands. Since these cannot be adjusted, other steps must be taken to mitigate potentially damaging overvoltages. The charging voltage could be kept low but this would limit driven current (and therefore the magnetic field strength of the RMP pulses) below the expected threshold to achieve mode-locking, namely, to bring the mode rotation frequency to the RMP rotation frequency. To overcome this problem, snubber circuits were implemented that act as shock absorbers for high transient voltages. This makes it possible to operate safely at higher switching speeds and currents.

For the layout in Figure 6.14, the capacitors across each IGBT collector and emitter are charged when that switch is conducting. The snubber diodes become forward biased when their respective switches are turned off and the inductive voltage spikes appear. This allows stored energy in the RMP coils to flow into the snubbing capacitors. Their capacitance must be sufficiently high in order to limit their voltage increase until the other set of switches is turned on and provide a new current path. At turn-on, when current is rising, the inductive voltage reduction allows the capacitors to discharge through the free-wheeling diodes, which are now forward biased, and the snubber resistors.

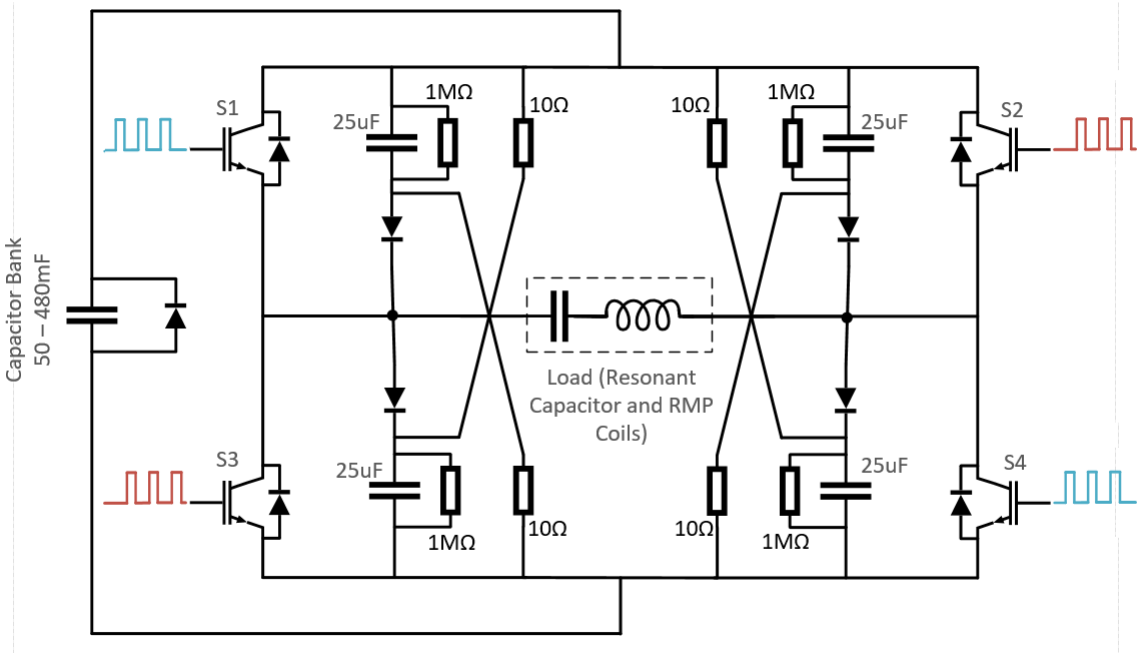

Figure 6.14: Snubbed H-bridge

Careful component selection is important. In addition to being capable of withstanding the power spikes, the resistors should be non-inductive to prevent ringing. The diodes need to have a short recovery time suitable for the frequencies being driven.

Figure 6.15 shows C-E voltage spikes of >150 V (<50 V) for an unsnubbed (snubbed) H-bridge circuit when the bank voltage is 40V and frequency is 12.2 kHz.

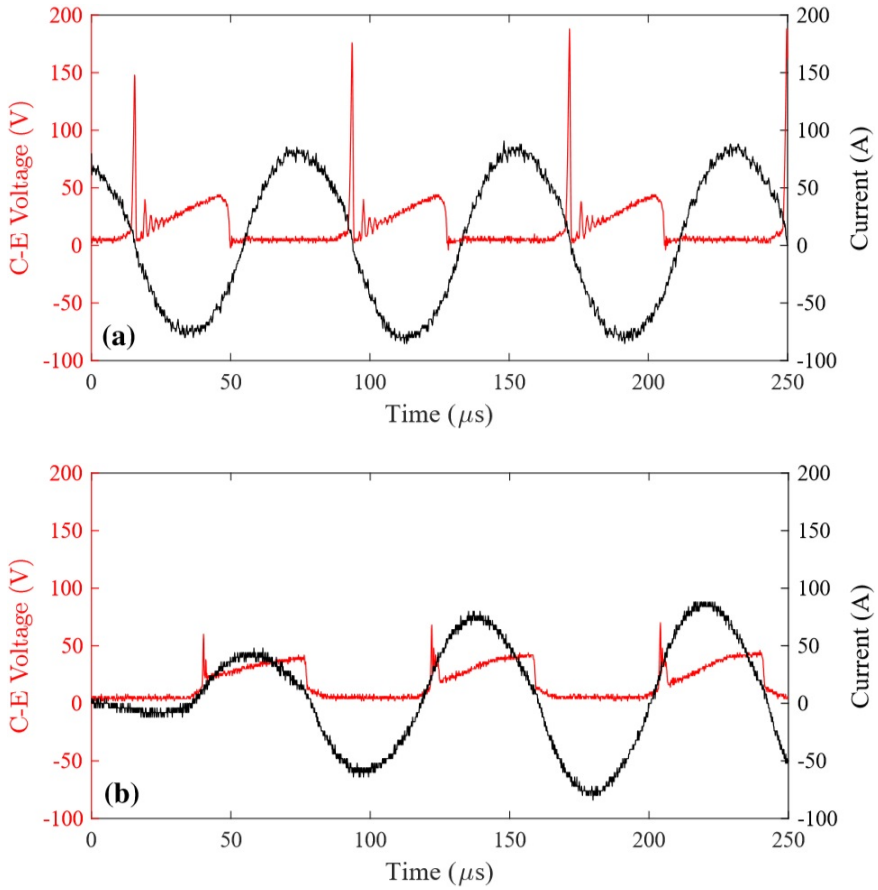

Figure 6.15: Effect of snubber circuit on collector-emmitter voltage during rapid switching. (a) Unsnubbed. (b) Snubbed

6.3.6 Wire Selection

A straight cylindrical conductor of length l, resistivity ρ, and cross-sectional area A has a DC resistance of

$$R_{DC} = \frac{\rho l}{A} \tag{6.34}$$

When driving alternating currents through the magnetic perturbation system's coils, a counter-electromotive force is established which is strongest at the center of the conductor. The changing currents, due to changes in the electric field, are accompanied by encircling magnetic fields that are also changing as described by Faraday's Law. The eddy currents resulting from the changing magnetic field reduce the total current flow towards the center of the conductor such that the majority of current flows in the outer layer of the conductor. This well-known skin effect is equivalent

to a reduction in the conductor cross-section and increases the total AC resistance,

$$R_{AC} = \frac{\rho l}{A_{eff}} \tag{6.35}$$

where A_{eff} is the effective cross-sectional area of the wire at a given frequency. The skin depth, δ, is the distance from the surface of an infinitely thick and long conductor at which the field strength will be reduced to $\frac{1}{e}$ of its strength at the surface.

$$\delta = \sqrt{\frac{\rho}{\pi f \mu}} \tag{6.36}$$

Here f represents the frequency of the oscillating field and μ its magnetic permeability. If the radius, r, of a conductor is large relative to the skin depth, its effective area can be approximated by its total area minus the area of the circle defined by the skin depth. That is,

$$A_{eff} = \pi r^2 - \pi(r-\delta)^2 = \pi(2r\delta - \delta^2) \tag{6.37}$$

It is common to ignore the δ^2 term as it has already been assumed δ is small relative to r however for common wire gauges dropping this term actually results in substantial errors ([75]).

Calculated using Maxwell's Equations, the exact resistance of a highly-conductive cylindrical wire is expressed using Bessel functions [76]. A simpler, faster model was used to calculate the values of R_{AC} in Figure 6.16 which are within 0.09% of the exact solutions [75]. For the frequencies shown, calculations using Equations 6.35 to 6.37 yield similar values for wire radii > 2mm. Ξ is used to represent the AC factor,

$$\Xi = \frac{R_{AC}}{R_{DC}} \tag{6.38}$$

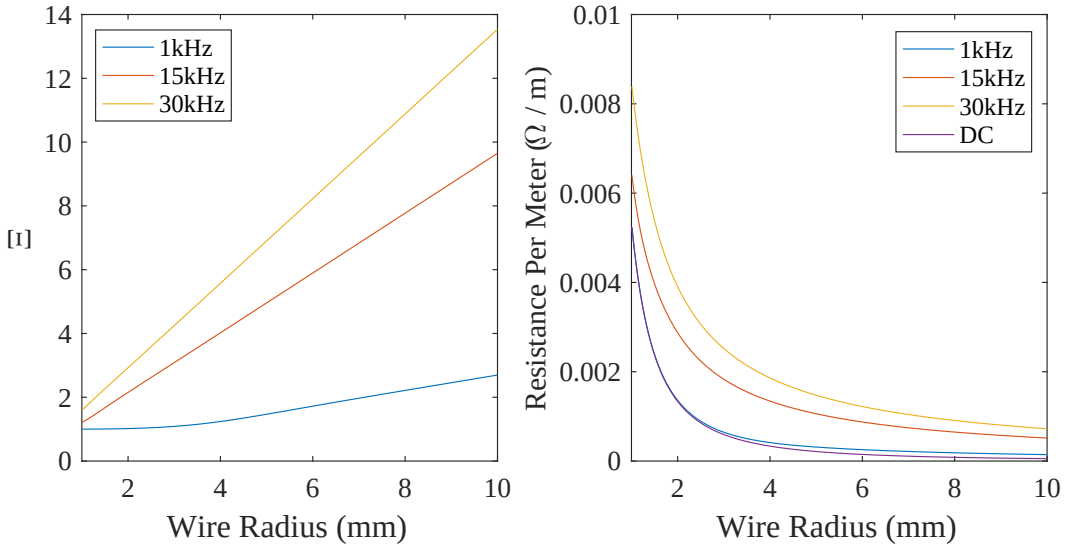

Figure 6.16: Left: AC factor, Ξ, and Right: the resulting resistance at relevant frequncies for different wire radii

Since the load resistance is the main determinant of the peak current driven through the coils it is important to minimize the resistance of all wires that make up the discharge path. The skin effect at the higher frequencies possible with the system renders much of the interior copper of a standard wire useless. One solution to this is to use litz wire. This is a type of stranded wire that reduces the skin effect by individually isolating strands to increase the effective surface area for a given cross-sectional area. This introduces a new challenge known as the proximity effect, which like the skin effect, causes AC resistance of a wire to increase with frequency. The cause of a current reduction in an insulated strand is again eddy currents, this time from the nearby strands. However, litz wire is wound in patterns that ensure each strand has similar lengths on the interior and exterior of the cable and equalizes the proximity effect across them, minimizing the effect overall. Litz wire (especially of the gauge required) is substantially more expensive than simple standard stranded wire and has a much larger total cross-section due to the additional insulation.

Another option to achieve a lower load resistance is to simply over-size the wires. With standard wire, a far larger diameter is required than necessary to avoid overheating concerns. While much of the interior copper is unused, for the small scale of the system the cost waste is not a significant issue. And, the smaller total wire diameter, as compared to litz wire, makes installing the coils a much easier task.

Flat (thin, cross-sectionally rectangular) wires could also be used. However, at the thicknesses needed to substantially reduce the skin effect these would have to be impractically wide. It would also be necessary to manually insulate the wires.

For simplicity of installation and minimizing the system's cost, the current setup uses mainly 8 gauge stranded wires. The RMP coils themselves are made of 14 gauge stranded wire as mentioned in Section 5.3. If the current, but not voltage rating, of IGBTs is improved in the future then replacing the standard wiring with litz wire would enable larger RMP currents.

6.3.7 Charging System

A simple transformer and bridge rectifier circuit (Figure 6.17) is used to charge the capacitor bank, which interlocks with the same signal that controls the bank charging of STOR-M.

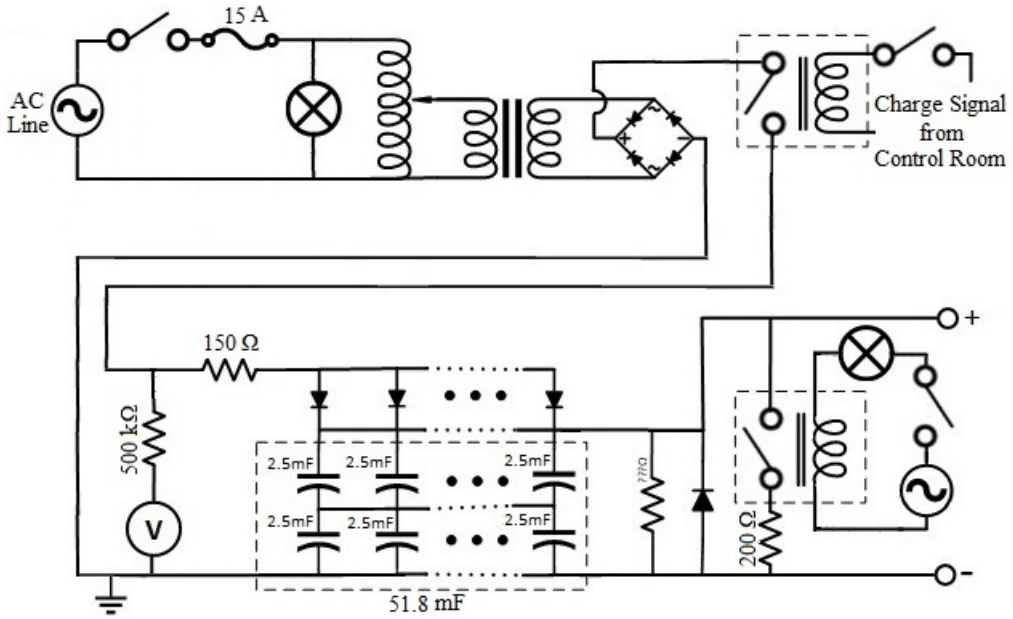

Figure 6.17: Capacitor Bank Charging System

The charger is capable of supplying up to 1000V but the practical limit on charging voltage is set by either the capacitor bank being used or wiring voltage rating (600 V), whichever is lower. It is sometimes preferable to swap the 900 V-rated bank to one with larger capacitance (420 mF) but lower voltage rating (200 V). The higher capacitance results in a flatter peak when driving direct current as the banks drain less quickly. Since the load resistance is not increased by the skin effect the charging voltage does not need to be as high. At present, charging voltages for experiments

rarely exceed 400V. Beyond this the large inductive voltage spikes due to rapid switching would tend to cause latchup in the IGBTs currently in use.

The perturbation system's banks are not fully drained in one pulse, and under standard charging times for STOR-M's main banks, the bank voltage increases towards the charging voltage each shot until a stable voltage is reached after 4 to 5 shots.

6.4 Images of Completed Magnetic Perturbation System

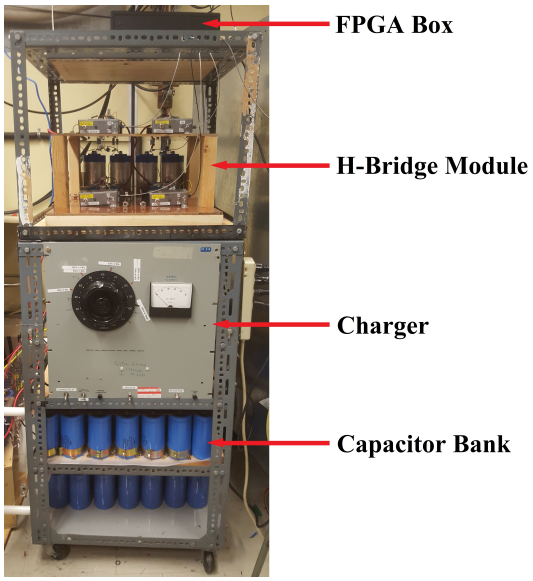

Figure 6.18: RMP power supply

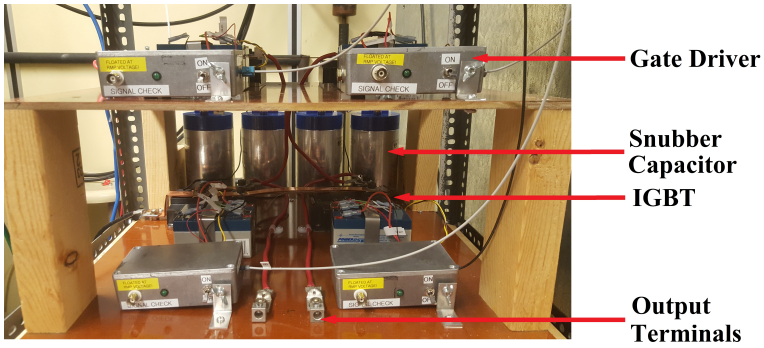

Figure 6.19: H-Bridge Module

CHAPTER 7

DIAGNOSTICS

A large number of diagnostics tools are available on STOR-M that enable the examination of plasma current, line-averaged density, temperature, position, toroidal flow velocity, and the detection of magnetic fluctuations. During RMP application, clear changes are seen in the signals collected from many of these diagnostics. At this point it is unclear whether most of the interesting changes observed in these diagnostic signals are due to the RMP's effect on the plasma. The RMP creates a large amount of electromagnetic interference which must be accounted for during signal analysis. Additionally, the automatic plasma position sensing and control system may miscalculate due to this noise and attempt a correction, pushing the plasma column inwards or outwards and effectively sweeping the non-homogeneous plasma past, for example, soft x-ray camera lines-of-sight. In the previous static RMP experiments on STOR-M electromagnetic interference did not impose a significant difficulties since the position sensing and fluctuation detecting signals are sensitive to only changing signals.

7.1 External Magnetic Field Coils

One of the diagnostic systems available is a set of Mirnov coils, composed of many simple magnetic pick-up coils. Their planes are oriented parallel to the vacuum chamber at their locations so that they encircle and are perpendicular to the radial magnetic field lines. Assuming a uniform magnetic field perpendicular to the coil plane, B, each coil end produces a voltage output, V, proportional to the area bounded by the coils, A, their number of turns,n, and the rate at which the magnetic field changes as follows from Faraday's Law.

That is,

$$V = \frac{\partial \mathbf{B}}{\partial t} nA \tag{7.1}$$

The main indicators used to detect the presence of rotating magnetic islands within the STOR-M plasma are these discrete Mirnov coil signals, which measure the poloidal field component at a distance of 16 cm from the plasma centre, on the exterior of the vacuum chamber. It is important to note that distortion of the magnetic surfaces due to the radial field comes with a change in the poloidal field at the same time. Therefore, the rotating magnetic islands will cause both radial and poloidal magnetic fluctuations.

Each set of Mirnov coils consists of 16 discrete coils evenly distributed along the poloidal direction with an angular separation of 22.5 deg [77]. Examination of the full set of coils enables mode calculations of the plasma magnetic islands. Using just one channel, time-frequency analysis can reveal the rotational frequencies of the magnetic islands. For speed and simplicity this is the method that is utilized in the following chapter to indicate the current status of the new RMP system's impact on the plasma.

After performing a time-frequency analysis on a magnetic signal it is ordinarily clear what part of the signal is from the plasma, and what is due to the RMP noise. However, for high-frequency RMPs in the range of the magnetic island rotational frequencies it not as easy to distinguish between the two. In these cases, vacuum RMP shot data is collected, and after matching the starting time of both applied perturbation signals, subtracted from a plasma shot with the same RMP coil current. RMP discharges are highly reproducible and this effectively removes the majority of the RMP noise. Due to small (microseconds) deviations in the relative data-collection starting times and the beginning of an RMP pulse from shot to shot these timeshifts are performed manually.

7.2 Internal Radial Magnetic Field Probes

Another magnetic diagnostic tool available on STOR-M is an internal radial magnetic field probe array, depicted in Figure 7.1. The array has four individual coils of 60 turns each and all have a resistance and inductance of approximately 1 Ω and 5.5 μH respectively. They are located on the end of an extendible manipulator and connected to the vacuum chamber through bellows.

The probe array cannot be inserted into the plasma core without damaging its ceramic sheath and causing disruptions of the STOR-M discharge but it can be used to probe the edge plasma. These internal probes were used to test the magnetic field attenuation due to the vacuum chamber. The raw signals are integrated digitally.

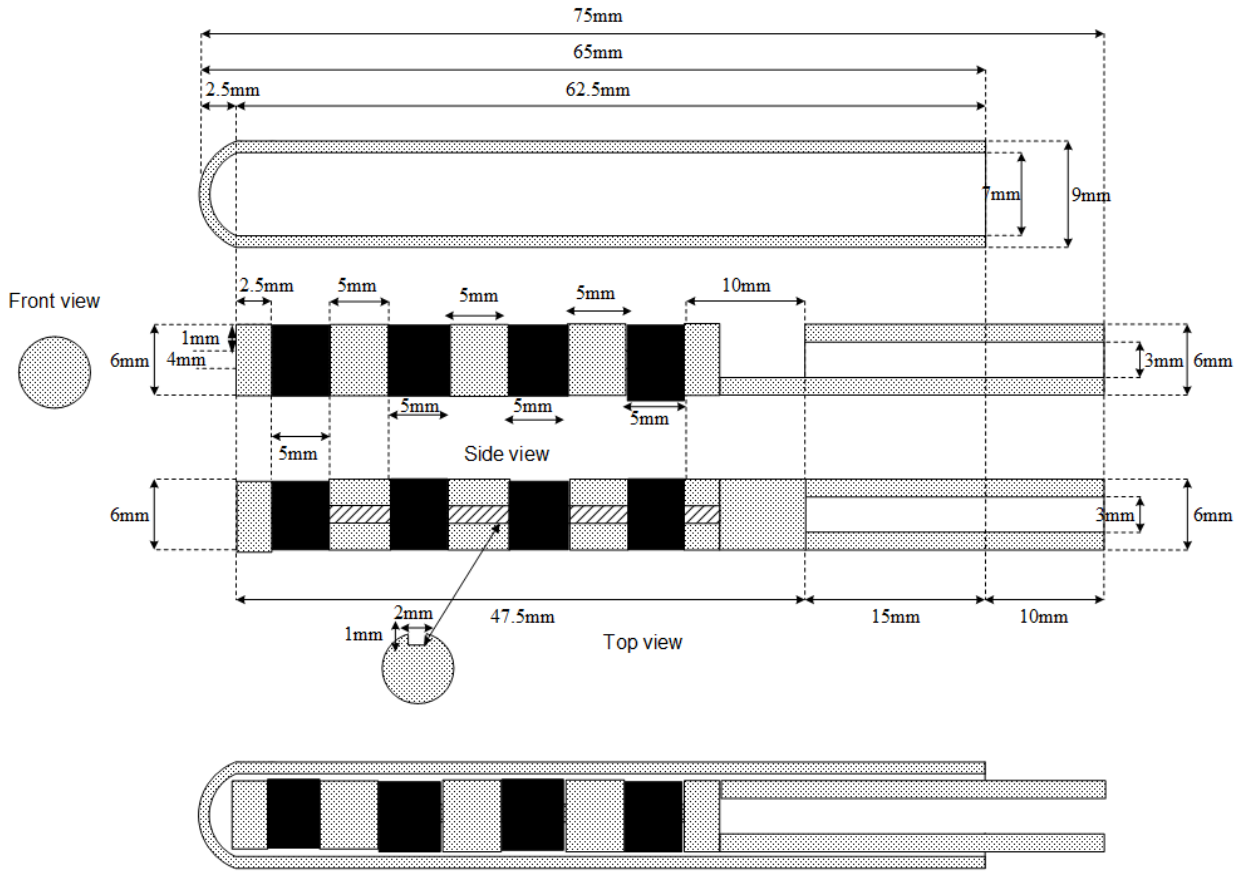

Figure 7.1: Internal radial magnetic field probe (from [78])

7.3 Wavelet Analysis

A modified version of the Short Time Fourier Transform (STFT) is used to examine how signal frequencies evolve over time. In the STFT, a signal is divided into segments by means of a sliding window function, w and the Fourier transform is performed on each segment individually:

$$X(\tau,\omega) = \int_{-\infty}^{\infty} x(t)w(t-\tau)e^{-i\omega t}dt \tag{7.2}$$

where $\omega = 2\pi f$ and τ represents the time step.

A spectrogram of the signal is then simply the STFT's magnitude:

$$|X(\tau,\omega)|^2 \tag{7.3}$$

The choice of a window's length has a strong impact on the spectrogram. A short window will produce good time resolution and poor frequency resolution, and a long window the reverse. For a given number of samples, N, obtained at a sampling rate of f_s, the Fourier Transform will produce $\frac{N}{2}$ unique coefficients corresponding to frequencies from zero to the Nyquist frequency, $\frac{f_s}{2}$. To improve frequency resolution, the spacing between these frequencies, $\frac{f_s}{N}$, must be reduced. If f_s is lowered (but N kept constant), there will be fewer samples per unit time and the window size will increase accordingly. When f_s is held constant, increasing N also results in a longer time window and so any attempt to improve frequency resolution comes at the cost of decreasing time resolution.

Likewise, improving the time resolution (by decreasing the window size) results in an increase in the spacing of frequencies, and a reduction in frequency resolution.

The most appropriate window length is selected based on the frequencies present in a signal and how quickly those frequencies change. If the timescale or frequency range of a signal vary significantly, a pre-determined window length will be inadequate.

The wavelet transform uses a range of window lengths to capture both high and low frequency information with the optimal time-resolution. It is defined as,

$$S(\tau,a) = \frac{1}{\sqrt{a}} \int_{-\infty}^{\infty} \psi^* \Big(\frac{t-\tau}{a} \Big) x(t) dt \tag{7.4}$$

where ψ is the wavelet function, which takes the place of the window function in STFT, and ψ^* is its complex conjugate. And as with the STFT, τ represents the time shift. a is adjusted to scale the wavelet and adjust the window length and the transforms are computed for each scale, then combined.

Ψ, the Fourier transform of ψ, must satisfy the two conditions,

$$\int_{-\infty}^{\infty} |\psi(t)|^2 dt < \infty \tag{7.5}$$

$$\int_{-\infty}^{\infty} \frac{|\Psi(\omega)|^2}{\omega} d\omega < \infty \tag{7.6}$$

which imply ψ has finite energy and is admissible. That is, the Fourier transform of the wavelet is zero at the origin, which is required for the wavelet transform to remain bounded, and for the signal to be reconstructable.

The wavelet function which minimizes the joint time-frequency uncertainty, and which is used in the analysis of magnetic diagnostic signals in Chapter 8 , is the Morlet wavelet, which is a simple sine wave enveloped by a Gaussian function,

$$\Psi_{Morlet}(t) = e^{i\omega_0 t} e^{-\frac{t^2}{2\sigma^2}} \tag{7.7}$$

In the wavelet transform, a represents a dilation of the entire wavelet, whereas σ is a dilation of only the Gaussian envelop, and is known as the variance (or bandwidth) parameter.

CHAPTER 8

EXPERIMENTAL RESULTS

Numerous tests have demonstrated the wide operating parameters available with the newly constructed magnetic perturbation system. A typical STOR-M discharge lasts 30 to 40 ms, following a 3.5 min idle and charge cycle. The pre-programmed RMP current waveforms, sinusoidal or rectangular, are turned on during the tokamak discharge for a few milliseconds. It is possible to exceed the current rating of the IGBTs in the RMP circuit (600 or 1200 A) due to the short pulse time and long duty-cycle. Currents from 1 to 2200 A have been fed through the coils. This risks latchup and device destruction however hundreds of pulses at double the device rating have been performed without issue. RMP discharges can be single-directional or made to oscillate up to a maximum frequency of approximately 25 kHz, determined by the turn-off time of the IGBTs. Figure 8.1 shows three examples of current waveforms driven in the helical coil by the magnetic perturbation system's power supply. It can be seen that there is a transient period before the sinusoidal signals settle to a relatively stable amplitude. This transient time ranges from a fraction of a millisecond at high frequency to a few milliseconds at low frequency. The peak amplitude reached appears approximately stable on the timescale of a discharge due to the large bank capacitance.

The amplitude of inductive voltage spikes across IGBT collectors and emitters increases with the current between them and with switching speed. The device rating for this voltage (1200 V) is the determinant of maximum current/frequency, and exceeding the rated collector-emitter voltage caused a number of system failures (damaged IGBTs) during the development phase. The higher the current pulsed through the coils, the lower the maximum frequency, and the higher the frequency, the lower the maximum current. Closely matching the driving frequency from the FPGA control system with the resonant frequency of the load (coils and resonant capacitor) is helpful in limiting the inductive voltage spikes. With close frequency-matching, at the maximum frequency of 25 kHz, it was possible to repeatedly drive 1500 A of current without exceeding the

1200 V rating across the collector-emitter. This was done using the smaller, 600 A rated PRX (model CM600HA-24A) IGBTs due to their shorter turn-off time compared to the 1200 A IGBTs.

The larger Infineon modules (model FZ1200R12HP4), rated for 1200 A and 1200 V, are used when higher currents/lower frequencies are required. The highest current safely passed with these modules, 2200 A, was driven at 2.6 kHz. When applying a static RMP, the size of the IGBT gate resistors can be increased to extend the turn-on/off times, reduce inductive voltages spikes, and increase the maximum safe current. A DC discharge will cause the supply capacitor bank to be drained more quickly however, and additional capacitance should be added to the bank for pulses longer than several microseconds.

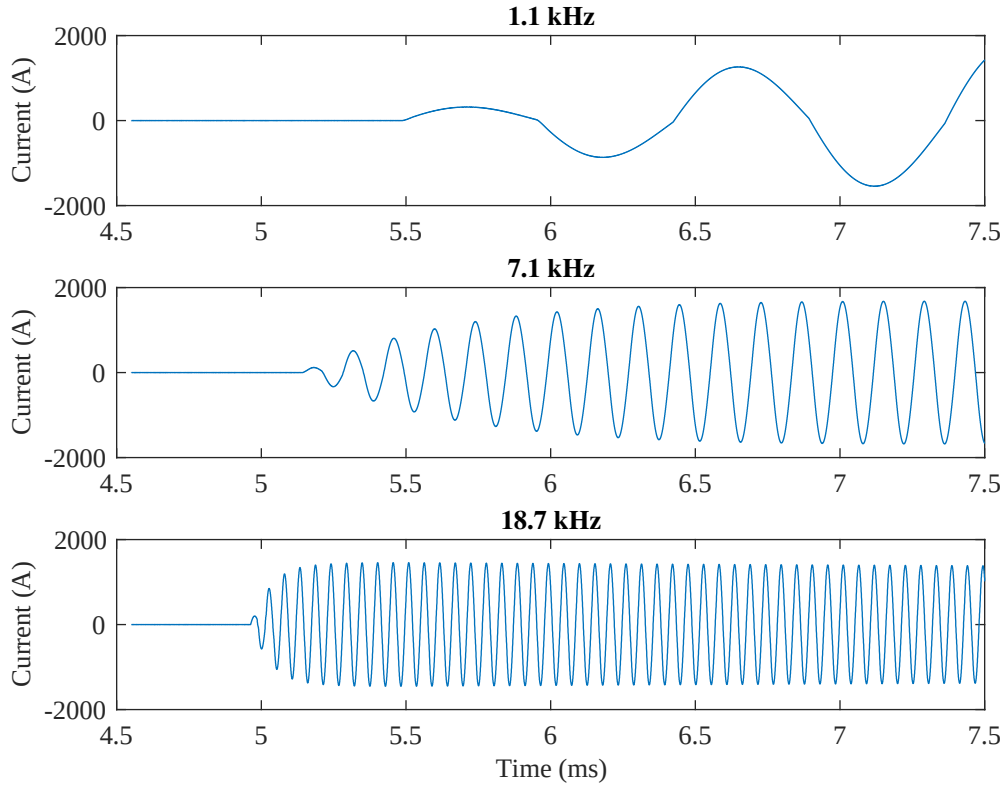

Figure 8.1: RMP coil currents for three example frequencies

8.1 System Tests With Helical Coil

The helical coil has previously been seen to strongly affect magnetic island rotational frequency [13]. The first test of the new magnetic perturbation system was to confirm this result and demonstrate the plasma conditions were appropriate for further RMP experiments.

For reference, Figure 8.2 shows a wavelet analysis of a single channel of the Mirnov coils described in Section 7.1 during a typical STOR-M discharge (having basic plasma discharge parameters similar to those shown in Figure 2.6) during the flat current region. These coils are oriented to detect the radial magnetic field of the rotating islands but not the toroidal field of the main magnets or poloidal field of the plasma current. A wavelet analysis on the induced voltage signal in a coil allows determination of the rotational frequencies of the islands present in the plasma.

In the top plot, the time variation of magnetic island rotational frequencies present in the plasma is displayed. The bottom plot shows the time-evolution of the weighted average of these frequencies as defined by the following equation:

$$f_{w_{avg}} = \frac{\sum_f I(t,f) f}{\sum_f I(t,f)} \tag{8.1}$$

where here I represents the intensity of the individual frequencies. This weighted average remains relatively stable throughout the current flat-top, between 30 to 40 kHz.

The wavelet analyses shown in this chapter were all done in the "flat-top" region of plasma current, after the initial current ramp-up and plasma breakdown and before termination of the plasma. The plasma discharge begins at $t = 0$. The magnetic pick-up coil used to obtain the analysed signals is located at $\theta = 0$, on the low field (ouboard) side of the torus.

References to RMP current are to the peak current reached. Over the course of a discharge the amplitude of an RMP pulse decreases somewhat as the supply bank is drained due to the resistive component of the load.

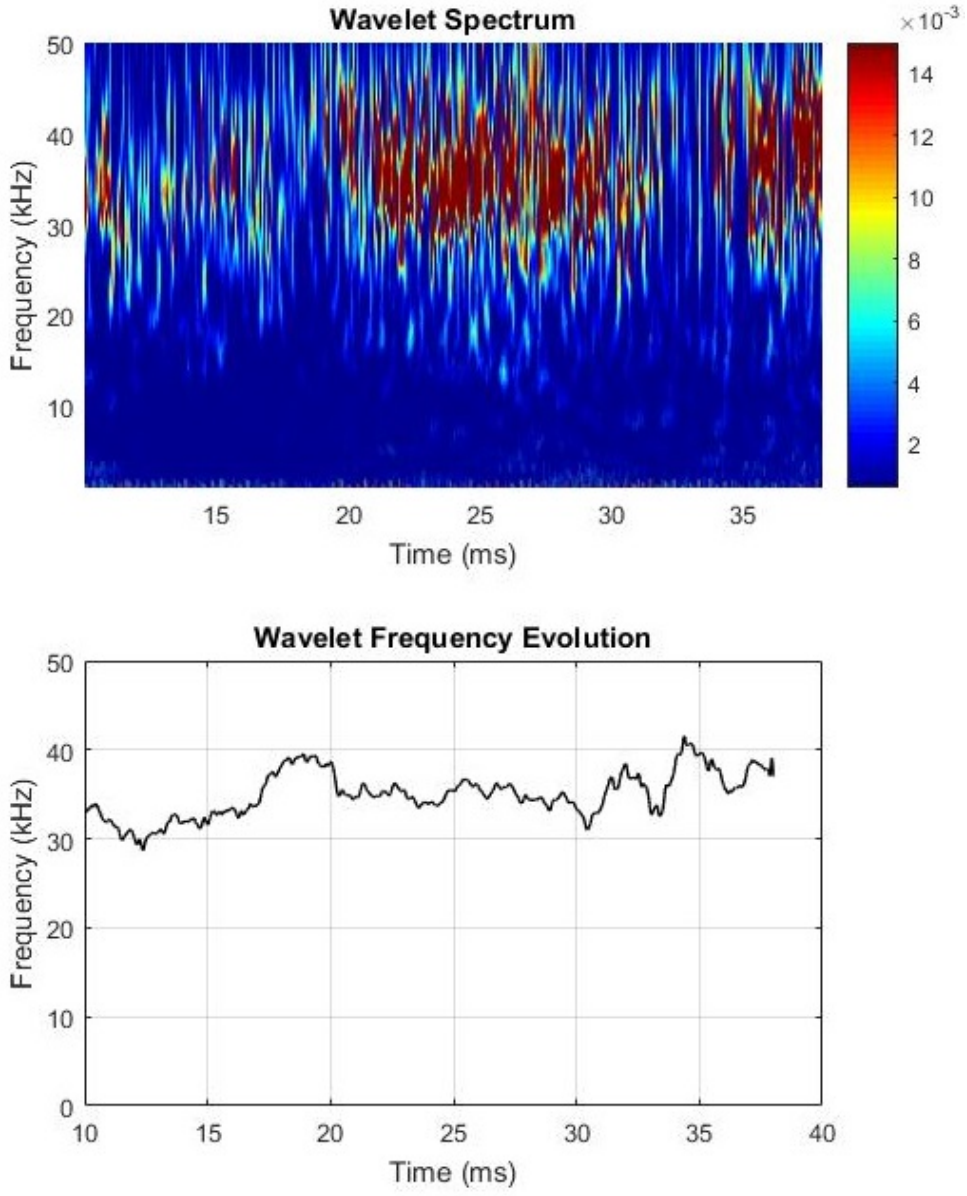

Figure 8.2: Magnetic island rotational frequencies present in a typical STOR-M discharge

8.1.1 Alternating Static Pulses

The application of a series of 3 ms current pulses with alternating polarities is demonstrated in Figure 8.3. On the timescale of the magnetic island rotational frequencies, these discharges can be considered to be constant in time,i.e. static, stationary pulses. The current driven in the helical coil is overlaid on the wavelet analysis plots. Contrasting with Figure 8.2, a clear reduction of island

rotational frequencies is seen to coincide with the RMP signal, regardless of current direction, and consistent with the earlier results on STOR-M. The independence of the current direction is expected for two reasons. Firstly, the helical RMP coil is wound once in one toroidal direction and once in the other so that for any polarity current is driven in both directions. And secondly, a tearing mode's rotation will bring its associated magnetic field in and out of phase with the perturbation field of the helical coil whatever current direction is chosen.

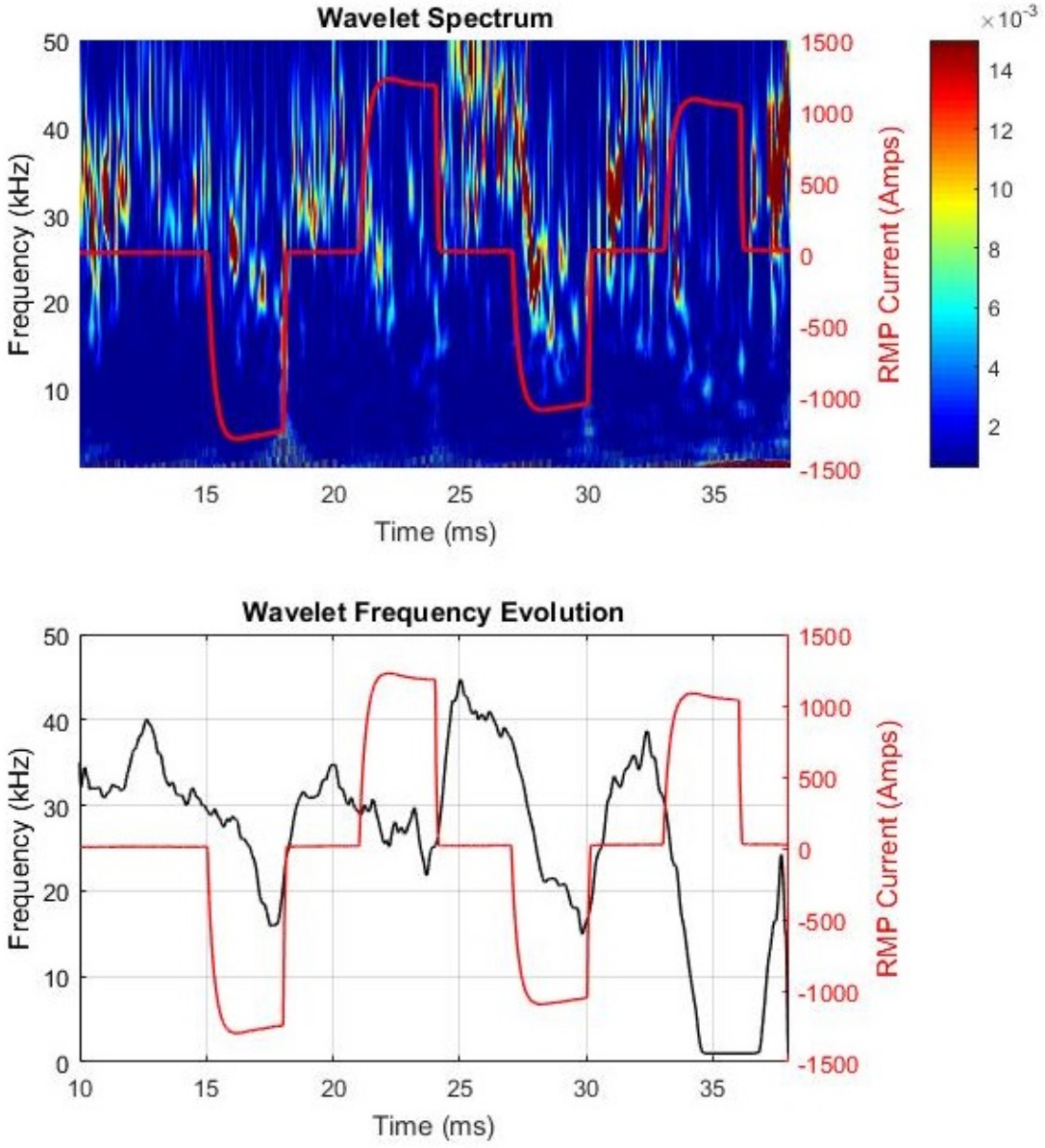

Figure 8.3: Effect of static RMPs produced by helical m/n = 2/1 coil on magnetic signal

8.1.2 Oscillating Current

The highest achievable currents for the different available frequencies were tested using the helical coil. Note that it is not possible to make a perturbation rotate around the chamber using this coil. By driving an oscillating current in the single coil a standing wave is established in the chamber. The effects of an RMP discharge on the plasma are independent of the direction of RMP current when the applied perturbation is static. A low frequency standing wave should have a similar effect to a static perturbation as it is close to being static in the reference frame of quickly rotating magnetic islands. For a given RMP current, the effect would be expected to be less than the static case however, due to eddy currents in the vacuum chamber and because the field strength's average magnitude is lower.

Applying a low frequency RMP pulse early in the flat-top, such as in Figure 8.4**(a)**, where the magnetic perturbation oscillates at 2.6 kHz, has no clear effect on the rotational frequency of magnetic islands. This holds for low currents (hundreds of amps) up to the maximum investigated with this set-up: 1200 A. It may appear in **(a)** that the RMP pulse induces island growth (represented by the onset of larger amplitude oscillations) as the start of the RMP and the increased island field amplitude coincide. However, this is the time at which island widths naturally grew during a discharge on the day of these experiments. There is no discernible difference between plasma discharges without RMPs and those in which RMP is applied before islands begin to grow.

When the RMP is applied later in the discharge, after island growth has already begun (8.4**(b)**), it was repeatedly seen to result in a decrease in island frequency and amplitude. The threshold current for this effect appears to be in the 900 to 1000 amp range.

Sufficiently high current (> 800 A) RMP pulses that begin during the last approximately 5 ms of the flat-top result in a disruption and early termination of the plasma.

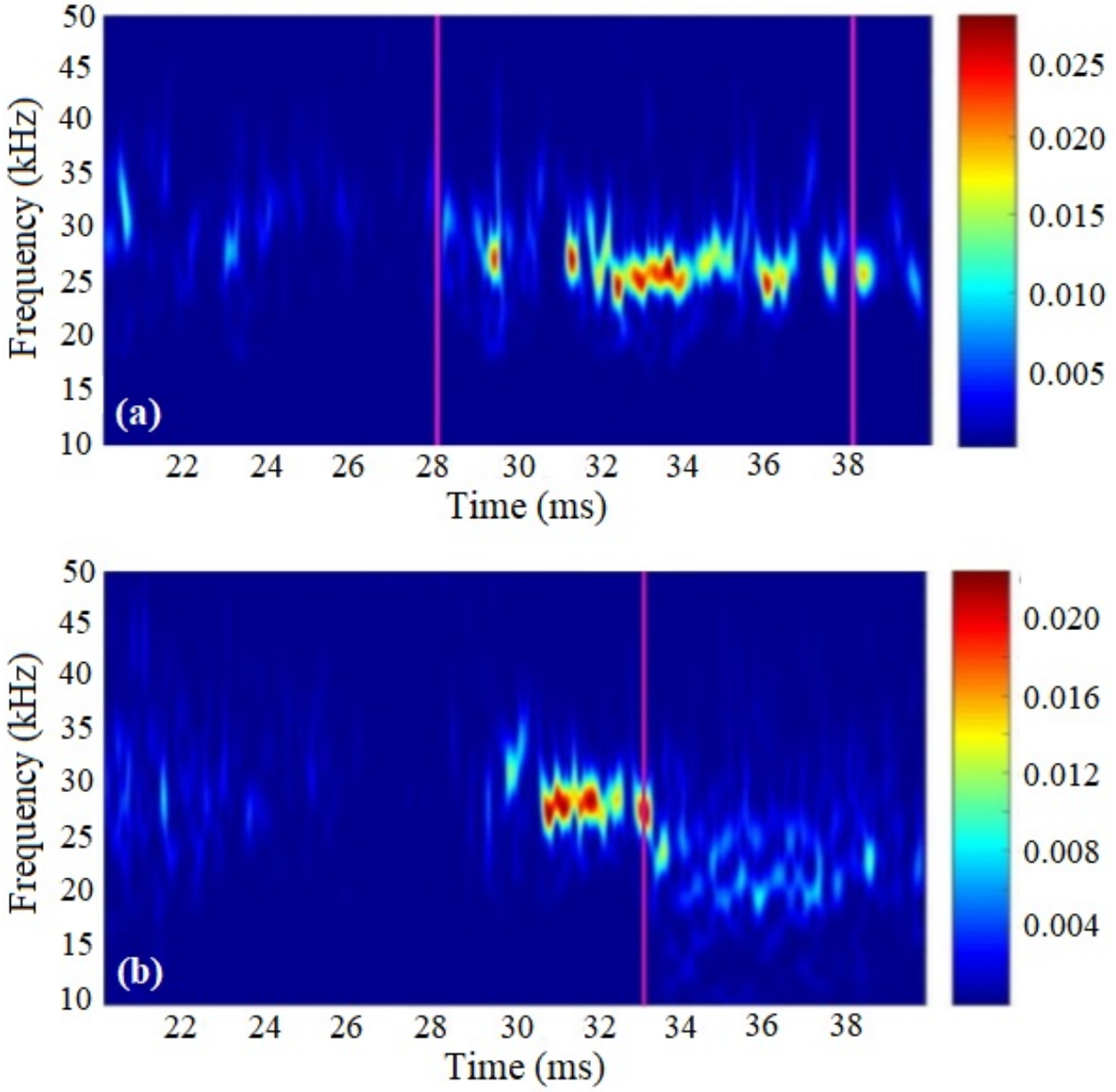

Figure 8.4: Wavelet Spectrums with 2.6 kHz RMP (1150 A) for two shots: (a) RMP applied from 28.2 ms to 38.2 ms and (b) RMP applied from 33.2 ms to 43.2 ms. Purple bars indicate RMP pulse window

Similar results were obtained for mid-range frequency tests, such as at 10.7 kHz. In Figure 8.5, the 10 ms long artifacts of well defined, constant frequency are due to pickup of the field induced by the RMP current. They do not represent a magnetic island in the plasma. In the case of RMP application in the later half of the flat-top, a small frequency decrease is again observed, however the drop always occurs more gradually than the sudden frequency reduction associated

with low-frequency or static RMPs. At this mid-range frequency, changes to signal amplitude were inconsistent. Again, beginning an RMP pulse in the final stages of the flat-top caused plasma termination.

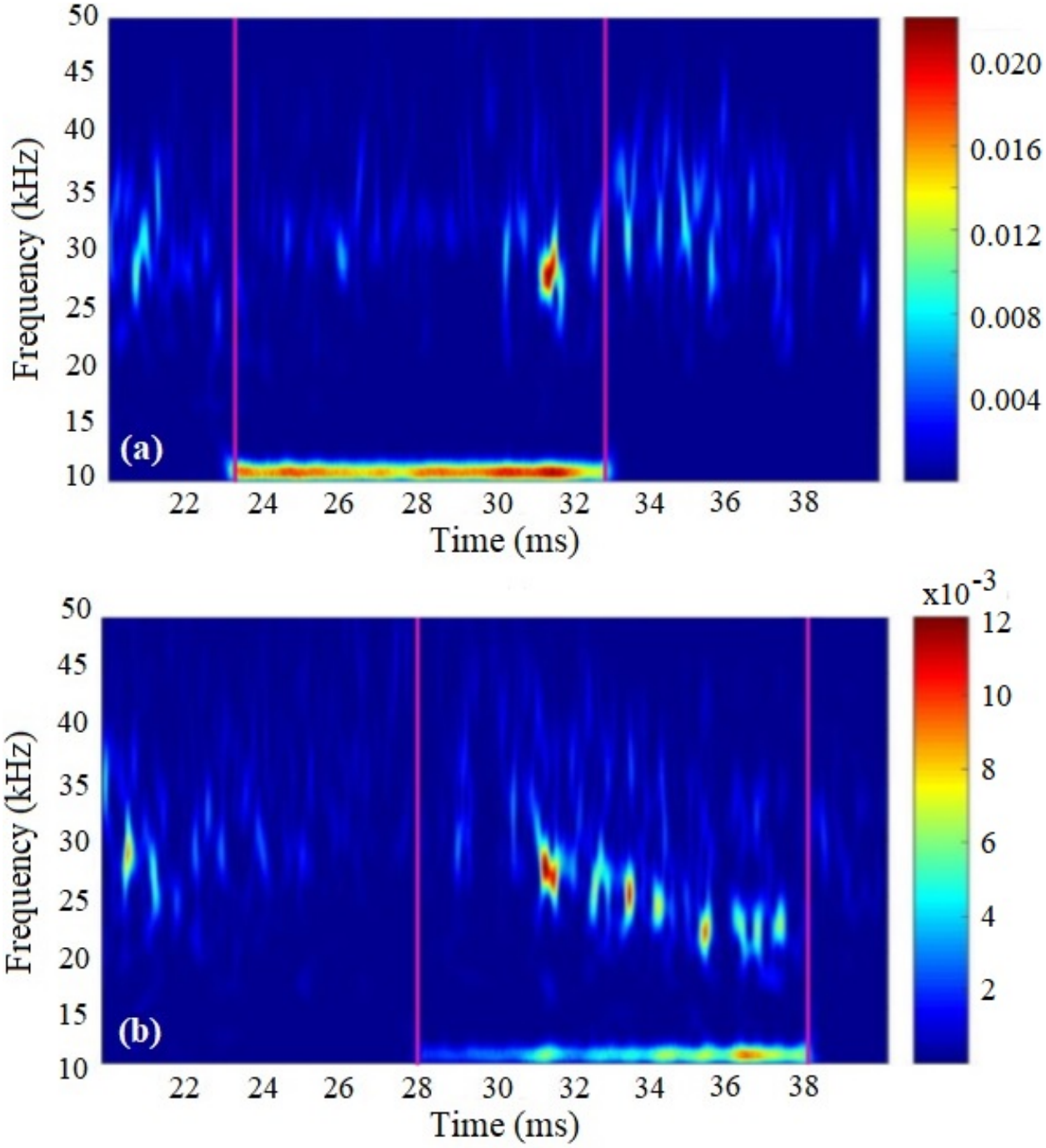

Figure 8.5: Wavelet Spectrums with 10.7 kHz RMP (1100 A) for (a) RMP applied from 23.1 ms to 33.1 ms and (b) RMP applied from 28.0 ms to 38.0 ms

At higher frequencies (15 to 25 kHz), magnetic measurements have not shown any indication of a standing wave RMP having an effect on the plasma.

8.2 System Tests With Discrete Coil Arrays

For four coil arrays, two H-bridges are needed to achieve a rotating perturbation. By reversing the polarity of connections, a single bridge can feed coils that must be 180 degrees out-of-phase. For the current discrete coil set-up, adjacent arrays are separated by 90 degrees and must be fed with currents that are 90 degrees out-of-phase, and therefore cannot be fed via the same bridge. The charging system, control system, capacitor bank, and H-bridge of the new magnetic perturbation system are all modular, and stacked vertically in a rack. Adding the additional H-bridge module needed for rotating perturbations will be a simple task. Before committing the required resources to do so, static and standing wave perturbations were also investigated using the discrete coil arrays.

It was expected their use would have a similar impact on the plasma as the helical coil. However, this was not the case. Static current pulses of up to 2200 A were fed through the discrete coils with no discernible effect. This was likewise the case for any of the possible standing wave frequencies.

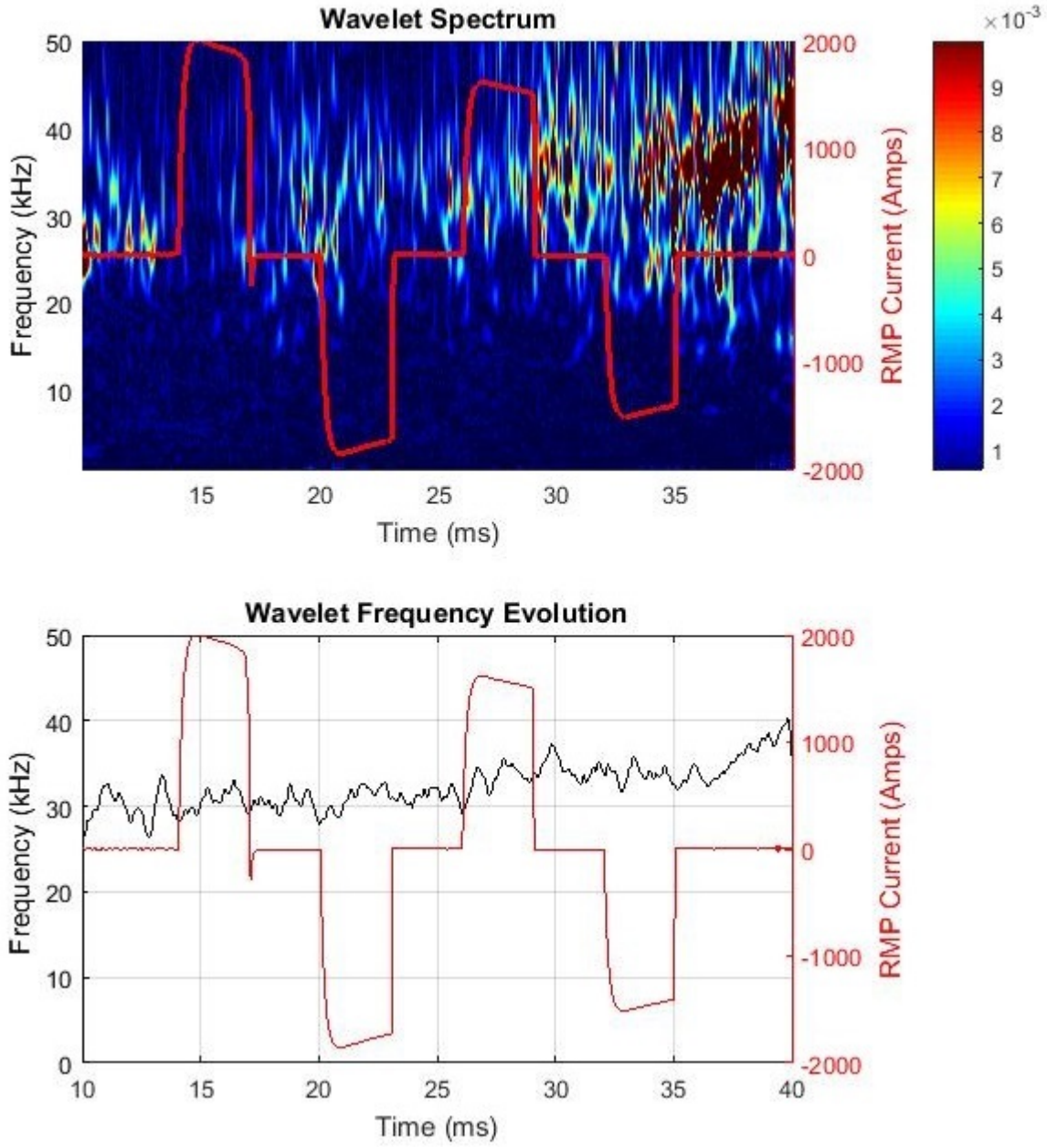

Figure 8.6: Effect of static RMPs produced by discrete m/n = 2/1 coils on magnetic signal

8.3 RMP Chamber Penetration

The attenuation due to eddy currents in the chamber walls was expected to be significant at high frequencies.

Maxwell's equations applied to a plane wave impinging on a large, flat material with high

conductivity $\sigma >> \varepsilon f$, where ε is its magnetic permeability and f the frequency of the wave, lead to an attenuated plane wave solution. That is,

$$B_{conductor} = B_0 e^{i(2\pi f t - \frac{x}{\delta})} e^{\frac{x}{\delta}} \tag{8.2}$$

where x represents the distance from the conductor surface and $\delta = (2\pi\mu\sigma f)^{\frac{-1}{2}}$, with $\mu \approx \mu_0$, the permittivity of free space. The attenuation constant δ is known as the conductor's skin depth.

While clearly inaccurate, this simple model of a plane-wave impinging on a zero-curvature conducting wall was used to estimate the approximate amount of attenuation expected as the magnetic field created by the perturbation system passes through the vacuum chamber walls. The model is shown in black in Figure 8.7(a).

The other series in Figure 8.7(a) show the actual attenuation due to chamber eddy currents as measured by probes at four radial locations. All measurements were taken with very similar RMP coil currents. The raw signals' strengths at various peaks from different shots were recorded and scaled to the corresponding coil current peaks. For each frequency, the average of twenty-five measurements (five peak for each of five different shots) was taken. The data from each probe was then fitted to an exponential and normalized so that 0 kHz corresponds to a field/signal strength of 1. Standard deviation is used as in indication of error.

Figure 8.7(b) displays the time delay between a peak in the coil current and the corresponding magnetic field peak as measured by the probes. As with the signal strength, delay times were measured at five points for five different shots each. And again, the plotted values are averages and the error bars represent standard deviations.

The observed attenuation is significantly stronger than the plane conductor and plane-wave approximation. Neglecting the vacuum chamber, a peak magnetic field of 27.4 G (calculated using the same scripts as in Section 5.2) would be produced at the r = 7 cm surface per 1 kA of current in the discrete coils. At 10 kHz, the approximation gives a reduction to 32% of the magnetic field's original amplitude so that a peak field of 8.8 G per 1 kA coil current would be generated at r = 7 cm. Despite the significant attenuation, this is stronger by far (at 1 kA coil current) than the field required to see an effect in the J-TEXT experiments (2.2 to 3.5 G) [47]. And, by driving 1800 A a comparable field would be created with that seen to affect the plasma in earlier experiments on STOR-M utilizing static RMP from the helical coil.

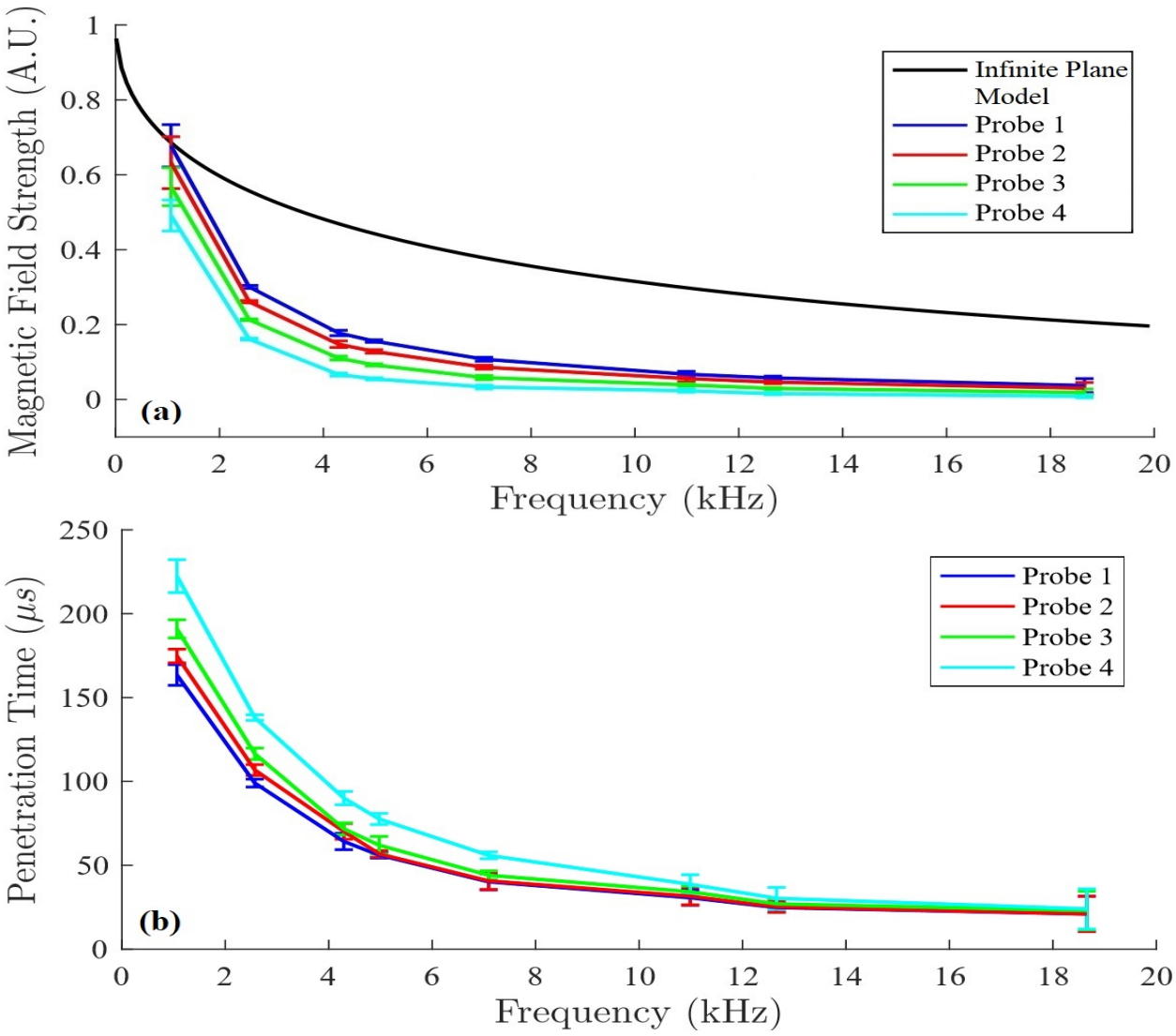

Figure 8.7: Penetration of magnetic field into vacuum chamber, measured at four radial locations. Probe 1: r = 11.9 cm, Probe 2: r = 12.9 cm, Probe 3: r = 13.9 cm, Probe 4: r = 14.9 cm. (a) attenuation, with field strength at 0 kHz scaled to 1. (b) time delay between current peaks and corresponding probe signal peaks

The measured attenuation is position-dependant. The probes are inserted towards r = 0 from the exterior of the chamber at $\theta = 0$ and experience stronger attenuation the closer they are to the chamber wall. Though the probes have slightly different calibration factors due to small differences in their resistances and their exact winding geometry, their frequency responses are in the MHz

range and differences in these values cannot be responsible for the different attenuations. The discrepancy is possibly due to the non-uniform distribution of other conductors around the vacuum vessel.

At the locations measurements were performed, a magnetic perturbation driven at 10 kHz is reduced to approximately 3 to 8% of its unattenuated amplitude, with the probe location closest to the m/n = 2/1 surface (at r = 7 cm) experiencing the weakest attenuation. It is expected then that at this surface a field of at least 2.2 G per 1 kA will be generated. Even at this level of attenuation, the perturbation system can create fields similar to those used on J-TEXT. However, at this frequency it is not possible with the current system to produce a field of the same strength required in the earlier static RMP experiments on STOR-M. At 10 kHz, the coil current would need to be approximately 7500 A.

Unless the system can be upgraded, attenuation through the vacuum vessel will likely impose an upper frequency limit on future experiments. Beyond approximately 4 kHz, the magnetic field strength inside the chamber will be lower than the previously established minimum, even at the maximum possible coil current. However, on other tokamaks it has been seen that the closer the frequency matching between the externally applied perturbation and magnetic island rotational frequencies, the lower field amplitude is required to achieve mode locking to the perturbation. Effects on the plasma may be seen at higher frequencies and lower field strengths than otherwise expected.

CHAPTER 9

CONCLUSION, SUMMARY, AND FUTURE WORK

9.1 Conclusion

IGBTs are the optimal choice when requiring both a high-current and high-frequency semiconductor switch, such as for the H-bridge power supply discussed in this thesis. In such a circuit, close frequency matching of the driving signal with the resonant frequency of the load is necessary to maximize driven current. It is also important to precisely control the dead time between on-states of the switch pairs to balance the maximization of current, the enabling of high-frequency oscillations, and maintaining a sinusoidal waveform with the need to avoid a catastrophic short circuit. This requirement is best met by a digital control system, such as the FPGA controller implemented here.

A high frequency limit is imposed by the turn-on and turn-off times of the switches used, but also by the dangerous voltage surges induced by rapid switching. If the latter are what restricts the possible high frequencies for a high-current power supply, snubbers can be used to extend this limit further. Published device current ratings are typically given in regards to steady state, or specific pulse-times. When the power supply will have both a low duty-cycle and the length of one pulse is very short, many of these ratings can be exceeded, including those of semiconductor switches like IGBTs. Pushing components beyond their rated limits (current, voltage, frequency or otherwise) always risks their failure. It is important to develop gate drive circuits for the main switches that fail in the off-mode to avoid destruction of the more expensive components.

Using more discrete elements will enable a closer match when attempting to imitate a continuous system. In the case of trying to create a magnetic field of a specific helicity such as in this thesis, the maximum possible number of coils should be used to obtain a purer mode. This will

naturally come with physical space limitations. And, in the case of a rotating perturbation, will require additional H-bridge modules.

9.2 Summary

The deleterious effect on plasma confinement from the various MHD instabilities continues to be an issue in the development of a commercial magnetic confinement fusion reactor. Recent experimental studies using resonant magnetic perturbations have focused primarily on ELM suppression and mitigation. STOR-M does not operate in H-mode, where ELMs are present. However, the large-scale tokamak ITER, along with its successors, will have more slowly rotating magnetic islands than the previous generations of devices. The problems associated with these slower rotations (the locking of magnetic islands to external error fields and the subsequent island growth, leading to plasma disruptions) are likely to bring renewed interest in tearing-mode instabilities, which are present in all tokamaks. The newly constructed, versatile magnetic perturbation system on STOR-M will enable the Plasma Physics Lab to build upon past investigations into resonant magnetic perturbations and pursue further research into understanding their effects on tearing-mode instabilities.

By pushing high-power IGBTs to their operational limits the magnetic perturbation system can drive 2200 A of direct current, or at the maximum frequency of 25 kHz, up to 1500 A alternating current. A clear modulation of magnetic island rotational frequency has been observed when driving a direct current through the helical, m/n = 2/1 coil on STOR-M.

9.3 Future Work

On future large devices that have slowly rotating islands it would be desirable to lock these islands to externally applied rotating magnetic perturbations and spin them up to a faster rotational speed, limiting their growth and effect on the plasma confinement. It is perhaps not currently possible to generate perturbations of sufficient strength that rotate faster than the natural frequency of the magnetic islands in STOR-M. However, it should be possible to lock the islands to a more slowly rotating perturbation. A demonstration of island rotational frequency adjustment to a variety of

different, slower perturbation frequencies would indicate it should also be possible to speed up island rotation on large tokamaks.

9.3.1 Construction of Additional H-Bridge Module(s)

The conceptual and development work to achieve magnetic perturbations that rotate with respect to the vacuum chamber has been completed, however an additional H-bridge module, an exact copy of the one currently in use, will need to be constructed. This will enable the production of not only oscillating perturbations, but also rotating ones. If more discrete coil arrays are to be added, additional H-bridge modules will be required. Each module can drive coils that are in-phase or 180° out of phase with respect to its output current, and the time-phase of coils corresponds to their angular locations.

9.3.2 Extension or Construction of Additional Saddle-Coils

While the initial results using static perturbations show a clear impact on island frequency, more experiments need to be performed with oscillating/rotating perturbations. Before these are done, it should be confirmed that the saddle coils can have an effect comparable to the helical coil when utilizing static currents. Both types of coils have similar mode numbers.

It may be that the helical coils' greater effect is due to it's complete coverage of the plasma column, contrasted with the relatively small coverage of the four arrays currently in place. Depending on how many H-bridge modules it is decided to use, the saddle-coil arrays can be enlarged or more can be built. Building more will result in purer modes, and will be simpler to implement as the design of the coils already in place cab be replicated. However, this will require more H-bridge modules (a total of 4 modules if the number of arrays is doubled to 8). If the number of arrays is kept the same, but they are extended in the toroidal direction a less pure m/n = 2/1 mode will be created, however only one additional H-bridge module will be needed.

9.3.3 Electromagnetic Noise Compensation

Firing the magnetic perturbation system creates a large amount of electromagnetic interference (EMI) that affects all the diagnostics available on STOR-M. It may be necessary to develop com-

pensation circuits or signal processing techniques to remove this noise if other diagnostics, such as the soft x-ray (SXR) cameras or ion-doppler spectroscopy (IDS), are to be used. The script currently used to reduce the impact of EMI on the magnetic signals works well for individual channels. If the full array of available Mirnov coils is to be utilized for singular-value decomposition (SVD) analysis a new system that works for all channels simultaneously will need to be developed.

9.3.4 Further Experiments Utilizing STOR-M's Diagnostics

Once a suitable method of compensating for EMI has been implemented, the impact of various types of magnetic perturbations on the plasma and magnetic islands can be investigated. It is hoped that islands will lock to the rotating perturbations and be brought to the same rotational frequency. This could have an impact on island width, and therefore also plasma confinement.

Toroidal flow velocity, as determined by IDS, can can also be examined. It has previously been seen on STOR-M that magnetic islands have some combination of electron temperature and density that is significantly different than in the bulk plasma [79]. So additionally, the SXR cameras present on the tokamak could be used to probe these parameters under the influence of the new system, along with the effect on sawtooth oscillations. Sawtooth oscillations, or relaxations, are commonly observed, periodic drops in temperature and density in the plasma core which impose a limit on the current density.

In future experiments, both co-rotating and counter-rotating magnetic perturbations (with respect to plasma flow) should be utilized. This should more clearly elucidate the causes behind any observed effects.

9.3.5 Increase Maximum System Parameters

If higher coil currents (and correspondingly a higher amplitude magnetic field) are required, the IGBTs in the H-bridge circuit could be replaced with higher rated modules newly available. Two potential upgrades from the latest iteration of IGBT technology are shown in Figure 9.1.

These are produced by ABB. However, similar models can be purchased from most major power electronics manufacturers.

To drive the higher currents the new IGBTs would allow would require an increase in charging

Table 9.1: Potential IGBT upgrades

5SNA-1500E33030	5SNA-3600E170300
$V_{ce} = 3300V$	$V_{ce} = 1700V$
$I_{c_{cont.}} = 1500A$	$I_{c_{cont.}} = 3600A$
$I_{c_{pulsed}} = 3000A$	$I_{c_{pulsed}} = 7200A$

voltage. The voltage the capacitor bank is charged to depends not only on the desired current, but also the frequency at which it is being driven. This is because of the change in the coils' effective resistance due to the skin effect. In all the times the system has been tested thus far, the charging voltage has been limited to approximately 400V. The charger is capable of supplying up to 1000V but must be limited to below 900V, the voltage rating of the capacitor bank. Moreover, most of the wiring of the magnetic perturbation system is rated for 600V. If the IGBTs are replaced and the charging voltage is to exceed this value much of the wiring will need to be replaced, or additional insulation added.

BIBLIOGRAPHY

[1] W. Hare S.C.B. Raper K. Frieler R. Knutti D.J. Frame R. Allen M. Meinshausen, N. Meinshausen. Greenhouse-gas emission targets for limiting global warming to 2 degrees celsius. *Nature*, 458, 2009.

[2] P. Etkins C. McGlade. The geographical distribution of fossil fuels unused when limiting global warming to 2 degrees celsius. *Nature*, 517, 2015.

[3] J. Wesson. *Tokamaks*. Oxford University Press, 2011.

[4] J.D. Lawson. Some criteria for a power producing thermonuclear reactor, 1955.

[5] Japan Atomic Energy Agency. JT-60 Operational history and the progress of plasma performance. *http://www.jt60.naka.jaea.go.jp/english/jt60/project/html/history.html*, 2016.

[6] B. Carroll and D. Ostlie. An introduction to modern astrophysics, 2nd edition, 2007.

[7] M.W. Hirsch. Schematic of a tokamak. *https://en.wikipedia.org/wiki/Tokamak*, 2015.

[8] G.D. Conway O. Mitarai A. Sarkissian H.M. Skarsgard L. Zhang A. Hirose W. Zhang, C. Xiao. Improved confinement and edge plasma fluctuations in the STOR-M tokamak. *Physics of Fluids B: Plasma Physics*, 4(10), 1992.

[9] W. Zhang A. Hirose C. Xiao, K.K. Jain. Measurement of plasma rotation velocities with electrode biasing in the saskatchewan torus-modified (STOR-M) tokamak. *Physics of Plasmas*, 1(7), 1994.

[10] L. Zhang D. McColl W. Zhang G. Conway A. Hirose H.M. Skarsgard O. Mitarai, C. Xiao. Alternating current plasma operation in the STOR-M tokamak. *Nuclear Fusion*, 36(10), 1996.

[11] A.K. Singh A. Hirose D. Liu, C. Xiao. Bench test and preliminary results of vertical compact torus injection experiments on the STOR-M tokamak. *Nuclear Fusion*, 46(1), 2006.

[12] S. Sen C. Xiao, A. Hirose. Improved confinement induced by tangential injection of compact torus into the saskatchewan torus-modified (STOR-M) tokamak. *Physics of Plasmas*, 11(8), 2004.

[13] T. Asai A. Hirose C. Xiao S. Elgriw, D. Liu. Control of magnetic islands in the STOR-M tokamak using resonant helical fields. *Nuclear Fusion*, 51(11), 2011.

[14] D. Trembach A. Hirose S. Elgriw A. Pant D. Rohraff T. Niu M. Dreval, C. Xiao. Simultaneous evolution of plasma rotation, radial electric field, MHD activity and plasma confinement in the STOR-M tokamak. *Plasma Physics and Controlled Fusion*, 50(9), 2008.

[15] C. Xiao A. Hirose M. Dreval, D. Rohraff. Retarding field energy analyzer for the Saskatchewan Torus-Modified plasma boundary. *Review of Scientific Instruments*, 80(10), 2009.

[16] C. Xiao D. Trembach and A. Hirose M. Dreval. Diamagnetic measurements in the STOR-M tokamak by a flux loop system exterior to the vacuum vessel. *Review of Scientific Instruments*, 80(5), 2009.

[17] M. Dreval, M. Hubeny, Y. Ding, T. Onchi, Y. Liu, K. Hthu, S. Elgriw, C. Xiao, and A. Hirose. Plasma confinement modification and convective transport suppression in the scrape-off layer using additional gas puffing in the STOR-M tokamak. *Plasma Physics and Controlled Fusion*, 55, 2013.

[18] A. Pant, A. Hirose, and C. Xiao. Repetitive operation of the university of saskatchewan compact torus injector. *Radiation Effects and Defects in Solids*, 165(2), 2010.

[19] F.F. Chen. Introduction to plasma physics and controlled fusion, 2nd edition, 1974.

[20] W.A. Cooper F. Yasseen A. Turnbull F. Troyon, A. Roy. Beta limit in tokamaks. experimental and computational status. *Plasma Physics and Controlled Fusion*, 30(11), 1988.

[21] F. Troyon, R. Gruber, H. Saurenmann, S. Semenzato, and S. Succi. MHD-limits to plasma confinement. *Plasma Physics and Controlled Fusion*, 26(1A), 1984.

[22] S.A. Sabbagh, A.C. Sontag, J.M. Bialek, D.A. Gates, A.H. Glasser, J.E. Menard, W. Zhu, M.G. Bell, R.E. Bell, A. Bondeson, C.E. Bush, J.D. Callen, M.S. Chu, C.C. Hegna, S.M. Kaye, L.L. Lao, B.P. LeBlanc, Y.Q. Liu, R. Maingi, D. Mueller, K.C. Shaing, D. Stutman, K. Tritz, and C. Zhang. Resistive wall stabilized operation in rotating high beta nstx plasmas. *Nuclear Fusion*, 46(5):635, 2006.

[23] T.C. Hender, R. Fitzpatrick, A.W. Morris, P.G. Carolan, R.D. Durst, T. Edlington, J. Ferreira, S.J. Fielding, P.S. Haynes, J. Hugill, I.J. Jenkins, R.J. La Haye, B.J. Parham, D.C. Robinson, T.N. Todd, M. Valovic, and G. Vayakis. Effect of resonant magnetic perturbations on COMPASS-C tokamak discharges. *Nuclear Fusion*, 32(12), 1992.

[24] R.J. Buttery, T.C. Hender, J.D. Ashall, K.B. Axon, G. Blow, and S.J. Fielding. Effects of resonant magnetic perturbations on divertor target power loads in COMPASS-D. *Nuclear Fusion*, 36(10), 1996.

[25] M. Lehnen, K. Aleynikova, P.B. Aleynikov, D.J. Campbell, P. Drewelow, N.W. Eidietis, Yu. Gasparyan, R.S. Granetz, Y. Gribov, N. Hartmann, E.M. Hollmann, V.A. Izzo, S. Jachmich, S.-H. Kim, M. Kocan, H.R. Koslowski, D. Kovalenko, U. Kruezi, A. Loarte, S. Maruyama, G.F. Matthews, P.B. Parks, G. Pautasso, R.A. Pitts, C. Reux, V. Riccardo, R. Roccella, J.A. Snipes, A.J. Thornton, and P.C. de Vries. Disruptions in ITER and strategies for their control and mitigation. *Journal of Nuclear Materials*, 463(Supplement C), 2015.

[26] A. Sanderson and S. Kruger. *http://www.vacet.org/gallery/images_video/NIMROD_87009_23_Surface1.png*.

[27] A. Sanderson, G. Chen, X. Trioche, D. Pugmire, S. Kruger, and J. Breslau. Analysis of recurrent patterns in toroidal magnetic fields. *IEEE Transactions on Visualization and Computer Graphics*, 16(6), 2010.

[28] F. Wagner, G. Becker, K. Behringer, D. Campbell, A. Eberhagen, W. Engelhardt, G. Fussmann, O. Gehre, J. Gernhardt, G. V. Gierke, G. Haas, M. Huang, F. Karger, M. Keilhacker,

O. Klüber, M. Kornherr, K. Lackner, G. Lisitano, G. G. Lister, H. M. Mayer, D. Meisel, E. R. Müller, H. Murmann, H. Niedermeyer, W. Poschenrieder, H. Rapp, H. Röhr, F. Schneider, G. Siller, E. Speth, A. Stäbler, K. H. Steuer, G. Venus, O. Vollmer, and Z. Yü. Regime of improved confinement and high beta in neutral-beam-heated divertor discharges of the asdex tokamak. *Physical Review Letters*, 49, 1982.

[29] H. Zohm. Edge localized modes (ELMs). *Plasma Physics and Controlled Fusion*, 38(2), 1996.

[30] M. Becoulet, F. Orain, G.T.A. Huijsmans, S. Pamela, P. Cahyna, M. Hoelzl, X. Garbet, E. Franck, E. Sonnendrücker, G. Dif-Pradalier, C. Passeron, G. Latu, J. Morales, E. Nardon, A. Fil, B. Nkonga, A. Ratnani, and V. Grandgirard. Mechanism of edge localized mode mitigation by resonant magnetic perturbations. *Physical Review Letters*, 113, 2014.

[31] S. Corti J. Gernhardt O. Kluber G. Lisitano K. McCormick D. Meisel S. Sesnic F. Karger, H. Wobig. Proceedings of 5th IAEA Int. Conf. Tokyo. Plasma Physics and Controlled Nuclear Fusion.

[32] Pulsator Team. The pulsator tokamak. *Nuclear Fusion*, 25(9), 1985.

[33] K. Bol, J.L. Cecchi, and C.C. Daughney et al. Proceedings of 5th IAEA Int. Conf. Tokyo. Plasma Physics and Controlled Nuclear Fusion.

[34] F. Karger, W. Feneberg, and J. Gernhardt et al. Controlled fusion and plasma physics. Proceedings of 8th eur. conf. prague. volume 13B Part II. European Physical Society.

[35] N.V. Ivanov and A.M. Kakurin. *Soviet Journal of Plasma Physics*, 5, 1979.

[36] K.M. McGuire and D.C. Robinson. Controlled fusion and plasma physics. Proceedings of 9th Eur. Conf. Oxford. volume 13B Part II. European Physical Society.

[37] M.V. Fernandes et al. I.L. Caldas, O.W. Bender. Resonant helical fields in TBR-1. *University of Sao Paulo*, page 654, 1987.

[38] C. Balkwill et al. A. W. Morris, S. Arshad. Controlled fusion and plasma physics. Proceedings of 16th Eur. Conf. Venice. volume 13B Part 2. European Physical Society.

[39] A.W. Morris, S. Arshad, and C. Balkwill et al. 1989 controlled fusion and plasma physics proc. 16th Eur. Conf. Venice. volume 13B Part II. European Physical Society.

[40] J.D. Fletcher et al. G. Nothnagel, D. Sherwell. 1989 controlled fusion and plasma physics proc. 16th Eur. Conf. Venice. volume 13B Part II. European Physical Society.

[41] Y. Huo et al. J. Chen, J. Xie. *Nuclear Fusion*, 30, 1990.

[42] D.E. Roberts, D. Sherwell, J.D. Fletcher, G. Nothnagel, and J.A.M. de Villiers. Major disruptions induced by helical coils on the tokoloshe tokamak. *Nuclear Fusion*, 31(2), 1991.

[43] R. P. da Silva et al. H. Franco, C. Ribeiro. *Review of Scientific Instruments*, 63:3710, 1992.

[44] W. Jin, Y.H. Ding, B. Rao, Q.M. Hu, X.S. Jin, N.C. Wang, X.Q. Zhang, Z.J. Wang, Z.Y. Chen, G. Zhuang, and the J-TEXT Team. Dependence of plasma responses to an externally applied perturbation field on MHD oscillation frequency on the J-TEXT tokamak. *Plasma Physics and Controlled Fusion*, 55(3), 2013.

[45] L. Frassinetti, K.E.J. Olofsson, P.R. Brunsell, and J.R. Drake. Resonant magnetic perturbation effect on tearing mode dynamics. *Nuclear Fusion*, 50(3), 2010.

[46] R.J. La Haye, R. Fitzpatrick, T.C. Hender, A.W. Morris, J.T. Scoville, and T.N. Todd. Critical error fields for locked mode instability in tokamaks. *Physics of Fluids B: Plasma Physics*, 4(7), 1992.

[47] Q. Hu, Q. Yu, B. Rao, Y. Ding, X. Hu, G. Zhuang, and the J-TEXT Team. Effect of externally applied resonant magnetic perturbations on resistive tearing modes. *Nuclear Fusion*, 52(8), 2012.

[48] D. Reiser and D. Chandra. Plasma currents induced by resonant magnetic field perturbations in tokamaks. *Physics of Plasmas*, 16(4), 2009.

[49] R. Fitzpatrick and T.C. Hender. The interaction of resonant magnetic perturbations with rotating plasmas. *Physics of Fluids B: Plasma Physics*, 3(3), 1991.

[50] R. Fitzpatrick. Interaction of tearing modes with external structures in cylindrical geometry (plasma). *Nuclear Fusion*, 33(7), 1993.

[51] N. Wang P. Shi Bi. Yi Y. Ding B Rao Z. Chen L. Gao Q. Hu, Q. Yu, X. Hu, J.Li K. Yu G. Z. H. Jin, M. Li, and the J-TEXT Team. Influence of rotating resonant magnetic perturbations on particle confinement. *Nuclear Fusion*, 54(12), 2014.

[52] H.R. Koslowski, Y. Liang, A. Kramer-Flecken, K. Lowenbruck, M. von Hellermann, E. Westerhof, R. C. Wolf, O. Zimmermann, and the TEXTOR team. Dependence of the threshold for perturbation field generated m / n = 2/1 tearing modes on the plasma fluid rotation. *Nuclear Fusion*, 46(8), 2006.

[53] G. Zhuang, K.W. Gentle, P. Diamond, J. Chen, B. Rao, L. Wang, K. Zhao, S. Han, Y. Shi, Y.H. Ding, Z.Y. Chen, X.W. Hu, Z.J. Wang, Z.J. Yang, Z.P. Chen, Z.F. Cheng, L. Gao, X.Q. Zhang, M. Zhang, K.X. Yu, Y. Pan, H. Huang, and the J-TEXT Team. Overview of the recent research on the J-TEXT tokamak. *Nuclear Fusion*, 55(10), 2015.

[54] R. Fitzpatrick, E. Rossi, and E.P. Yu. Improved evolution equations for magnetic island chains in toroidal pinch plasmas subject to externally applied resonant magnetic perturbations. *Physics of Plasmas*, 8(10), 2001.

[55] T.E. Evans, R.A. Moyer, P.R. Thomas, J.G. Watkins, T.H. Osborne, J.A. Boedo, E.J. Doyle, M.E. Fenstermacher, K.H. Finken, R.J. Groebner, M. Groth, J.H. Harris, R.J. La Haye, C.J. Lasnier, S. Masuzaki, N. Ohyabu, D.G. Pretty, T.L. Rhodes, H. Reimerdes, D.L. Rudakov, M.J. Schaffer, G. Wang, and L. Zeng. Suppression of large edge-localized modes in high-confinement DIII-D plasmas with a stochastic magnetic boundary. *Physical Review Letters*, 92, 2004.

[56] P.R. Thomas J.G. Watkins T.H. Osborne J.A. Boedo E.J. Doyle M.E. Fenstermacher K.H. Finken R.J. Groebner M. Groth J.H. Harris R.J. La Haye C.J. Lasnier S. Masuzaki N. Ohyabu D.G. Pretty T.L. Rhodes H. Reimerdes D.L. Rudakov M.J. Schaffer G. Wang L. Zeng T.E. Evans, R.A. Moyer. Suppression of large edge-localized modes in high-confinement DIII-D plasmas with a stochastic magnetic boundary. *Physical Review Letters*, 92, 2004.

[57] Y. Liang, H. R. Koslowski, P. R. Thomas, E. Nardon, B. Alper, P. Andrew, Y. Andrew, G. Arnoux, Y. Baranov, M. Bécoulet, M. Beurskens, T. Biewer, M. Bigi, K. Crombe,

E. De La Luna, P. de Vries, W. Fundamenski, S. Gerasimov, C. Giroud, M. P. Gryaznevich, N. Hawkes, S. Hotchin, D. Howell, S. Jachmich, V. Kiptily, L. Moreira, V. Parail, S. D. Pinches, E. Rachlew, and O. Zimmermann. Active control of type-i edge-localized modes with $n = 1$ perturbation fields in the JET tokamak. *Physical Review Letters*, 98, 2007.

[58] A. Kirk, E. Nardon, R. Akers, M. Becoulet, G. De Temmerman, B. Dudson, B. Hnat, Y.Q. Liu, R. Martin, P. Tamain, D. Taylor, and the MAST team. Resonant magnetic perturbation experiments on MAST using external and internal coils for ELM control. *Nuclear Fusion*, 50(3), 2010.

[59] J.M. Canik, R. Maingi, T.E. Evans, R.E. Bell, S.P. Gerhardt, H.W. Kugel, B.P. LeBlanc, J. Manickam, J.E. Menard, T.H. Osborne, J.-K. Park, S. Paul, P.B. Snyder, S.A. Sabbagh, E.A. Unterberg, and the NSTX team. ELM destabilization by externally applied non-axisymmetric magnetic perturbations in nstx. *Nuclear Fusion*, 50(3), 2010.

[60] W. Suttrop, T. Eich, J.C. Fuchs, S. Gunter, A. Janzer, A. Herrmann, A. Kallenbach, P.T. Lang, T. Lunt, M. Maraschek, R.M. McDermott, A. Mlynek, T. Putterich, M. Rott, T. Vierle, E. Wolfrum, Q. Yu, I. Zammuto, and H. Zohm. First observation of edge localized modes mitigation with resonant and nonresonant magnetic perturbations in asdex upgrade. *Physical Review Letters*, 106, 2011.

[61] I.T. Chapman, A. Kirk, R.J. Akers, C.J. Ham, J.R. Harrison, J. Hawke, Y.Q. Liu, K.G. McClements, S. Pamela, S. Saarelma, R. Scannell, A.J. Thornton, and The MAST Team. Assessing the merits of resonant magnetic perturbations with different toroidal mode numbers for controlling edge localised modes. *Nuclear Fusion*, 54(12), 2014.

[62] Y. Sun, Y. Liang, Y. Q. Liu, S. Gu, X. Yang, W. Guo, T. Shi, M. Jia, L. Wang, B. Lyu, C. Zhou, A. Liu, Q. Zang, H. Liu, N. Chu, H. H. Wang, T. Zhang, J. Qian, L. Xu, K. He, D. Chen, B. Shen, X. Gong, X. Ji, S. Wang, M. Qi, Y. Song, Q. Yuan, Z. Sheng, G. Gao, P. Fu, and B. Wan. Nonlinear transition from mitigation to suppression of the edge localized mode with resonant magnetic perturbations in the east tokamak. *Physical Review Letters*, 117, 2016.

[63] T.E. Evans, K.H. Burrell, M.E. Fenstermacher, R.A. Moyer, T.H. Osborne, M.J. Schaffer, W.P. West, L.W. Yan, J.A. Boedo, E.J. Doyle, G.L. Jackson, I. Joseph, C.J. Lasnier, A.W.

Leonard, T.L. Rhodes, P.R. Thomas, J.G. Watkins, and L. Zeng. The physics of edge resonant magnetic perturbations in hot tokamak plasmas. *Physics of Plasmas*, 13(5), 2006.

[64] Y.M. Jeon, J.K. Park, S.W. Yoon, W.H. Ko, S.G. Lee, K.D. Lee, G.S. Yun, Y.U. Nam, W.C. Kim, Jong-Gu Kwak, K.S. Lee, H.K. Kim, and H.L. Yang. Suppression of edge localized modes in high-confinement kstar plasmas by nonaxisymmetric magnetic perturbations. *Physical Review Letters*, 109, 2012.

[65] J. Lee, G.S. Yun, M.J. Choi, J.M. Kwon, Y.M. Jeon, W. Lee, N.C.Luhmann, and H.K. Park. Nonlinear interaction of edge-localized modes and turbulent eddies in toroidal plasma under $n = 1$ magnetic perturbation. *Physical Review Letters*, 117, 2016.

[66] D.M. Orlov, R.A. Moyer, T.E. Evans, C. Paz-Soldan, N.M. Ferraro, R. Nazikian, J.S. deGrassie, B.A. Grierson, D. Eldon, M.E. Fenstermacher, J.D. King, N.C. Logan, M.J. Lanctot, R. Maingi, P.B. Snyder, E.J. Strait, and A. Wingen. Suppression of type-I ELMs with reduced rmp coil set on DIII-D. *Nuclear Fusion*, 56(3), 2016.

[67] P. Cahyna and E. Nardon. Model for screening of resonant magnetic perturbations by plasma in a realistic tokamak geometry and its impact on divertor strike points. *Journal of Nuclear Materials*, 415(1), 2011. Proceedings of the 19th International Conference on Plasma-Surface Interactions in Controlled Fusion.

[68] A.J. Thornton, A. Kirk, P. Cahyna, I.T. Chapman, J.R. Harrison, Y. Liu, and the MAST Team. The effect of resonant magnetic perturbations on the divertor heat and particle fluxes in MAST. *Nuclear Fusion*, 54(6), 2014.

[69] Strike-point splitting induced by external magnetic perturbations: Observations on JET and MAST and associated modelling. *Journal of Nuclear Materials*, 415(1), 2011. Proceedings of the 19th International Conference on Plasma-Surface Interactions in Controlled Fusion.

[70] L. Zhou, Y. Liu, Y. Liu, and X. Yang. Plasma response based rmp coil geometry optimization for an ITER plasma. *Plasma Physics and Controlled Fusion*, 58(11), 2016.

[71] A. Loarte, G. Huijsmans, S. Futatani, L.R. Baylor, T.E. Evans, D. M. Orlov, O. Schmitz, M. Becoulet, P. Cahyna, Y. Gribov, A. Kavin, A. Sashala Naik, D.J. Campbell, T. Casper,

E. Daly, H. Frerichs, A. Kischner, R. Laengner, S. Lisgo, R.A. Pitts, G. Saibene, and A. Wingen. Progress on the application of ELM control schemes to ITER scenarios from the non-active phase to dt operation. *Nuclear Fusion*, 54(3), 2014.

[72] S. Elgriw. Effects of resonant magnetic perturbations on the STOR-M tokamak discharges. *University of Saskatchewan*, 2014.

[73] S. Elgriw, J. Adegun, M. Patterson, A. Rohollahi, D. Basu, M. Nakajima, K. Colville, D. Gomez, C. Greenwald, J. Zhang, A. Hirose, and C. Xiao. Design of rotating resonant magnetic perturbation coil system in the STOR-M tokamak. *Fusion Engineering and Design*, 123, 2017. Proceedings of the 29th Symposium on Fusion Technology (SOFT-29) Prague, Czech Republic, September 5-9, 2016.

[74] J. Dodge. IGBT technical overview. *https://www.microsemi.com/document−portal/doc_view /14709−igbt−technical−overview*, 2014.

[75] D.W. Knight. Practical continuous functions for the internal impedance of solid cylindrical conductors. 2012.

[76] T. Van Duzer S. Ramo, J.R. Whinnery. *Fields and Waves in Communication Electronics*. John Wiley and Sons Inc., 3rd edition.

[77] S. Elgriw, D. Liu, T. Asai, A. Hirose, and C. Xiao. Control of magnetic islands in the STOR-M tokamak using resonant helical fields. *Nuclear Fusion*, 51(11), 2011.

[78] Joseph Adegun Adedapo. Effect of lithium coating on the impurities and shielding effect of plasma on the resonant magnetic perturbations field in the STOR-M tokamak plasma. *University of Saskatchewan*, 2017.

[79] S. Elgriw. Investigation of magnetohydrodynamic fluctuation modes in the STOR-M tokamak. *University of Saskatchewan*, 2009.